

02892102

~~A3414/A3415~~

United Kingdom Atomic Energy Authority

HARWELL

**An investigation of the reaction
mechanism for resonance neutron
capture in ^{54}Fe and ^{62}Ni**

J P Mason

Nuclear Physics Division
Harwell Laboratory, Oxfordshire

January 1986

© - UNITED KINGDOM ATOMIC ENERGY AUTHORITY - 1986
Enquiries about copyright and reproduction should be addressed to the Publications
Office Harwell Laboratory Oxfordshire OX11 0RA England

**AN INVESTIGATION OF THE REACTION MECHANISM FOR
RESONANCE NEUTRON CAPTURE IN ^{54}Fe AND ^{62}Ni**

J.P. Mason

ABSTRACT

The gamma-ray spectra produced following neutron capture in the low energy resonances of ^{54}Fe and ^{62}Ni have been observed, using the Harwell 136 MeV electron linear accelerator facility, HELIOS, as a source of pulsed neutrons.

The aim of these measurements was to compare the observed gamma-ray transition strengths for *s*-wave capture with the predictions of Lynn's valence model, in order to obtain some insight into the reaction mechanism.

Using the optical model formulation of the valence model, careful calculations were made of the partial radiative widths to low-lying $p_{1/2}$ and $p_{3/2}$ states following *s*-wave resonance capture. For the 1.8 keV resonance in ^{54}Fe , good agreement was obtained between the absolute values for the partial radiative widths, as deduced from the experiment, and the theoretical predictions. However, the data for the 4.5 keV resonance of ^{62}Ni showed no evidence of valence capture.

The failure to observe single particle effects in ^{62}Ni capture was interpreted as being due to the interference between the valence and statistical contributions, whereas the apparent success for the nuclide ^{54}Fe was attributed to the fact that it has a closed neutron shell, providing such a strong valence component to the capture that the interference with compound nuclear terms is not significant.

It was concluded that, for *s*-wave capture in the mass region $A \approx 55$, single particle effects may only be apparent if the size of the valence component is about an order of magnitude larger than the compound nuclear component, and that this may limit the importance of such effects to a few nuclides.

In addition, although not part of the studies of the applicability of the valence model, some information was obtained on the radiative decay of *p*-wave resonances of ^{54}Fe and ^{62}Ni .

Nuclear Physics Division
Harwell Laboratory

January 1986

HL86/1039

ACKNOWLEDGEMENTS

This thesis could not have been written without the help and encouragement which I received from so many people. First and foremost, I would like to thank Dr. Bryan Patrick for his thoughtful and generous supervision, and for his tact when suppressing some of the less practical suggestions which I proposed! I am grateful to him for the many stimulating and exciting discussions which we had, and for the enthusiasm which he engendered in this work.

I would also like to thank Drs. Eric Lynn and Mike Coates for giving me the opportunity to do this work within the linac group, and to members of the group who provided advice so willingly. I particularly wish to mention Mick Moxon, whose enthusiasm for capture experiments knows few bounds, and who provided an enormous amount of advice and encouragement from his experience in this field of research. His guidance in the application of the code REFIT is also much appreciated. Thanks are also due to Nigel Hawkes for stimulating discussions and for timely suggestions concerning the data acquisition. Stimulating, though irrelevant, discussions with Dr. Martyn Sené were much appreciated.

Experimental measurements such as these rely on technical support, and I am grateful to Dave Webb and John Brisland for maintaining the data acquisition computer at all times of the day and night, to the workshop staff, to the operators of the linac, and to Dr. Jim Riddle for his skill in producing beam from a sometimes rather reluctant machine!

I would also like to thank Drs. Tony Lane, Eric Lynn and Peter Hodgson for so readily providing advice on the theoretical side of this work, and for assistance in the interpretation of the data.

I am most grateful to Dr. Archie Ferguson for initially providing me with the opportunity to carry out this work whilst at Harwell, and to Prof. George Morrison for his continued interest in the work.

Finally, I wish to thank my fiancée, Gill, for her invaluable support and encouragement, as well as for her practical help with figures contained in this thesis.

TABLE OF CONTENTS

CHAPTER 1	INTRODUCTION	1
1.1	Historical Background	1
1.1.1	Experimental Developments.....	1
1.1.2	Theoretical Advances.....	1
1.2	The Neutron Capture Reaction.....	3
1.2.1	Introduction.....	3
1.2.2	Non-statistical Effects in the Resonance Region	3
1.2.3	The Reaction Mechanism	4
1.3	Applications of the Neutron Capture Reaction	6
1.3.1	Nuclear Power	6
1.3.2	Stellar Nucleosynthesis.....	6
1.3.3	Prompt Gamma-ray Analysis	6
1.4	An Outline of the Present Investigations	7
1.4.1	Purpose	7
1.4.2	Theory.....	7
1.4.3	Experiment.....	7
CHAPTER 2	NEUTRON CAPTURE THEORY	8
2.1	Introduction	8
2.1.1	The Capture Cross-section.....	8
2.1.2	The Behaviour of Partial Radiative Widths	8
2.2	The Strong Coupling Model.....	9
2.3	The Giant Dipole Resonance Model	10
2.4	The Lane-Lynn Theory	11
2.4.1	The Resonant Capture Components	11
2.4.2	Channel Capture	12
2.4.3	Non-Resonant Capture	13
2.4.4	Thermal Capture	13
2.5	Valence Neutron Transitions	14
2.5.1	Average Partial Widths	14
2.5.2	The Specialised Valence Model	15
2.5.3	Alternative Forms for the Valence Model.....	16
2.6	Valence Model Calculations.....	17
2.6.1	Initial and Final State Wave Functions	17
2.6.2	The Reduced Valence Width.....	18
2.6.3	The Particular Cases ^{54}Fe and ^{62}Ni	19
CHAPTER 3	EXPERIMENTAL TECHNIQUES	23
3.1	Introduction	23
3.1.1	Neutron Spectroscopy	23
3.1.2	Data Collection	24
3.2	The Neutron Source and Flight Path	25
3.2.1	The 136 MeV Harwell Linac – HELIOS.....	25
3.2.2	The Neutron Energy Resolution.....	26
3.2.3	The Collimation of the Flight Path.....	26
3.2.4	Components of the Flight Path	28
3.3	Capture Gamma-ray Detection	29
3.3.1	Detectors and Geometry	29
3.3.2	The Kandiah Pulse Height Processing System	30

	3.3.3	The Timing System	31
3.4		The Electronics and Computer Interface	32
	3.4.1	Introduction	32
	3.4.2	Combining the Two Detectors	32
	3.4.3	The Data Acquisition	35
3.5		Neutron Fluence Measurements	36
CHAPTER 4		METHODS OF ANALYSIS	37
4.1		Introduction	37
	4.1.1	Analysis of Two Parameter Data	37
	4.1.2	Peak Extraction Techniques	37
	4.1.3	Experimental Complexities	38
4.2		Expressions for the Partial Radiative Width	40
4.3		Gamma-ray Transmission Calculations	41
4.4		The Detector Efficiency Determination	43
4.5		Area Analysis of Gamma-ray Transitions	44
	4.5.1	The Gamma-ray Spectrum	44
	4.5.2	The Underlying Background	44
	4.5.3	Extracting the Peak Area	45
	4.5.4	Relative Gamma-ray Transition Strengths	46
4.6		Shape Analysis	46
	4.6.1	The Time-of-flight Spectrum	46
	4.6.2	Corrections to the Observed Spectrum	47
	4.6.3	The Yield Curve	47
	4.6.4	Fitting of the Yield Curve with REFIT	48
	4.6.5	Analysis of Transmission Data	48
CHAPTER 5		PRELIMINARY MEASUREMENTS	50
5.1		Detector Efficiency Measurements	50
	5.1.1	Thermal Neutron Capture Measurements	50
	5.1.2	Standard Source Values	51
	5.1.3	Combining Low and High Energy Determinations	52
5.2		The Timing Resolution	52
5.3		The Neutron Background Determination	53
5.4		^{10}B Sample Thickness Measurements	53
CHAPTER 6		RESULTS	56
6.1		^{54}Fe Measurements	56
	6.1.1	Experimental Details	56
	6.1.2	The s-wave Resonances	56
	6.1.3	The p-wave Resonances	57
6.2		^{62}Ni Measurements	59
	6.2.1	Experimental Details	59
	6.2.2	The s-wave Resonances	60
	6.2.3	The p-wave Resonances	60
6.3		Natural Nickel Measurements	62
	6.3.1	Experimental Details	62
	6.3.2	The 4.5 keV ^{62}Ni s-wave Resonance	62
CHAPTER 7		DISCUSSION AND CONCLUSIONS	64
7.1		Capture in ^{54}Fe	64
7.2		Capture in ^{62}Ni	64
7.3		Future Measurements	66

APPENDIX A SOLVING THE SCHRÖDINGER EQUATION	68
A.1 Introduction	68
A.2 The Radial Equation	68
A.3 Numerical Method.....	68
A.4 Boundary Conditions	69
A.5 Finding the Bound State Energy	70
A.6 Normalisation of the Wave Functions.....	70
APPENDIX B EXPRESSIONS FOR OBSERVABLES	72
B.1 The s-wave Scattering Matrix Element.....	72
B.2 The s-wave Neutron Strength Function	72
B.3 The Scattering Radius.....	72
APPENDIX C ERROR ANALYSIS USING COVARIANCES	
C.1 Introduction	73
C.2 Definitions	73
C.3 The Propagation of Errors	74
C.4 Example: Relative Transition Strengths.....	74
C.5 Linear Least Squares Fitting	75
C.6 The Fitting of Polynomials	76
C.7 Applications of Polynomial Fitting	77
REFERENCES	79

1 INTRODUCTION

1.1 Historical Background

1.1.1 Experimental Developments

The investigation of neutron reactions began soon after the discovery of the neutron by Chadwick in 1932. Fermi and his co-workers discovered a variety of new isotopes by neutron activation experiments (Fer + 34) whilst the first gamma-rays from neutron capture were seen by Lea (Lea 34) when he detected gamma-rays from paraffin bombarded by neutrons from a polonium-beryllium source. A most significant discovery in relation to neutron reactions was made when early measurements in the field of neutron spectroscopy revealed rapid variations in neutron cross-sections with incident energy i.e the neutron resonance phenomenon (MT 36, Ras + 36).

Post-war advances in neutron capture were helped enormously by the increased flux available from nuclear reactors. At the same time, the study of the gamma-ray spectrum following neutron capture became possible with the development of magnetic spectrometers. Significant discoveries were made by Kinsey and Bartholomew who, using a pair spectrometer, found correlations between gamma-ray intensities and (d,p) spectroscopic factors for the same final states (KB 54). Groschev, who used a Compton spectrometer, found an anomalous bump in the gamma-ray spectra of certain medium mass nuclides (Gro 55) and further evidence of correlations of gamma-ray intensities with (d,p) spectroscopic factors (Gro + 58). By 1959, with extensive measurements available, a compilation of thermal neutron capture gamma-rays was produced (Gro + 59).

Only limited information on the capture mechanism could be obtained from these thermal measurements because the initial (compound nuclear) state formed was not in general one of definite spin and parity, rather it was the superposition of states from the tails of resonances both bound and unbound. The ideal study, the decay from a resonance of known spin and parity was not feasible with the magnetic spectrometers of the 1950s due to their low gamma-ray detection efficiency. Although high efficiency NaI detectors had been developed, their gamma-ray resolution was poor and it was the introduction of Ge(Li) detectors in the 1960s which gave a new impetus to measurements of capture spectra. This was a detector having both high resolution and high efficiency. Together with improved beam choppers on reactors and the development of pulsed Van de Graaff machines and electron linear accelerators, the time-of-flight technique was used to observe transitions from resonances to particular final states of the compound nucleus.

Much of the work on resonance capture gamma-rays was performed on heavy elements, especially the actinides, stimulated by the need to understand the capture mechanism in these elements in order to improve reactor calculations. However, a considerable amount of data has become available concerning non-statistical effects in various mass regions and this will be discussed in section 1.2.

1.1.2 Theoretical Advances

The first model to be proposed for slow neutron reactions was the single particle model (Bet 35, Ama + 35). This was, however, quite unable to explain the existence of the neutron resonances. Variations in the cross-section were expected

within the model but over much larger energy ranges, of the order of an MeV rather than the observed fluctuations over an eV or so.

The problem was resolved when Bohr proposed the compound nucleus model in 1936 (Boh 36). He pictured the incoming neutron interacting strongly with the nucleus and thus rapidly sharing its energy amongst the other nucleons. This leads to long-lived and therefore narrow states, since subsequent decay of the compound nucleus depends on the probability that a large fraction of the excitation energy is once more concentrated on a single nucleon. Since the compound nuclear state so formed is a complicated one, it permitted a statistical interpretation of the neutron reactions.

The shape of the cross-section of a resonance was first derived by Wigner and Breit (WB 36). They supposed that a bombarding nucleon could excite a long-lived two-particle state. The Breit–Wigner formula was based on rather weak assumptions, but more formal derivations were obtained which showed the formula was correct for the case of a narrow, well-isolated resonance (KP 39, WE 47, HR 61).

The statistical model was applied to neutron capture by Blatt and Weisskopf (BW 52) who derived estimates of the average transition strengths for resonance capture. Porter and Thomas (PT 56) deduced that the statistical model implied a wide distribution of these strengths, given by a χ^2 distribution with one degree of freedom.

Evidence that the statistical model could not explain all the experimental observations was also considered. The correlations between gamma-ray intensities and the (d,p) spectroscopic factors of the same final states could be explained if a direct mechanism was invoked. Lane and Wilkinson (LW 55) pointed out that the (n, γ) and (d,p) reaction matrix elements would have a common overlap factor if the capture proceeded through that part of the initial state for which the target was in its ground state. The observed correlations would then follow. Bockelmann (Boc 59) calculated the direct cross-section at thermal energies but found values in general too low as he ignored contributions from the nuclear wave function outside the interaction radius, the importance of which had first been noted by Thomas (Tho 51).

Radiative capture was dealt with formally by Lane and Thomas (LT 58) and subsequently in detail by Lane and Lynn (LL 60) who recognised three distinct components to the resonance neutron capture reaction: compound nucleus, channel and potential capture. Working within the framework of the intermediate coupling model (LW 55a), which had been introduced to describe the situation between the single particle and the compound nucleus model, Lynn isolated the valence component of the channel capture (Lyn 68). Subsequent formulations of the valence model were made within the optical model (LM 74) and the shell model (BM 73, CM 75, Cug 76). Attempts were also made to explain the success of the valence model since single particle effects had been expected to play only a small part in the resonance capture process (Lan 74, Gya + 74).

Other simple states through which capture could occur beside the valence state have been considered by a variety of authors (Bec 69, Bec 71, Sol 74) and a detailed treatment of the relationship between these doorway states and correlations was provided by Lane (Lan 71). However, it is the valence model which has provided the best quantitative predictions of resonance capture widths and its validity still remains to be tested fully.

1.2 The Neutron Capture Reaction

1.2.1 Introduction

The neutron capture reaction has been studied over nine orders of magnitude of neutron energy. Figure 1.1 illustrates the range, the techniques used for the measurements and the principal mechanisms believed to be dominant in specific regions. Attention will be concentrated on the resonance energy region, where s -wave and p -wave interactions predominate in what is normally assumed to be a statistical fashion.

When the nucleus absorbs a neutron it excites levels of the compound nucleus in the region of 5–10 MeV, equal to the neutron separation energy plus the kinetic energy of the incoming neutron. Figure 1.2 illustrates the energetics of the process. The excited state may decay by re-emitting a neutron, i.e. elastic scattering, or by gamma-ray emission, which may be directly to the ground state or, more usually, in a cascade via intermediate states. The first gamma-ray of such a cascade is known as the primary transition, subsequent members of the cascade being secondary, tertiary *etc.* Depending on the particular nuclide and the energy of the neutron, other modes of decay such as fission and inelastic scattering are also possible.

In Bohr's statistical model, the compound nucleus retains no memory of how it was formed, and so the mode of decay is a stochastic process. The probability for decay from the initial state via each open channel is proportional to a corresponding width: Γ_n for neutron emission and Γ_γ for radiative decay. The radiative width may further be split into its partial widths for decay via particular primary transitions. The radiative width for a resonance λ , $\Gamma_{\gamma\lambda}$ is then equal to the sum of the partial widths, $\Gamma_{\gamma\lambda\mu}$, for decays to different final states μ ,

$$\Gamma_{\gamma\lambda} = \sum_{\mu} \Gamma_{\gamma\lambda\mu}. \quad (1.1)$$

The compound nuclear state is a very complicated one in the sense that its wave function no longer appears to be anything like a single neutron plus target nucleus. This means that overlaps with final states via single particle radiative transitions are randomly distributed, and a Porter–Thomas distribution is predicted for the partial radiative widths. This distribution has a large variance, but the total radiative width, being the sum of (say) n partial radiative widths, is distributed as a χ^2 distribution with n degrees of freedom. Figure 1.3 illustrates how the χ^2 function tends to peak as the number of degrees of freedom, n , increases. The number of partial widths which contribute to the total width is relatively large in the statistical model, so the distribution of total radiative widths for different resonances is expected to be narrow.

The statistical model also implies that, because single particle effects should be absent, correlations should not exist between the strengths of radiative transitions and the single particle natures of the initial and final states, as given by the neutron width and the (d,p) spectroscopic factors respectively.

1.2.2 Non-statistical Effects in the Resonance Region

1.2.2.1 The neutron strength function

The l -wave neutron strength function S_l is defined as

$$S_l = \frac{\langle \gamma_{nl}^2 \rangle}{D_l} \quad (1.2)$$

where $\langle \gamma_{nl}^2 \rangle$ is the average reduced neutron width for resonances λ formed by neutrons of incident orbital angular momentum l , and \bar{D}_l is the average spacing of such resonances. The strength function is a measure of the probability of compound nucleus formation and as such is not expected to show structure when expressed as a function of mass number. However, as is illustrated in Figure 1.4, the s -wave neutron strength function shows substantial peaks at mass numbers $A = 55$ and $A \approx 150$, the latter region being split into two due to nuclear deformation. The size of nuclei in these mass regions is such that $3s$ and $4s$ neutrons respectively are just unbound and the existence of these size resonances indicates that the single particle state still plays a part in the compound nucleus wave function. Similar size resonances can be seen in the p -wave strength function, although measurements of this quantity are less extensive. The curves in Figure 1.4 are optical model fits to the data.

1.2.2.2 Spectroscopic factor correlations

Contrary to the predictions of the statistical model, many instances of correlations have been found. A compilation has been provided by Allen and Musgrove (AM 79) and Figure 1.5 shows a graph of the observed correlations for s -wave resonances as a function of mass number. The initial state correlations ρ_I are of the form $\rho_I(\gamma_{nl}^2, \Gamma_{\gamma\lambda})$ and the final state correlations ρ_F are $\rho_F(\theta_\mu^2, \Gamma_{\gamma\lambda\mu}/E_\gamma^3)$ where E_γ is the gamma-ray energy and θ_μ^2 is the (d,p) spectroscopic factor of the final state μ . It should however be noted that some of the initial state correlations may be spurious due to the sensitivity of capture detectors to scattered neutrons.

1.2.2.3 Humps in the gamma-ray spectrum

Enhanced transition strength for capture gamma-rays with energies from 5–6 MeV has been observed (Bar + 73). This is contrary to expectations of a smooth spectrum when averaged over resonances, proportional to E_γ^3 times the density of the final states.

1.2.2.4 The behaviour of total radiative widths

If the Porter–Thomas distribution holds for the reduced partial radiative widths then the total radiative widths are expected to be fairly constant. However, when Cameron (Cam 59) fitted the total widths of all available nuclides, taking level density effects into account, he discovered a residual variation with A which could not be explained in the framework of the statistical model. A peak was observed in the region $A = 145$ to $A = 175$, the $4s$ size resonance. In addition, fluctuations in the total radiative cross-section for different resonances were frequently found to be quite large, indicating the number of degrees of freedom was less than expected and particular transitions were being enhanced above statistical expectations.

The mass regions in which non-statistical effects have been observed are therefore

- (i) $40 < A < 70$, the $3s$ region,
- (ii) $90 < A < 110$, the $3p$ region and
- (iii) $135 < A < 205$, the $4s$ region.

1.2.3 The Reaction Mechanism

The existence of non-statistical effects has prompted the proposal of a number of mechanisms for capture other than that of the extreme compound nucleus model. The mechanisms are illustrated schematically in Figure 1.6 and are discussed briefly below.

1.2.3.1 Direct or potential capture

In the Lane–Lynn theory of radiative capture a non-resonant, direct component to the capture cross-section appears. It is known as hard-sphere capture and corresponds to a neutron undergoing a single particle transition to a low-lying state of large single particle character. Correlations with the (d,p) spectroscopic factors of the final state are thus expected. In the strong coupling assumption this is the only component expected for potential capture, but in the case of the intermediate coupling model another component is present, due to the tails of distant resonances, which is added to the hard-sphere amplitude to give the total non-resonant potential capture amplitude. Evidence for direct capture has been obtained by observing spectra at thermal energies in isotopes where there are no nearby resonances which dominate the cross-section e.g. in ^{136}Xe (Mug 79), ^{130}Te (Hon + 80), ^{34}S (Car + 82) and ^{12}C (Mug + 82).

1.2.3.2 Valence capture

In the valence model, decay following resonant capture is assumed to be dominated by single particle transitions of neutrons from the capturing state to low-lying levels, whilst the target nucleus acts as an inert core. Within the model, absolute values of the partial radiation widths are predicted to be proportional to the spectroscopic factors of both initial and final states, accounting for observed correlations. Confirmation of the model has been impressively demonstrated in the $3p$ size resonance (Mug + 71). In the $3s$ region also, transition amplitudes have been found to agree with the valence model predictions e.g. in ^{54}Fe (Ram + 80) and ^{32}S (AC + 85), although only relative amplitudes were measured. On the other hand, there are several cases where the model appears to fail: ^{56}Fe and ^{58}Fe (Wel + 78, Kom + 84), ^{59}Co (Kop + 84) and ^{100}Mo (Wei + 79). Clearly, further investigations in these regions, and particularly absolute measurements, are of interest.

1.2.3.3 Doorway state capture

In the valence capture discussed above, it is the one-particle zero-hole (1p-0h) state of neutron plus inert target core which dominates the capture. However, the resonant state has many other configurations contributing to it. Levels of complexity are built up as extra particle-hole pairs are excited from the core. The first stage of excitation leads to the formation of a 2p-1h state, referred to as a doorway, since it marks the start and end of the formation of the compound nucleus. Decay from the more complex configurations (3p-2h, 4p-3h *etc.*) gives rise to statistical spectra, but if 2p-1h states play a large part in the capture process, they are simple enough to give non-statistical decay and provide final state correlations. De-excitation by gamma-ray emission may take place from these states either by particle-hole annihilation or by a particle transition in the presence of an excited core. Any residual non-statistical nature unexplained by the valence model could be attributed to these doorway states providing a strong capture channel.

1.3 Applications of the Neutron Capture Reaction

The neutron capture reaction has found applications in a variety of fields outside pure nuclear physics research. Some of these applications relate to other areas of physics, for example stellar nucleosynthesis, and others have a direct practical importance: nuclear power, activation analysis, the doping of semi-conductors, isotope production and prompt gamma-ray analysis. Three of the topics having the most current interest are presented below, and further details and references may be found in a recent review by Chrien (Chr 84).

1.3.1 Nuclear Power

Nuclear data needs for fission reactor design have been the stimulus for much of the research carried out in neutron physics and further understanding of the processes involved continues to be of value to the nuclear power programme. An improved knowledge of the capture cross-sections is of importance in relation to the neutronics characteristics of reactors and other effects such as the temperature coefficient of reactivity and the activation of coolant circuits. The spectrum following capture in the materials present in a reactor is of direct significance in calculations of the gamma-ray heating.

Many measurements are very difficult or impossible to make and reactor calculations frequently rely on theory for unknown neutron cross-sections. For instance, the existence of non-statistical effects may have to be taken into account as improved accuracies are required. This is particularly true for the structural materials of fast reactors (Fe, Cr, Ni, Mo *etc.*) which are in mass regions known to show non-statistical effects.

1.3.2 Stellar Nucleosynthesis

It is generally accepted that all but the very lightest elements were formed in the stars. The production of elements heavier than iron depends on the neutron capture reaction since the coulomb repulsion is too large at stellar temperatures to permit charged particle reactions when $Z > 26$. Stars contain neutrons with a Maxwellian distribution of energies at a temperature of ≈ 30 keV and this results in a close connection between the energy-averaged neutron capture cross-section and the abundance of elements.

The two principal mechanisms involved in nucleosynthesis are the rapid and slow processes, known as the r-process and the s-process respectively. The s-process proceeds slowly (compared with the competing β decay) up the valley of stability whilst the r-process produces neutron-rich isotopes near the neutron drip-line which decay to stability via β decay. Accounting for the contribution from each process provides valuable information for both astrophysicists and cosmologists. For instance, the age of the universe can be estimated which in turn provides a limit on the mass of the neutrino (Kla 85).

1.3.3 Prompt Gamma-ray Analysis

The spectrum of gamma-rays given off by an isotope when irradiated by neutrons is a unique signature of that substance. Therefore, in many situations an elemental analysis can be carried out by observing the gamma-ray spectrum with a high resolution spectrometer (usually a Ge detector) whilst the sample under analysis is irradiated in a neutron flux. Reactor based systems allow the most sensitive analysis as the neutron flux is large and very small quantities of some materials can be

detected. Applications of the technique are found in the fields of archaeology, air filter analysis, oil and mineral exploration and medical diagnosis amongst others.

Mobile analysis may be carried out by using a suitable source of neutrons such as a ^{238}Pu -Be or a ^{252}Cf source. Such mobile units are in use for medical diagnosis, trace elements being detected in particular organs of the body.

There are also many commercial applications such as in oil borehole logging. Small D-T accelerators have been developed which provide 14 MeV neutrons. These can be placed down a borehole together with a gamma-ray detector. The spectrum which is observed contains gamma-rays from both inelastic scattering and from thermal neutron capture, with timing differences being used to separate the two contributions.

1.4 An Outline of the Present Investigations

1.4.1 Purpose

The purpose of the current work was to investigate the nature of the non-statistical effects present in isotopes in the $3s$ size resonance. In particular, as the valence model predicts large transition amplitudes to be present for high energy transitions in ^{54}Fe and ^{62}Ni , resonance capture was observed in these two nuclides and compared with theory. No reliable measurements of the absolute partial radiative widths previously existed for these nuclides, and they were expected to provide a good test of the validity of the valence model.

1.4.2 Theory

Careful theoretical calculations were carried out to predict the partial widths for radiative capture within the framework of the valence model. The formulation of Lane and Mughabghab was used (LM 74), in which an optical model solution is used for the initial state wave function. The effects of changes in optical model parameters were investigated which allowed an error to be ascribed to the predictions of the model. The details of the calculations will be given in Chapter 2.

1.4.3 Experiment

The experiment was designed to observe the gamma-ray spectrum following capture in a sample placed in a flight path on the fast neutron target of the Harwell linac HELIOS. Two high purity n-type Ge detectors were used to observe the spectrum. Absolute values of the gamma-ray transition strengths could be calculated by comparing yields with a run using a ^{10}B sample, and in such a way, the partial widths were deduced for the lowest energy s -wave resonances, and some p -wave resonances in ^{54}Fe and ^{62}Ni . The experimental method will be explained more fully in Chapter 3.

The methods used for the analysis of the experimental data are described in Chapter 4, and results of preliminary measurements, such as that of the detector efficiency using thermal capture gamma-rays, and the background determination using a filtered neutron beam, are presented in Chapter 5. The results of the capture data for ^{54}Fe and ^{62}Ni follow in Chapter 6, and finally, in Chapter 7 these results are discussed and some conclusions are drawn concerning these investigations.

2 NEUTRON CAPTURE THEORY

2.1 Introduction

This chapter deals with some theoretical aspects of the neutron capture reaction in the resonance energy region. Only electric dipole transitions are considered, as these dominate capture in the medium-mass nuclei of interest here. Various models are discussed, but particular attention is paid to the valence model, for which detailed calculations have been made.

2.1.1 The Capture Cross-section

For a narrow, well-isolated resonance, λ , of energy E_R and spin J , the partial radiative capture cross-section to a final state μ for an incident neutron of energy E is given by the Breit-Wigner formula,

$$\sigma_{\gamma\lambda\mu} = \sigma_0 \left(\frac{E_R}{E} \right)^{1/2} \frac{\Gamma_{\gamma\lambda\mu}}{4(E - E_R)^2 + \Gamma^2} \quad (2.1)$$

where $\Gamma_{\gamma\lambda\mu}$ is the partial radiative width and Γ is the total width, the sum of the widths of all open channels. The total cross-section peaks at the resonance energy, taking the value

$$\begin{aligned} \sigma_0 &= \frac{2\pi\hbar^2}{mE_R} \left(\frac{A+1}{A} \right)^2 \frac{g_J \Gamma_n}{\Gamma} \\ &= \frac{2.608 \times 10^6}{E_R(\text{eV})} \left(\frac{A+1}{A} \right)^2 \frac{g_J \Gamma_n}{\Gamma} \text{ barns} \end{aligned} \quad (2.2)$$

where m is the neutron mass, A is the mass number of the target nucleus and the statistical spin factor is

$$g_J = \frac{2J+1}{2(2I+1)} \quad (2.3)$$

for a target nucleus with spin I .

An expression for the partial radiative width may be derived within the framework of R-matrix theory (LT 58). Following a perturbation approach, applicable here since the coupling of nucleons to the electromagnetic field is small, and using the long-wave approximation for the E1 operator, the width for E1 radiation is given by (Lyn 68)

$$\Gamma_{\gamma\lambda\mu} = \frac{16\pi}{9(2J+1)} k_\gamma^3 |\langle X_\lambda || e r Y_1 || \Phi_\mu \rangle|^2 \quad (2.4)$$

where X_λ is the wave function of the resonance, Φ_μ is the wave function of the final state, e is the electronic charge [†], r is the radial co-ordinate and Y_1 is the spherical harmonic for one unit of angular momentum. The wave number of the gamma-ray, k_γ , is related to the energy by

$$k_\gamma = E_\gamma / \hbar c. \quad (2.5)$$

2.1.2 The Behaviour of Partial Radiative Widths

The cubic dependence on gamma-ray energy (eqn. 2.4) which comes from the phase space factor is often removed to give a reduced partial width,

$$\gamma_{\gamma\lambda\mu} = \Gamma_{\gamma\lambda\mu} / E_\gamma^3 \quad (2.6)$$

[†] If S.I. units are used, factors of e^2 should be replaced by $e^2/4\pi\epsilon_0$.

which is proportional to the square of the reduced matrix element $\langle X_\lambda || e r Y_1 || \Phi_\mu \rangle$. If the initial state is complicated, in the spirit of the compound nucleus model, then this matrix element will be distributed as a Gaussian with zero mean. This follows from a consideration of the multi-dimensional overlap integral involved in the matrix element. If the integral is considered as made up of the sum of many independently contributing cells (PT 56), then the central limit theorem may be invoked to deduce the Gaussian distribution. This in turn implies that the reduced partial width should be distributed as the χ^2 function with one degree of freedom i.e. a Porter-Thomas distribution, implying widely fluctuating values.

The reduced matrix element in eqn. (2.4) depends on the nuclear structure of the compound nucleus, permitting information to be derived concerning the capture process. A correlation of $\gamma_{\lambda\mu}$ with Γ_n (which is a measure of the component of the resonance consisting of incident neutron plus unperturbed core) implies that the unperturbed core configuration plays a part in the capture channel. Similarly, since the (d,p) reaction involves a neutron being stripped from a deuteron whilst the target nucleus acts as an inert core, correlations of the reduced width with the spectroscopic factors obtained from (d,p) measurements indicate the rôle of the single particle nature of the final state in the capture process.

A study of the behaviour of partial radiative widths can thus be seen to provide information on the capture process, the nuclear structure of the final state and the applicability of the statistical model.

2.2 The Strong Coupling Model

This model was the first basic model of neutron capture, introduced by Blatt and Weisskopf (BW 52). Simplifying assumptions are made concerning the wave functions of the resonance and final states as applied in eqn. (2.4). First consider for simplicity a spinless particle bound in an s -state by the potential of the target nucleus, undergoing a transition to a low-lying, pure p -state. The resonance wave function may now be written as

$$X_\lambda = u_0(r)\phi_0 \quad (2.7)$$

whilst the final state is

$$\Phi_\mu = u_1(r)\phi_0 \quad (2.8)$$

where the u are radial wave functions and ϕ_0 contains the wavefunction of the target nucleus plus all the angular dependence. The separation of the radial and angular dependence of the wave functions allows eqn. (2.4) to be rewritten as

$$\begin{aligned} \Gamma_{\gamma sp} &= \frac{16\pi}{9} k^3 \left(\bar{e} \int_0^\infty u_0(r) u_1(r) r dr \right)^2 |\langle J=0 || Y_1 || J=1 \rangle|^2 \\ &= \frac{4\pi}{3} \left(\frac{E_\gamma}{\hbar c} \right)^3 \left(\bar{e} \int_0^\infty u_0(r) u_1(r) r dr \right)^2 \end{aligned} \quad (2.9)$$

where \bar{e} , the effective charge of the neutron takes the value $-Z/A$ times the proton charge. This is derived by assuming the centre of mass of the nucleus to remain fixed during emission of a gamma-ray. The result follows since a movement of a single neutron through distance δ then implies a movement of the centroid of charge (the Z protons) through a distance $-\delta Z/A$.

The strong coupling model assumes that the total s -state single particle strength calculated above is dissolved amongst all the s -wave resonances. If the single

particle energy spacing is D_0 and the average spacing of s -wave resonances is $\overline{D}(l=0)$, then the partial radiative width for a resonance should on average be diluted by the factor $\overline{D}(l=0)/D_0$, giving

$$\overline{\Gamma}_{\gamma s p} = \frac{4\pi}{3} k^3 \left(\overline{e} \int_0^{\infty} u_0(r) u_1(r) r dr \right)^2 \frac{\overline{D}(l=0)}{D_0}. \quad (2.10)$$

If the final p -state is also fragmented amongst several levels, a typical partial width will be further reduced.

Blatt and Weisskopf made a rough estimate of the radial integral by assuming the wave functions to be uniform within the nuclear radius, a , and zero outside. The final estimate of the average partial width then becomes

$$\overline{\Gamma}_{\gamma \lambda \mu} = \frac{3}{4} e^2 \left(\frac{E_\gamma}{\hbar c} \right)^3 a^2 \frac{\overline{D}(l=0)}{D_0}. \quad (2.11)$$

Originally D_0 was thought to be about 0.5 MeV, the spacing of low-lying levels in the nucleus, but this gives estimates of the radiative width which are too large by about two orders of magnitude. When a realistic value is taken for D_0 (15–30 MeV) and more accurate radial wave functions are used in the integral, the discrepancy with experiment is reduced to a factor of 5 or so.

Despite its crudity and the need for empirical normalisation factors, the strong coupling model is still widely used in calculating neutron capture cross-sections up to neutron energies of 1 or 2 MeV.

2.3 The Giant Dipole Resonance Model

An alternative approach to calculating the average partial radiative width is to consider the inverse photo-absorption reaction. The broad peak in the photonuclear cross-section at energies between 10 and 20 MeV was interpreted by Goldhaber and Teller in terms of the giant dipole resonance model (GT 48). They considered the giant resonance to be a collective mechanism in which the proton and neutron fluids oscillated independently in anti-phase within the nucleus. The form of the absorption cross-section was predicted to be Lorentzian in shape and, for photon energies E_γ below the $(\gamma, 2n)$ threshold, this implies a (γ, n) cross-section of

$$\sigma(\gamma, n) = \frac{\sigma_0 \Gamma_g^2 E_\gamma^2}{(E_\gamma^2 - E_g^2)^2 + \Gamma_g^2 E_\gamma^2}. \quad (2.12)$$

where σ_0 is the peak cross-section of the giant resonance at energy E_g , having width Γ_g .

Using the reciprocity theorem for nuclear reactions, the cross-section for the inverse reaction may be deduced,

$$\sigma(n, \gamma) = \sigma(\gamma, n) \frac{E_\gamma^2}{\hbar^2 c^2 k^2} \quad (2.13)$$

where k is the wave number of the neutron. If an extrapolation of the Lorentzian as far down as the neutron threshold region is assumed to be valid, then the relationship between the average neutron capture cross-section to the ground state and the mean radiative width for such a transition,

$$\bar{\sigma}(n, \gamma_0) = \frac{2\pi^2 g_J}{k^2} \frac{\bar{\Gamma}_{\gamma\lambda 0}}{\bar{D}(J)} \quad (2.14)$$

may be used to derive the relationship

$$\bar{\Gamma}_{\gamma\lambda 0} = \frac{\bar{D}(J)\sigma_0}{2\pi^2 \hbar^2 c^2 g_J} \frac{\Gamma_g^2 E_\gamma^4}{(E_\gamma^2 - E_g^2)^2 + \Gamma_g^2 E_\gamma^2} \quad (2.15)$$

where $\bar{D}(J)$ is the average spacing of resonances of spin J .

This is an expression for the average partial radiative width to the ground state only. However, the Brink hypothesis may be introduced (Bri 55) in which it is assumed that identical giant resonances may be built on the excited states of nuclei. It then follows that the gamma-ray energy dependence of the cross-section is independent of the excitation energy of the final state and the expression above is a measure of the average radiative strength for all possible primary transitions. Carrying out an extrapolation of eqn (2.15) to the neutron threshold region with $\Gamma_g = 5$ MeV, $E_g = 80 A^{-1/3}$ and $\sigma_0 = 13 A \Gamma_g^{-1}$ mb, Axel (Axe 62) was able to show that for gamma-ray energies around 7 MeV, to a good approximation,

$$\bar{\Gamma}_{\gamma\lambda\mu}(eV) = 6.1 \times 10^{-15} \bar{D}(J)(eV) E_\gamma (MeV)^5 A^{8/3}. \quad (2.16)$$

The width is thus predicted to have a fifth power dependence on the gamma-ray energy in direct contradiction with the strong coupling model. Despite the assumption that the Lorentzian form for the absorption cross-section is still valid when applied at neutron separation energies (5 – 10 MeV) which are two or three half-widths from the peak, this model appears to describe the systematics of photon strength better than the strong coupling model, at least for $A \geq 60$ (McC + 81). It also confirms the empirical fact of harder gamma-ray spectra than are predicted from the cubic gamma-ray energy dependence of the single particle model.

An illustration of the validity of the energy dependence suggested by eqn. (2.16) is given in Figure 2.1 which shows data for the radiative widths reduced by the factor E_γ^3 , averaged over resonances in ^{196}Pt . It is clear that, in the region 6 – 8 MeV, the Lorentzian shape is approximated by an E_γ^5 curve and that the experimental data, taken from (BT 67), is described poorly by the strong coupling model but well by the giant dipole extrapolation.

2.4 The Lane–Lynn Theory

2.4.1 The Resonant Capture Components

Despite the apparent success of the giant dipole resonance model in predicting the average radiative strength, it is still unable to explain the observed non-statistical effects. The Lane–Lynn theory (LL 60) is a rigorous treatment of the capture reaction and allows inclusion of non-statistical processes.

The starting point of the Lane–Lynn theory was to derive an expression for the collision matrix, U , which is related to the cross-section by the expression

$$\sigma_{\gamma\lambda\mu} = \frac{\pi}{k^2} \sum_J g_J |U_{\gamma\lambda\mu}^{(J)}|^2. \quad (2.17)$$

The collision matrix was split into three components, dropping the superscripts and subscripts which are to be understood,

$$U = U(\text{internal resonance}) + U(\text{channel resonance}) + U(\text{hard sphere}) \quad (2.18)$$

where the first two components are resonant in nature. The hard sphere term is non-resonant and will be neglected for the time being. The sum of the two resonant terms has the form

$$U(res) = -ie^{-i\phi} \sum_{\lambda} \frac{\Gamma_{n\lambda}^{1/2} (\Gamma_{\gamma\lambda\mu}^{1/2} + (\delta\Gamma_{\gamma\lambda\mu})^{1/2})}{E_{\lambda} - E - i\Gamma_{\lambda}/2} \quad (2.19)$$

which for a single resonance can readily be seen to reproduce the Breit-Wigner form, eqn. (2.1), when applied in eqn. (2.17), and where the partial radiative widths for the internal and channel resonance components are given respectively by

$$\Gamma_{\gamma\lambda\mu}^{1/2} = \left(\frac{16\pi}{9(2J+1)} \right)^{1/2} k_{\lambda}^{3/2} \langle X_{\lambda}^{int} \| erY_1 \| \Phi_{\mu} \rangle \quad (2.20)$$

and

$$(\delta\Gamma_{\gamma\lambda\mu})^{1/2} = \left(\frac{16\pi}{9(2J+1)} \right)^{1/2} k_{\lambda}^{3/2} \langle X_{\lambda}^{ch} \| erY_1 \| \Phi_{\mu} \rangle. \quad (2.21)$$

These expressions are seen to be identical except that the first width is integrated over the internal region only, using the resonance internal wave function X_{λ}^{int} , whereas the second width is integrated over the external region with the channel wave function, X_{λ}^{ch} . A new wave function, X_{λ}^e may be defined

$$\begin{aligned} X_{\lambda}^e &= X_{\lambda}^{int} & r \leq a \\ &= X_{\lambda}^{ch} & r > a \end{aligned} \quad (2.22)$$

where a is the channel radius. With the integral carried out over all space, the resonant partial radiative width is now given by (cf. eqn. (2.4))

$$\Gamma_{\gamma\lambda\mu} = \frac{16\pi}{9(2J+1)} \left(\frac{E_{\gamma}}{\hbar c} \right)^3 |\langle X_{\lambda}^e \| erY_1 \| \Phi_{\mu} \rangle|^2 \quad (2.23)$$

2.4.2 Channel Capture

Lane and Lynn (LL 60) showed that the channel component to resonance capture, eqn. (2.21) could, in suitable circumstances be larger than the internal resonance part by an order of magnitude. They derived an expression for the channel capture width from eqn. (2.21),

$$\Gamma_{\gamma\lambda\mu}^{ch} = \frac{64\pi}{9} k_{\gamma}^3 \theta_{\mu}^2 \theta_{\lambda}^2 \frac{\bar{e}^2}{k_{\mu}^2} \frac{|\langle J_{\lambda} \| Y_1 \| J_{\mu} \rangle|^2}{2J_{\lambda} + 1} \quad (2.24)$$

where k_{μ} is the wave number for a neutron bound by energy E_{γ} and θ_{λ}^2 , θ_{μ}^2 are the spectroscopic factors of the initial and final states respectively. The initial state spectroscopic factor is given by the ratio of the neutron width to the single particle Wigner limit,

$$\theta_{\lambda}^2 = \frac{\Gamma_n}{\Gamma_n^W} = \frac{\Gamma_n}{\frac{2k\hbar^2}{ma}} \quad (2.25)$$

and the final state spectroscopic factor comes from (d,p) measurements. If the channel radius, a , is taken to be $1.35 A^{1/3}$, then

$$\Gamma_{\gamma\lambda\mu}^{ch} \approx 6.44 \times 10^{-3} \frac{E_{\gamma}(\text{MeV})^2}{\sqrt{E}(\text{eV})} \left(\frac{Z}{A} \right)^2 A^{1/3} \Gamma_n \theta_{\mu}^2 |A.M.|^2 \quad (2.26)$$

where the angular momentum coupling factor, $|A.M.|^2$, is $1/4\pi$ for an $s \rightarrow p_{1/2}$ transition and $1/2\pi$ for an $s \rightarrow p_{3/2}$ transition.

This illustrates that channel capture shows a square dependence on gamma-ray energy unlike the single particle model. The proportionality with spectroscopic factors of the initial and final states is an important prediction and indicates that channel capture effects should be observed most readily in cases where the reduced neutron width and (d,p) final state spectroscopic factors are large.

2.4.3 Non-Resonant Capture

The third term in the collision matrix expansion eqn. (2.18) will now be considered. This arises from the potentially scattered wave function which is present even in off-resonance regions. In this case the wave function of the initial state has a node at the nuclear surface and, assuming a strong coupling model, it does not penetrate the nucleus; the nucleus is behaving as a hard sphere. For capture to a final p -wave state, Lane and Lynn derived the following expression

$$\sigma_{\mu}(hard\ sphere) = \frac{0.062}{a\sqrt{E}} \left(\frac{Z}{A}\right)^2 \sum_{s'} \frac{2J_{\mu} + 1}{6(2I + 1)} \theta_{\mu}^2 y^2 \left(\frac{y + 3}{y + 1}\right)^2 \text{ barns} \quad (2.27)$$

where $y = k_{\mu} a$ and a is the hard sphere radius, taken to be the nuclear radius. The statistical spin factor sum over s' accounts for the effect of limitations imposed by the angular momentum coupling and only channel spins s' satisfying $J_{\mu} = s' + I_{\mu}$ should be included (here $I_{\mu} = 1$).

In the intermediate coupling assumption, there is another component to the non-resonant capture cross-section. This contribution arises from non-local levels in the resonance terms of the collision matrix eqn. (2.18). The sum of the hard sphere term and the distant resonance terms (both internal and channel) is called the potential capture term. The collision matrix may thus be rewritten as

$$U = U(local\ res) + U(pot) \quad (2.28)$$

where

$$U(pot) = U(hard\ sphere) + U(distant\ res) \quad (2.29)$$

Physically this corresponds to the penetration of the nuclear surface by the incoming wave function, allowed in the intermediate coupling model due to the finite mean free path of a nucleon within the nucleus. (Mathematically, with the strong coupling model, the signs of the distant resonant terms were random and the overall contribution was zero.) It can be shown that the potential capture can be calculated in the intermediate coupling model by evaluation of the same overlap integral used in hard sphere capture but taking the real part of an optical model wave function for the initial state (LL 60). Such calculations predict that the potential capture cross-section has a double peak in the 3s mass region (see Figure 2.2).

The form of the collision matrix above (eqn. 2.28) shows that in principle there may be interference between the resonance term and the potential capture resulting in asymmetric capture resonances. Experimental evidence of any such effect is not conclusive.

2.4.4 Thermal Capture

In certain nuclides there are no resonance levels near to the neutron separation energy and such circumstances provide a good testing ground for the Lane-Lynn

theory. Within the strong coupling model, the capture cross-section is given by the hard sphere term of eqn. (2.18) but channel contributions from nearby (although not dominant) levels may also be included (distant levels and nearby internal resonance contributions will be ignored). The effect of this channel contribution is to enhance the hard sphere capture by a calculable factor, giving

$$\sigma_{\gamma\mu}(\text{thermal}) = \sigma_{\gamma\mu}(\text{hardsphere}) \left[1 + \frac{(a - a_s)}{a} y \frac{y+2}{y+3} \right]^2 \quad (2.30)$$

where a_s is the coherent scattering length for thermal neutrons. The effect of the correction factor due to resonance channel terms can be very large if the nuclear radius a is significantly different from the scattering length. Good agreement in absolute terms has been found (see references in chapter 1).

Finally, it should be noted that this predicted thermal cross-section depends (approximately) linearly on the gamma-ray energy and so when looking for correlations with final state spectroscopic factors a reduction factor of E_γ rather than E_γ^3 should be used. An example of the improvement in correlations which may be obtained by applying a reduction factor of E_γ raised to a smaller power, is the case of thermal capture in ^{37}Cl (SA 73) which is illustrated in Figure 2.3. Here a reduction factor of $E_\gamma^{1.2}$, which maximizes the observed correlation, is compared with application of the normal E_γ^3 factor.

2.5 Valence Neutron Transitions

2.5.1 Average Partial Widths

It is possible to make an estimate of the resonance internal contribution as well as the channel capture if certain simplifying assumptions are made and applied to the general eqn. (2.23). Lynn (Lyn 68) considered the part played by the valence neutrons i.e. single particle transitions in the presence of an inert core. Firstly, a suitable basis set, χ_{pc} , is chosen on which to expand the initial wave function

$$\chi_{pc} = u_p(r)\phi_c \quad (2.31)$$

where $u_p(r)$ are radial wave functions of a set of single particle states p , and ϕ_c contain the wave function of the core, the angular momentum coupling of the core to the single particle and the angular dependence of the single particle. On this basis the resonance wave function is then given by the expression

$$X_\lambda = \sum_{cp} C_{cp}^\lambda u_p(r)\phi_c \quad (2.32)$$

where the C_{cp}^λ are coefficients of fractional parentage. This wavefunction is taken to apply over all space; the single particle moves in the potential provided by the inert core.

If the final state is also expressed in terms of a single-particle plus core expansion,

$$\Phi_\mu = \sum_{c'p'} C_{c'p'}^\mu u_{p'}(r)\phi_{c'} \quad (2.33)$$

then the expression for the partial width, eqn. (2.23), becomes

$$\Gamma_{\gamma\lambda\mu} = \frac{16\pi}{9(2J+1)} k_\gamma^3 \sum_{cc'pp'} |\langle C_{cp}^\lambda u_p(r)\phi_c || e r Y_1 || C_{c'p'}^\mu u_{p'}(r)\phi_{c'} \rangle|^2 \quad (2.34)$$

The core is considered to be inert so all terms for which $c \neq c'$ drop out of the sum.

This assumption has been justified by Lane (Lan 59) where he argues that the many possible core-core transition terms should have random signs and not add coherently. In addition, as any reasonable amount of mixing of single particle states will lead to random signs for the coefficients of fractional parentage, all the cross-terms drop out and the average partial valence width is given by

$$\bar{\Gamma}_{\gamma\lambda\mu}^v = \frac{16\pi}{9(2J+1)} k_\gamma^3 \sum_{cpp'} \overline{(C_{cp}^\lambda)^2 (C_{c'p'}^\mu)^2} \left| \bar{e} \int_0^\infty u_p(r) u_{p'}(r) r dr \right|^2 \times |\langle j_p I_c J_\lambda \| Y_1 \| j_{p'} I_c J_\mu \rangle|^2 \quad (2.35)$$

where j_p , the angular momentum of state p , is coupled to the spin of the core, I_c , to give the total angular momentum of the resonance, J_λ and similarly state p' couples its angular momentum $j_{p'}$ to the core spin to give the final state angular momentum J_μ .

Lynn derived an estimate for the value of $\overline{(C_{cp}^\lambda)^2}$ by invoking the intermediate coupling model for which only one single particle state would play a large part in the resonance wave function. For its absolute value however he took the strong coupling model prediction for the neutron strength function. For the value of $\overline{(C_{c'p'}^\mu)^2}$ he assumed that the total strength of these states summed to the Wigner sum rule (TW 52) and that this could be averaged out amongst the levels since the resonance state was sufficiently complex that all core states appearing in Φ_μ were also present in X_λ . These assumptions lead to

$$\bar{\Gamma}_{\gamma\lambda\mu} = \frac{16\pi}{9(2J+1)} k_\gamma^3 \frac{1}{\pi K a} \frac{4m}{\hbar^2} \overline{u_p^{-4}(a)} \bar{D}(J) \times \sum_p \left| \bar{e} \int_0^\infty u_p(r) u_{p'}(r) r dr \right|^2 |\langle j_p I_c J_\lambda \| Y_1 \| j_{p'} I_c J_\mu \rangle|^2 \quad (2.36)$$

where K is the average wave number of a neutron in the nuclear potential and the final average denotes the average of the sum of the squared matrix elements to a specific single particle state p' .

Typical values for the radial integral were derived by calculating single particle wave functions for particles moving in a Saxon-Woods potential with a spin-orbit coupling term added. The parameters of the potential were those of Ross *et al* (Ros + 56). Lynn allowed the neutron to be bound by up to 1 MeV which takes account of the fact that excited core terms are being included in the calculation and only for unexcited cores should the neutron be unbound. The spin matrix elements were also averaged over possible angular momentum values enabling the global estimate of partial widths to be made,

$$\bar{\Gamma}_{\gamma\lambda\mu}(eV) = 0.16 \times 10^{-9} E_\gamma^3 (MeV) A^{5/6} \bar{D}(J)(eV). \quad (2.37)$$

This compares favourably with an empirical fit due to Cameron, derived from total radiative widths (Cam 59),

$$\bar{\Gamma}_{\gamma\lambda\mu}(eV) = 0.33 \times 10^{-9} E_\gamma^3 (MeV) A^{2/3} \bar{D}(J)(eV). \quad (2.38)$$

2.5.2 The Specialised Valence Model

Following the success of the global fit to average partial radiation widths using valence transitions, a further specialisation was applied, initially by Mughabghab (Mug + 71), where only the unexcited core components of the initial and final states were considered. In this case eqn. (2.35) becomes

$$\Gamma_{\gamma\lambda\mu}^v = \frac{16\pi}{9(2J+1)} k_\gamma^3 (C_{0p}^\lambda)^2 (C_{0p'}^\mu)^2 \left| \bar{e} \int_0^\infty u_p(r) u_{p'}(r) r dr \right|^2 \times |\langle j_p I_c J_\lambda || Y_1 || j_{p'} I_c J_\mu \rangle|^2 \quad (2.39)$$

where only a particular transition, p to p' , is being considered in the presence of an unexcited core.

This expression may be evaluated if the spectroscopic factors $(C_{0p}^\lambda)^2$ and $(C_{0p'}^\mu)^2$ are known. $(C_{0p}^\lambda)^2$ may be derived from a measurement of the neutron width and a comparison with the single particle neutron width, Γ_{nsp} ,

$$(C_{0p}^\lambda)^2 = \frac{\Gamma_{\lambda\mu}}{\Gamma_{nsp}}. \quad (2.40)$$

The value for $(C_{0p'}^\mu)^2$ is the spectroscopic factor for the (d,p) stripping reaction to state μ .

In this special case, the initial state of the neutron is not bound so Lynn's values for the radial integrals, used by Mughabghab, were incorrect. In addition, there are uncertainties in the value of Γ_{nsp} to be used since the Wigner limit which is normally adopted (TW 52), eqn.(2.25), applies only to the case of a square well potential. A correction which can be applied for a more realistic well having diffuseness d has been given by Vogt (Vog 62),

$$\Gamma_{nsp} = (1 + 6.7d^2)\Gamma_n^W \quad (2.41)$$

but the approach is clearly not very satisfactory and such considerations have led to the suggestion of alternative formulations of the valence model.

2.5.3 Alternative Forms for the Valence Model

Lane and Mughabghab (LM 74) used an optical model wave function at neutron energy E , $\psi_E^{(opt)}$, to describe the initial state. To extract the valence part of the capture process it is necessary to evaluate the dipole matrix element between the target state component of the initial state and the target state component of the final state, these components being defined respectively as

$$u_E^{(opt)} = \langle \phi_0 | \psi_E^{(opt)} \rangle \quad (2.42)$$

and

$$u_\mu = \langle \phi_0 | \Phi_\mu \rangle \quad (2.43)$$

where ϕ_0 is the target ground state. The expression for the valence width is then

$$\begin{aligned} \Gamma_{\gamma\lambda\mu}^v &= \left[\frac{Im \langle u_\mu | D | u_E^{(opt)} \rangle}{Im \tan \delta_{(opt)}} \right]^2 \cdot \Gamma_{\lambda n} \\ &= \frac{8\pi^2}{9} e^2 \left(\frac{Z}{A} \right)^2 k_\gamma^3 \theta_\mu^2 \Gamma_{\lambda n} \left[\frac{Im \langle w_\mu(r) | r | w_E^{(opt)}(r) \rangle}{Im \tan \delta_{(opt)}} \right]^2 \\ &\quad \times |\langle j_p I_c J_\lambda || Y_1 || j_{p'} I_c J_\mu \rangle|^2 \end{aligned} \quad (2.44)$$

where the w are the radial components of the wavefunctions.

The essential features of the valence model are seen to be retained since the width is proportional to the spectroscopic factors of the initial and final states. However, it is now also apparent that there is a dependence on the resonance energy through the optical model wave function in the overlap integral.

Another approach, adopted by Boridy and co-workers, was to use a shell model formulation of the reaction (BM 73 and CM 75). Although their approach should be equivalent to Lane and Mughabghab's, they define their observable radiative width differently. The apparent disagreement in values between Cugnon (Cug 76) and Allen and Musgrove (AM 79) was noted by the latter authors but it can be shown that formally they are identical (Lan 82) and that Lane and Mughabghab's definition provides a more useful value of the width for comparison with experiment.

The various methods for evaluating the valence width have been compared by Halderson and Castel (HC 78) who conclude that the optical model formulation of Lane and Mughabghab is the most useful one to use since it does not rely on an evaluation of Γ_{nsp} , it includes external contributions to the photon width, and the predictions are not very sensitive to the potential employed. It is therefore through use of eqn. (2.44) that the calculations described in the next section have been carried out.

2.6 Valence Model Calculations

2.6.1 Initial and Final State Wave Functions

Attention is restricted to the mass range of interest in which valence transitions are of the form $3s$ to $2p_{1/2}$ and $3s$ to $2p_{3/2}$.

The main task in evaluating the valence width expression eqn. (2.44) is to identify the phase shift, $\delta_{(opt)}$, and the radial matrix element. Firstly, solutions for the wave functions are found by solving the Schrödinger equation for a particle in the initial and final state potentials. For a central potential, $V(r)$, the wave function ψ corresponding to motion with angular momentum l may be split into radial and angular parts in the normal way

$$\psi_{Elm}(r, \theta, \phi) = w_E(r) Y_{lm}(\theta, \phi). \quad (2.45)$$

Here Y_{lm} is the spherical harmonic corresponding to angular momentum l , and m is the z -component of angular momentum. The spin part of the wavefunction is being ignored. The radial wavefunction $w_E(r)$ is determined by the equation

$$\frac{d^2}{dr^2} v_E(r) + \left(\frac{l(l+1)}{r^2} + \frac{2\mu}{\hbar^2} V(r) \right) v_E(r) = \frac{2\mu E}{\hbar^2} v_E(r) \quad (2.46)$$

where μ is the reduced mass of the system, E is the energy in the centre-of-mass frame and $v_E(r)$ is related to $w_E(r)$ by

$$v_E(r) = r w_E(r). \quad (2.47)$$

The radial equation was solved numerically using an optical model potential of the form

$$V_{opt}(r) = V_0 f(r) + i W_s g(r) + \left(\frac{\hbar}{m_\pi c} \right)^2 V_{so} \boldsymbol{\sigma} \cdot \mathbf{l} \frac{1}{r} \frac{df}{dr} \quad (2.48)$$

where the form factor for the volume potential was taken to be a Saxon-Woods

$$f(r) = \left[1 + \exp \left(\frac{r - R}{d} \right) \right]^{-1} \quad (2.49)$$

and the surface absorption form factor was a Gaussian

$$g(r) = \exp \left[- \left(\frac{r - R - c}{b} \right)^2 \right]. \quad (2.50)$$

No volume absorption term was included as at low energies it is known that surface absorption dominates (Hod 71). The factor $(\hbar/m_\pi c)^2$ was set to 2 fm^2 and the other constants were provided by fits to experimental data, as described below.

The initial state wave function was determined using the full (complex) optical model potential, specialised to the case $l = 0$, and with the value of E as the neutron resonance energy. Normalisation of the wave function, corresponding to unit flux incident on the target, was determined by the asymptotic behaviour of the wave function; for $l = 0$,

$$w_E^{(opt)}(r) \rightarrow \frac{1}{r} \sqrt{\frac{2\mu}{\pi \hbar^2 k}} (\sin kr + \tan \delta_{opt} \cos kr) \quad (2.51)$$

as $r \rightarrow \infty$. Matching of this asymptotic form with the numerical solution outside the range of the nuclear potential also provided the phase shift, δ_{opt} .

For the bound state wave function, only the real part of the optical potential was used. The value of E , which in this case is the binding energy of the low-lying $2p_{1/2}$ or $2p_{3/2}$ state, is initially unknown. E was therefore adjusted until the wave function behaved as a decaying exponential at large radii. Once the binding energy had been determined, the corresponding final state wave function was normalised to unity over all space. The solutions for the bound state energies were compared with values provided from other codes (Hod 82) and the agreement was excellent (within 0.3%).

An example of the radial wave functions, calculated for both initial and final states, is shown in Figure 2.4, together with the real part of the nuclear potential. The real and imaginary parts of the optical model wavefunction are in anti-phase near the origin since the imaginary part of the potential is zero except at the nuclear surface.

Details of the chosen method of solution of the differential equation (Nel 82) and the appropriate boundary conditions are given in Appendix A.

2.6.2 The Reduced Valence Width

In order to compare these current valence model calculations with previous estimates and also to make systematic trends clear, it is useful to define a reduced valence width parameter, $q(E)$, from which dependence on the gamma-ray energy and the spectroscopic factors has been removed (AM 79),

$$q(E) = \Gamma_{\gamma\lambda\mu}^v E_\gamma^{-3} \left(\frac{Z}{A} \right)^2 \theta_\mu^{-2} \Gamma_n^{-1} E^{1/2}. \quad (2.52)$$

The behaviour of q was examined using as a base the optical model parameters suggested by Moldauer (Mol 63):

$$\begin{aligned} V_0 &= -46 \text{ MeV}, & W_s &= -14 \text{ MeV}, & V_{so} &= 7 \text{ MeV}, \\ d &= 0.62 \text{ fm}, & b &= 0.5 \text{ fm}, & c &= 0.5 \text{ fm}, \\ R &= 1.16A^{1/3} + 0.6 \text{ fm}. \end{aligned}$$

He found that this choice of parameters provided good agreement with observations of the s -wave neutron strength function, total cross-section measurements up to 1 MeV and elastic scattering cross-sections.

The predicted behaviour of quantities of interest are given in Figures 2.5 and 2.6.

In Figure 2.5 the dependence on mass number of q and binding energy is given for final states of $p_{1/2}$ and $p_{3/2}$ character, whilst Figure 2.6 (a) shows the ratio of $q(E)$ to $q(E_{th})$ (which is the value of q for a resonance at thermal energy) for $A = 54$. Over the region of interest ($E \leq 100$ keV), the dependence on neutron energy for this mass region may clearly be neglected. However, if the well depth is varied (so changing the single particle binding energy) the variation in q is quite marked. This is illustrated in Figure 2.6 (b) for both $p_{1/2}$ and $p_{3/2}$ final states. On the log-log plot shown, q varies approximately linearly with binding energy, the slope indicating that $q \propto E_{\gamma}^{-1}$ where the binding energy has been associated with the gamma-ray energy. Thus an adjustment of the depth of the potential to provide agreement with observed gamma-ray energies implies, through eqn. (2.52), that the overall valence width varies as E_{γ}^2 in agreement with predictions for channel capture (eqn. 2.26). This is expected since the major contribution to the valence width comes from the external (channel) region when calculating the overlap integral.

It should be noted that the procedure of altering the potential until the energy of the final state is that of an observed level is unsatisfactory as the initial and final states will be non-orthogonal unless the optical model potential is also altered. The effect of varying the optical potential has thus been investigated.

The s -wave neutron strength function and the scattering radius implied by a particular optical model potential may be deduced from the calculated phase shift (see Appendix B). Figures 2.7 and 2.8 show a comparison with experimental data for these quantities as the real and imaginary parts of the optical potential are varied. The experimental data on the figures is taken from the compilation of Mughabghab *et al* (Mug + 81).

The behaviour with variations in the value of V_0 (the radius is fixed so the product $V_0 r^n$ is being varied), suggests (see Figure 2.7) that over this mass range a value of $V_0 = -44$ MeV would provide a better fit to the two observed quantities than the original potential of Moldauer. However, the data are rather poor and no fit appears to be very good so it would therefore seem that alterations of the well depth by up to 2 MeV should be permissible. The effect on the reduced valence width prediction for similar changes in V_0 is shown in Figure 2.9 where ± 2 MeV variation in V_0 gives rise to $\pm 5\%$ change in q .

As the imaginary part of the potential, W_s , is varied by ± 5 MeV, large changes are produced in the two observables (Figure 2.8). However, a similar variation produced $< 1\%$ change in q . Uncertainties in the value of W_s are therefore not important.

These considerations suggest that the value of q to be adopted should be that calculated with the well depth adjusted to give the binding energy of the observed level, provided that the required well depth does not differ too much from the Moldauer value. An error of 10% is ascribed to this value to account for the uncertainty of the optical model parameters.

2.6.3 The Particular Cases ^{54}Fe and ^{62}Ni

To apply eqn. (2.52) to ^{54}Fe and ^{62}Ni , experimental data must be used for the gamma-ray energies, the spins and spectroscopic factors of the possible final states and the neutron widths of the resonances. Only the lowest energy s -wave resonance in each nuclide is considered and values for their widths and energies were taken from the compilation of Mughabghab *et al* (Mug + 81).

Details of the final states are shown in Tables 2.1 and 2.2 where only those states known to be either $p_{1/2}$ or $p_{3/2}$ are given. The energy and spin assignments are those given in the evaluations of Auble for ^{63}Ni (Aub 79) and Enchen *et al* for ^{55}Fe (Enc + 85).

The spectroscopic factors of the states come from (d,p) measurements. The data for ^{55}Fe show a considerable spread of $\sim 30\%$ although the agreement between (FM 63) and (KH 72) gives variations of only $\sim 10\%$. The values adopted for this study are therefore those of the evaluation by Enchen *et al* but with an uncertainty of 10%. The ^{63}Ni data appear to be much more consistent and the adopted values are those of (Anf + 70). Although the quoted measurements agree to within 2%, it seems unreasonable that this is a good estimate of the true errors since systematic errors due to the similar analysis method may well be quite large. An error of 10% is therefore tentatively proposed for these data also.

The final calculations for the two nuclides are presented in Tables 2.3 and 2.4, where the overall uncertainty in the valence width is estimated from the (independent) contributions of the calculation of q (10%), the spectroscopic factors (10%) and the neutron widths (2% for ^{54}Fe and 10% for ^{62}Ni). This gives an overall error of $\approx 15\%$ for ^{54}Fe and $\approx 20\%$ for ^{62}Ni although a large part of the errors for individual transitions may be correlated.

Table 2.1

Summary of available data of the spectroscopic factors for $1/2^-$ and $3/2^-$ states in ^{55}Fe . The spin-parity assignments J^π and energy levels E_x are from a recent evaluation (Enc + 85). The identification of the 3.8 MeV level as $1/2^-$ is taken from (KH 72).

$E_x(\text{MeV})$	J^π	Spectroscopic factor				
		(KH 72)	(TC 80)	(FM 63)	(MP 64)	(Enc + 85)
0.0	$3/2^-$	0.73	0.58	0.81	0.46	0.78
0.413	$1/2^-$	0.59	0.3	0.60	0.31	0.6
1.925	$1/2^-$	0.07	0.04	0.13	0.03	0.1
2.058	$3/2^-$	0.08	0.07	0.09	0.04	0.09
2.478	$3/2^-$	0.15	0.1	0.19	0.08	0.17
3.035	$3/2^-$	0.03		0.02	0.01	0.03
3.559	$3/2^-$	0.11	0.09	0.13	0.06	0.12
3.800	$1/2^-$	0.50		0.7	0.34	0.6
5.775	$3/2^-$	0.04		0.05		0.05

Table 2.2

Summary of available data of the spectroscopic factors for $1/2^-$ and $3/2^-$ states in ^{63}Ni . The spin-parity assignments J^π and energy levels E_x are from an evaluation (Aub + 79). The identification of the 1.327 MeV level as $3/2^-$ is taken from (Hut + 74).

$E_x(\text{MeV})$	J^π	Spectroscopic factor		
		(Anf + 70)	(FM 63)	(Aub 79)
0.0	$1/2^-$	0.37	0.38	0.37
0.155	$3/2^-$	0.28	0.27	0.28
0.515	$3/2^-$	0.08	0.08	0.08
1.003	$1/2^-$	0.33	0.33	0.33
1.327	$3/2^-$	0.13		0.06

Table 2.3

Calculation of the valence widths to final states E_x in ^{55}Fe following capture in the 7.76 keV resonance. The neutron width is taken to be 1060 ± 20 eV from (Mug + 81). The overall uncertainty in the valence width is estimated to be 15%.

$E_x(\text{MeV})$	$E_\gamma(\text{MeV})$	J^π	θ_μ^2	$q(\text{MeV}^{-3}\text{eV}^{1/2})$	Valence width (eV)
0.0	9.298	$3/2^-$	0.78	6.9	1.21
0.413	8.885	$1/2^-$	0.6	3.2	0.38
1.925	7.373	$1/2^-$	0.1	4.1	0.05
2.058	7.240	$3/2^-$	0.09	10.0	0.10
2.478	6.820	$3/2^-$	0.17	11.2	0.17
3.035	6.263	$3/2^-$	0.03	12.7	0.026
3.559	5.739	$3/2^-$	0.12	13.5	0.09
3.800	5.498	$1/2^-$	0.6	6.2	0.17
5.775	3.523	$3/2^-$	0.05	22.6	0.01

Table 2.4

Calculation of the valence widths to final states E_x in ^{63}Ni following capture in the 4.54 keV resonance. The neutron width is taken to be 1880 ± 200 eV from (Mug + 81). The overall uncertainty in the valence width is estimated to be 20%.

$E_x(\text{MeV})$	$E_\gamma(\text{MeV})$	J^π	θ_μ^2	$q(\text{MeV}^{-3}\text{eV}^{1/2})$	Valence width (eV)
0.0	6.838	$1/2^-$	0.37	5.0	0.34
0.155	6.683	$3/2^-$	0.28	12.0	0.57
0.515	6.323	$3/2^-$	0.08	12.7	0.15
1.003	5.835	$1/2^-$	0.33	6.1	0.23
1.327	5.511	$3/2^-$	0.06	6.5	0.04

3 EXPERIMENTAL TECHNIQUES

3.1 Introduction

3.1.1 Neutron Spectroscopy

The experimental investigation of neutron capture gamma-ray spectra in the resonance energy region requires the detection of gamma-rays as a function of neutron energy. For each event of interest, it is thus necessary to record the energy of the gamma-ray which is observed and the energy of the neutron which gives rise to the capture event.

A Ge detector may be used to observe the capture gamma-rays, and it provides the necessary information on the gamma-ray energy, with a resolution of typically 0.2%. The timing of the gamma-ray event may also be determined in such a detector, a typical jitter achievable being 5 ns, and this may be used to determine the neutron energy with the time-of-flight technique.

The time-of-flight technique is the most widely applied method for determining neutron energies in the resolved resonance energy region and was used in these investigations. A 'white' spectrum of neutrons is produced in a short burst from a suitable machine such as an electron linear accelerator (linac) or a Van de Graaff generator. The neutrons travel down an evacuated flight path and interact with the chosen sample or detector at a station situated a distance l from the source. The time t between the neutron burst and detection of an event, known as the time-of-flight, determines the neutron energy E through the (non-relativistic) relation

$$t = \frac{72.296 l(m)}{\sqrt{E(eV)}} \mu s. \quad (2.1)$$

The neutron energy resolution which may be achieved is determined by a number of factors, which lead to uncertainties in either the flight path length or else the timing of the events. For example, uncertainty arises in the flight path length due to the finite thickness of the sample and the neutron target, and the angle at which the flight path is positioned to the source. An uncertainty in the timing of the event may come from the finite resolution of the detector, the width of the beam burst, and any contribution from the binning of events into particular timing channels. If the total uncertainties (FWHM) due to timing and flight path length are Δt and Δl respectively, then the energy resolution is given by

$$\frac{\Delta E}{E} = 2\sqrt{\left(\frac{\Delta t}{t}\right)^2 + \left(\frac{\Delta l}{l}\right)^2}. \quad (2.2)$$

In order to obtain the best resolution, the uncertainties Δt and Δl should be made as small as possible, but in addition it is clear that, for any given neutron energy, an increase in l will improve the resolution. The penalty which must be paid for using a longer flight path is the smaller flux then available, and a suitable compromise must therefore be reached between count-rate and resolution. Another factor to be borne in mind when choosing a flight path length is the effect of the gamma flash which is present on a pulsed machine such as an electron linac. This intense burst of gamma-rays which accompanies every pulse of the machine is caused by *bremsstrahlung* in the target as the electrons slow down. If the detector is sensitive to gamma-rays, this will tend to disable detection for a period of time, and

the recovery period will be longer for a short flight path where the gamma flash is more intense.

When working at a high pulse repetition rate, it is necessary to take some measures to ensure that slow neutrons from one pulse are not present when observing the fast neutrons of the next pulse. This may be achieved by inserting a boron filter of suitable thickness in the neutron beam. This has a large thermal cross-section due to absorption in ^{10}B , but with a $1/v$ energy dependence. It is thus possible to attenuate the overlap neutrons by a suitable large factor whilst still allowing a reasonable flux of resonance energy neutrons to pass through. An attenuation of 10^4 at the overlap energy, which depends on the machine pulse repetition frequency as well as the flight path length, is generally considered to be sufficient in a capture experiment (Mox 82).

3.1.2 Data Collection

As the experimental observation of neutron capture gamma-ray spectra requires the recording of two parameters for every event, each with good resolution, the demands imposed on data collection are quite severe. A computer is required in order to cope with the large quantity of data which is accumulated, and several different methods have been employed in the past:

- (i) event-by-event recording
- (ii) gamma-ray spectra collection in selected time bins
- (iii) accumulation of a 2-D histogram.

In method (i), whenever an event occurs, the two parameters are recorded together without any form of sorting. They are held temporarily in buffers or on disc in the computer until it is convenient to write the data to a magnetic tape. The advantage of this system is that there is virtually no limit to how many bits of information may be ascribed to each of the parameters to be recorded. The disadvantage is that whilst data collection is taking place, there is no simple way to view the time-of-flight or gamma-ray spectra, as finding the contents of a particular channel (the number of events which have occurred within specified neutron and gamma-ray energy ranges) requires a search through all the events which have been recorded up to that time.

In method (ii) several timing bins are set initially which correspond to neutron energies of known resonances. For each bin, the gamma-ray spectrum is accumulated separately within the computer, using a code for the particular timing bin (resonance) in which the gamma-ray occurred. This allows on-line inspection of the capture spectra of the resonances of interest. The method is useful if no information is required on the shape of the resonance and all resonances are known beforehand, but it is not a very flexible approach since much of the available information has been thrown away before any analysis.

Method (iii) is used when it is required that all the information is retained, whilst still allowing spectra to be observed on-line when required. A 2-D histogram is set up on disc in the computer, with axes corresponding to the time-of-flight and the gamma-ray energy. Each event which occurs increments the appropriate channel, and spectra for the two parameters may be viewed by displaying the histogram of one parameter summed over given channels of the other parameter. It thus contains the best features of each of the above methods, the limitation on its use being principally the storage and speed requirements imposed on the data collection computer.

The method adopted for these investigations was the third one, given the advantages outlined above. Once all the data had been collected, with off-line analysis it was possible to observe gamma-ray spectra in regions away from a resonance (i.e. background), the resonance shapes (allowing shape analysis) and the identification of small resonances. Other features of this method are the ability to observe the timing response of the detection system as a function of gamma-ray energy (i.e. walk) and in principle the unequivocal identification of a capture gamma-ray as a primary transition by observation of the associated shift in gamma-ray energy as the incident neutron resonance energy changes. Overall, the method was shown to be a very powerful one.

3.2 The Neutron Source and Flight Path

3.2.1 The 136 MeV Harwell Linac – HELIOS

The neutron source used for these investigations was the Harwell 136 MeV electron linac HELIOS (Harwell Electron Linear accelerator for the Investigation Of radiation and neutron Science). The general layout of the machine is shown in Figure 3.1. It was officially opened in 1979, the fourth in a series of linacs at Harwell, each one being more powerful than its predecessor.

HELIOS is an electron linac of the travelling wave type in which a pulse of r.f. power, produced by klystrons, is transmitted down a wave-guide which is loaded with irises to break the guide into a series of resonant cavities. The size of the cavities is chosen to ensure that the phase velocity of the electromagnetic wave is just right to accelerate the electrons, which obtain energy from the longitudinal component of the electric field.

The neutrons are produced by interactions of the electron beam with a heavy metal target. Initially, the electrons are slowed down rapidly, emitting gamma-rays due to *bremstrahlung*. These gamma-rays then induce photoneutron (and in certain targets photofission) reactions releasing a 'white' spectrum of neutrons. The primary spectrum is in fact a good approximation to a Maxwellian distribution with a temperature of 1 MeV. The spectral shape may be altered by placing some moderating material next to the target. Typically, 2 cm of polythene is used and this increases the flux in the region up to about 10 keV. It also defines the position at which the neutron effectively originated more precisely, improving the neutron energy resolution. Such a moderator was in place for the measurements made in these investigations.

There are currently three separate neutron-producing targets on HELIOS, which are chosen to cater for the differing requirements of particular experiments. For the purpose of these investigations, working at keV neutron energies, the fast neutron target (FNT) was the most suitable, as this can provide sufficient power (~ 5 kW) in a pulse short enough (~ 10 ns) to give the necessary neutron energy resolution. The condensed matter target (CMT) is used primarily for materials studies using low energy neutrons, whereas the booster target is best when used for energies intermediate between the CMT and FNT ranges. Figure 3.2 shows the configuration of the FNT and CMT targets. They are identical except for some differences in the cladding materials.

The low energy cell shown in Figure 3.1 is intended for photonuclear studies, the electron beam being diverted after passing through only two of the eight acceleration sections. This low energy beam is then used to produce gamma-rays by striking a suitable *bremstrahlung* radiator.

A summary of the main characteristics of HELIOS and the use of the different targets has been written by Lynn (Lyn 79).

3.2.2 The Neutron Energy Resolution

At the commencement of this work, the shortest existing flight path on the FNT was one of 42 m in length. Preliminary experiments on this flight path confirmed that, as expected, the count-rates would be too small for any useful measurements to be made, and it was necessary to undertake the design and construction of a new, shorter flight path and associated experimental station (blockhouse).

The most important decision which had to be made concerning the flight path was the proposed length which, as discussed above, had to be a compromise between achieving a higher count-rate with a shorter flight path and losing neutron energy resolution. It was also known that the gamma flash recovery would be slower on a short flight path, although this could be ameliorated in part by suitable shielding. It was considered that, in principle, the flight path should allow data to be accumulated for resonance capture measurements at up to 100 keV incident neutron energy. In the mass region $A \approx 60$, an energy resolution of 1% would enable most resonances to be separated, the mean separation of resonances for this mass region being ~ 5 keV for even-even nuclei. Taking all contributions to the resolution into account, and bearing in mind possible gamma flash effects, 12.5 m appeared to be the shortest acceptable path length.

The various components considered which added to the resolution were:

- machine pulse width
- the target resolution, essentially due to its finite thickness and the effects of moderation by the cooling water
- a geometry term, arising from the path length difference across the sample which exists because the flight path is not perpendicular to the FNT
- the channel width which results from the finite bin size of the timing channels
- the timing jitter of the detector.

The results for the calculated resolution are shown in Table 3.1 where uncertainties in path length have been converted to time uncertainties through the relation

$$\Delta t = \frac{\Delta l}{v} \quad (3.3)$$

where v is the neutron velocity.

Estimates of the target resolution were provided by Syme (Sym 82) and the timing channel width, detector jitter and machine pulse width were taken to give a total additional uncertainty of 16 ns, their contributions being 10 ns, 7.5 ns and 10 ns respectively.

At the time of the study of a proposed flight path, the position denoted F2, at an angle of 15° to the normal of the FNT moderator, was still available. The new flight path of length 12.5 m was therefore situated at this position.

3.2.3 The Collimation of the Flight Path

The collimation of a fast neutron flight path has to be undertaken with a great deal of care (Len 70) in order to produce a well-defined beam which illuminates the

Table 3.1

Neutron energy resolution $\Delta E/E$ as function of energy for a 12.5 m flight path at an angle of 15° to the FNT on HELIOS. Also given are the associated time-of-flight (TOF) and the contributions to the timing uncertainty from the target, Δt_{targ} , and from the flight path geometry, Δt_{geom} . The sample diameter is assumed to be 80 mm with the diameter of the target collimated to 100 mm. Values for Δt_{targ} are taken from (Sym 82). The total timing uncertainty, Δt_{tot} , assumes an additional uncertainty of 16 ns due to the combined effect of pulse width, detector jitter and timing channel width.

E(keV)	TOF(μ s)	Δt_{targ} (ns)	Δt_{geom} (ns)	Δt_{tot} (ns)	$\Delta E/E$ (%)
0.1	90.3	259	140	295	0.65
0.2	63.9	188	99	213	0.67
0.4	45.2	141	70	158	0.70
0.7	34.1	106	53	120	0.70
1.0	28.6	89	44	101	0.71
2.0	20.2	61	31	70	0.69
4.0	14.3	42	22	50	0.70
7.0	10.8	35	17	42	0.78
10.0	9.03	28	14	35	0.78
20.0	6.39	24	9.9	31	0.97
40.0	4.52	16	7.0	24	1.06
70.0	3.41	14	5.3	22	1.3
100.0	2.86	12	4.4	20	1.4

sample reasonably uniformly and minimizes scattering from pipe walls and collimators, since this gives rise to background neutrons. Background in this sense refers to neutrons which, although produced initially by the linac, arrive at the sample with the wrong time-of-flight for their energy. It normally consists of both time-dependent and time-independent components and should be minimised in order to obtain a good picture of capture at a given neutron energy.

The collimation of F2 is shown schematically in Figure 3.3 where the scale along the axis of the flight path has been reduced in order to enhance the important angles in the collimation. Significant lines of sight have also been inserted. Special features connected with the design of the collimation are discussed below.

Each collimator was constructed in three separate sections, made of different materials: iron, borated resin and lead. These various layers were necessary in order to provide adequate shielding from fast as well as thermal neutrons. The iron has a sufficiently high cross-section for fast neutrons (above 3 MeV), due to inelastic scattering, to compensate for the rapidly diminishing effect achieved by hydrogenous materials at these energies. The iron knocks fast neutrons down to energies below 1 MeV where they are effectively moderated by the hydrogen and carbon present in the resin. The boron in the resin has a very large cross-section for capturing the thermalized neutrons, and finally the lead is necessary in order to shield from the gamma-rays produced in the earlier collimators.

The size of the umbra and penumbra of the beam depends on the positioning of the first and last collimators between the neutron-producing target and the sample. The umbra (the part of the sample which is illuminated by the maximum amount of the target, compared to the penumbra in which only some of the target is visible) should be made as large as possible in order to maximize the count-rate and ensure that the illumination is uniform. However, this requires that the final collimator is placed as close as possible to the sample. This is not acceptable since large amounts of beam then scatter into the sample. The compromise reached was to place the final collimator about 1.5 m from the sample.

In order to make the scattered beam seen by the sample as small as possible, it was arranged that the sample could not see the walls of the outer pipe at any position, and also that the target was not allowed to illuminate the pipe wall directly. All this had to be achieved with as little collimation as possible since if there is too much collimation, the beam tends to rattle inside the collimators as if the inner diameter of the collimators is the pipe itself.

Because of the existing positioning of an experimental hall (CB) on the CMT, it was necessary to bring the flight path through the wall of the FNT cell at a different angle to the existing hole, in order to ensure that the sample position was at least 1 m away from the wall of CB. This was achieved by placing a smaller diameter pipe inside, although not concentric with, the existing pipe which penetrated the FNT cell wall. This inner pipe was supported at each end by a flange, and an accurate alignment of the pipe could be achieved by use of a system of adjustable supporting bolts. This arrangement meant that it was also necessary to provide collimation externally to the inner pipe, in order to prevent neutrons escaping directly through the FNT cell wall. It was also required that there was no pathway through the gap between the small pipe and the external collimators, so an additional collimator was placed inside the FNT cell, covering this gap.

3.2.4 Components of the Flight Path

The main features of the flight path are illustrated in Figure 3.4, showing the target, through-wall pipe, fission chamber position, beam blocker, filter position, sample position, blockhouse and dump pipe.

The flight tube was evacuated by a rotary pump in order to maintain a high neutron transmission. Thin windows, made out of melinex, which provided negligible attenuation of the beam, were used at the breaks between pipe sections. These occurred in two places:

- (i) just outside the FNT wall where there was a gap of ~ 1 cm for the mounting of a fission chamber monitor, incorporated to measure the neutron fluence of each run
- (ii) between the pipe section containing the sample and the final section of pipe work where there was a gap of ~ 50 cm to allow insertion of the sample.

The beam blocker consisted of a large mass of iron, sufficient to attenuate the neutron beam by a large amount, placed on runners, which could be driven into place remotely by an electric motor. A system of electrical interlocks ensured that access to the blockhouse was possible only when the iron block was placed in the neutron beam, therefore providing protection against the danger of personnel becoming irradiated by the neutron beam when the machine was still on.

The filter position enabled suitable filters to be placed in the beam as necessary.

One such filter which had to be present for all resonance energy measurements was the boron overlap filter. For these investigations a natural boron filter of thickness 0.36 g cm^{-2} was used. It was produced by sintering a fine boron powder, and overall thickness uniformity was achieved to within about 5%.

All the pipe work was made of either steel or aluminium except for the section in which the sample was placed. This was made of carbon fibre and resin, which scatters neutrons less than an aluminium pipe and has little gamma-ray attenuation. The sample itself was held in place by a lightly constructed carbon fibre framework and the positioning of the sample was achieved by removal of the end window and insertion inside the pipe to a known distance. The diameter of the samples was greater than the beam diameter, estimated from the collimation, by 3 mm in order to provide some lee-way against any possible misalignment of the flight path.

The blockhouse was constructed out of concrete blocks of 60 cm thickness and it was arranged in such a way that no wall was closer than 1 m from the sample position. This was to ensure that the number of neutrons which scattered back into the sample from the blockhouse walls was kept to a minimum. The wall thickness of 60 cm was sufficient to shield from any neutron background which might exist outside from scattering off collimators and from the nearby beam lines of other experiments. The shape of the blockhouse was also determined by the necessity to shield the sample from any direct line to the outside through the door which was made out of wood.

The beam dump was a large block of concrete, $150 \text{ cm} \times 150 \text{ cm}$, with a recessed hole into which the final piece of pipework was inserted. Its principal purpose was to provide radiological protection for personnel without producing a significant amount of scattering back into the sample. For this purpose it was placed some 4 m outside the blockhouse wall.

3.3 Capture Gamma-ray Detection

3.3.1 Detectors and Geometry

Two detectors were incorporated in the experimental set up in order to provide an increased count-rate. They were high purity Ge detectors made from n-type rather than p-type material, since n-type detectors are known to be more resistant to the effects of neutron damage (Peh + 79). This is a result of the collection being dominated by electrons rather than holes in an n-type detector (the main effect of neutron damage is to produce hole trapping centres (Kra + 68)). One of the detectors was provided by Princeton Gamma-Tech (PGT) and was of volume 101 cm^3 , having a relative efficiency of 25%. The FWHM resolution was initially 2.3 keV at 1.33 MeV. The second detector, provided by EG and G Ortec (EGG) had similar characteristics, with 25% relative efficiency and a resolution quoted as 2.0 keV at 1.33 MeV. The resolution achieved with the electronics of the current experiment was not as good as this, due to the extraordinary requirements for gamma flash recovery, described in the next section.

The geometry of the sample-detector arrangement was very important as it has a direct bearing on the count-rate and effects such as the gamma flash and neutron scattering. The importance of increasing the count-rate determined that the detectors should be as close as possible to the sample. In practice a limit was imposed by the need to ensure that the detector was not within the neutron beam, and in any case there was the physical barrier imposed by the pipe within which the

sample was placed. The positioning along the pipe length was determined by the need to minimize the gamma flash, and also the convenience and accuracy of providing a simple geometry for which the attenuation of capture gamma-rays within the sample could readily be calculated. The gamma-rays which come from the gamma flash enter the detector only after having Compton scattered in the sample. As Compton scattering is sharply forward peaked for all but low energy gamma-rays, the detector was placed 'up-stream' of the sample. The chosen geometry is illustrated schematically in Figure 3.5, where it is evident that the correction for gamma-ray attenuation in the sample is quite simple, the range of distances through which the bulk of gamma-rays travel to get out of the sample being small. Figure 3.6 shows the experimental set up and electronics in the F2 blockhouse.

The gamma flash effect was investigated experimentally and found to be large even in the chosen geometry. Two methods were proposed to reduce the effect of the gamma flash; both reduce the count-rate as well. Lead could be placed in the neutron beam (conveniently in the filter position), in which case the neutron flux reaching the sample would be attenuated as well as the gamma-rays from the gamma flash, and it would also add some structure to the energy spectrum of the neutron beam. As an alternative, lead could be placed between the sample and the detectors. This would reduce the gamma flash but it would also attenuate the capture gamma-rays which were to be observed. In practice, a thickness of 1 cm of lead was placed in the filter position and further thicknesses of 2 mm and 5 mm were placed in front of the EGG and PGT detectors respectively. The extra amount in front of the PGT detector was necessary since the recovery from the gamma flash was inferior in this detector, which had a large number of events for which the collection time was rather long, up to 2 or 3 μ s.

3.3.2 The Kandiah Pulse Height Processing System

The gamma-ray energy pulse height was analysed using an electronics system developed by Kandiah of the Instrumentation and Applied Physics Division at Harwell (KW 81). This system consists of a pre-amplifier, pulse processor and ADC which, however, can be better thought of as one complete unit since they cannot be operated independently of one another. It has many advanced features, employing in its original form opto-electronic feedback, a fixed processing and restore period, allowing comprehensive pile-up protection, gain stabilisation and zero stabilisation. The FET in the pre-amplifier and the various time constants in the processor are each matched individually to the detector and the user's requirements.

When an event has been processed, a digital word is produced by the ADC, proportional to the gamma-ray energy, which is held whilst a restore sequence is initiated. The restore sequence discharges the pre-amplifier, and resets the various variable time constants ready for the next event. The pulse height word from the ADC is placed on a data bus, awaiting transfer to a suitable storage device such as a computer by means of a 'handshake'. The handshake consists of the ADC setting a flag (a look-at-me or LAM) which indicates to the storage device that the data is ready and transfer should begin. When the transfer has been completed, the storage device sets a data-received flag, the ADC data lines are reset to zeros and the pulse processor is ready to accept another event.

There are three ways in which an event may be rejected before the fixed processing period is completed. In the normal mode of operation this occurs

whenever there is pile-up. In addition, when operating in coincidence mode, termination of the processing occurs if a coincidence pulse is not received within the fixed processing period, or if an anti-coincidence pulse is received. In each of these cases, the ADC does not convert the analogue signal, so zeros remain on the data bus, and a restore period is initiated immediately.

For these investigations, the opto-electronic feedback was replaced by a more powerful feedback loop able to provide a larger current to cope with the exceptional demands imposed by the need to recover from the gamma flash within $\sim 2.5 \mu\text{s}$. This unfortunately resulted in an increase in electronic noise such that the FWHM resolution at 1.33 MeV was increased to 4.5 keV for each detector. However, for the high energy transitions which were primarily being observed, the major component of the resolution arises from the counting statistics associated with the collection of the particle-hole pairs in the detector, and the increased electronics noise was therefore not important.

3.3.3 The Timing System

The pre-amplifier in the Kandiah system provides two analogue outputs; one was used to derive the pulse height signal through the pulse processor and ADC, whilst the other was used to derive the timing information of an event.

The first stage in producing the timing word was to shape the pre-amplifier output using an Ortec 474 timing filter amplifier. This shaped pulse was then fed into a Nuclear Enterprises ARC timing analyser NE4676, which uses the amplitude and rise time compensated (ARC) technique to produce a timing signal with characteristics of low jitter and walk. In principle, the ARC method gives no walk for pulses having different rise times and amplitudes, provided that the slope of the pulse is constant. This should be compared to the constant fraction technique which only provides compensation for events having amplitude variations. The additional independence from the rise time is provided by taking the constant fraction before the pulse has reached its peak. The ARC method has been compared to other methods (CC 71) and in general is found to be superior, particularly for large detectors where the position within the detector at which the event is detected may make a large difference to the signal produced by the pre-amplifier.

The PGT detector used in these investigations was particularly prone to variations in the rise time of the pre-amplifier output, producing some pulses with rise times of a few μs . The timing jitter from such slow signals cannot be in the region required (a few ns), and so use was made of the slow rise time rejection circuit which was available on the timing analyser. This circuit rejects all events which take longer than a given time to cross a low-level threshold. The observed jitter was therefore reduced, but there was an associated unavoidable loss of events.

The measurement and optimisation of the timing resolution of the two detectors is described in Chapter 5.

In order to produce a digital word for the time of the event, the output from the timing analyser was used as the stop signal for a TAC, the start signal for the TAC having been derived from the machine pulse using a toroid placed after the first section of the accelerator. The timing jitter from this start pulse was believed to be negligible compared with the width of the machine pulse. Finally, the pulse height from the TAC, which was proportional to the time-of-flight of the event, was used to produce a digital word with an ADC. The use of a single TAC was possible since,

as is described below, the data collection worked in a single-shot mode, i.e. only one event per machine pulse was ever recorded.

3.4 The Electronics and Computer Interface

3.4.1 Introduction

The pulse height processing system and the timing system described above was duplicated for the two detectors, and it was necessary to develop some electronics which would allow the two outputs to be interfaced separately to the data acquisition computer. This was simplified by the adoption of a single-shot approach so that only one detector at a time had to be dealt with whilst the other was effectively gated out. The use of the single-shot technique caused very little loss in counts, since the count-rate was so low that the chance of observing more than one event during the live time of each machine pulse was typically only 5%. In addition, with a single-shot approach, corrections for dead time were simple and accurate.

A block diagram of the complete electronics system is given in Figure 3.7. The pulse height and timing systems for each detector were situated in the blockhouse, together with the specially developed electronic unit DECODER (Device for the Electronic Combination Of Detectors and Event Recognition), described below, which combined the output from the two detectors and ensured that timing and pulse height signals were processed from one detector at a time. The other electronic unit in the blockhouse was the link transmitter. This is a parallel to serial converter, described by Morris (Mor 83), which allows a 12-bit word to be transmitted down a single coaxial cable.

The rest of the data collection system was situated in the counting laboratory some 50 m away, where the data acquisition computer with its direct memory access (DMA) and CAMAC interfaces was positioned. Here the stop pulse for the event was input to the TAC, and the serial form of the pulse height word was changed back to a parallel form before being input to the computer by the DMA. The CAMAC interface enabled scalers, recording various experimental run parameters, to be under computer control. In each run, scalers were set up to record the number of machine pulses, the number of events, the length of the run, and the number of counts in various neutron output monitors.

The various components of the data collection system are now described in more detail.

3.4.2 Combining the Two Detectors

Besides ensuring that each detector operated separately, so that individual pulse height spectra could be built up, it was also fundamentally important that the timing word and pulse height word were both derived from the same event. This was achieved by the unit DECODER, the circuit diagram of which is given in Figure 3.8.

There were five separate tasks which DECODER performed:

- (i) it took the timing outputs from each detector and sent a single stop signal to the TAC
- (ii) it ensured that one detector at a time produced a pulse height word to be transmitted down the serial link
- (iii) it set an extra bit on the pulse height word, determining in which detector the event was observed

- (iv) it ensured that only a single event per machine burst was processed
- (v) it ensured processing took place only for events occurring in a given time interval.

To achieve the first task, the stop pulses from each of the two timing analysers were fed into a simple passive 'or' gate, made from diodes and resistors, and the output was sent up a coaxial cable to the TAC.

The second task was achieved by taking the outputs of the pulse height words from the ADCs of the two detectors and combining the corresponding bits of each word in integrated circuit 'or' gates. Provided only the detector in which the event had occurred had any 1s on its ADC output lines, then the output from the 'or' gates represented the pulse height of the required event. To ensure that the other pulse processor did not produce any 1s on its output lines, both the systems were operated in coincidence mode and a coincidence pulse was provided by the appropriate detector's own timing output. It was therefore impossible to produce a pulse height word without first producing a timing signal for the event.

The other functions of the unit may be described most clearly by following through the sequence of events from a typical machine cycle in which a gamma-ray is observed in one of the detectors. The timing diagram of Figure 3.9 indicates the order of events.

A pre-pulse is emitted by the master timing unit (MTU), which is responsible for triggering the machine, about $30 \mu\text{s}$ before the gun fires. This pulse is not accurate enough for use as a start pulse, as it has about 20 ns jitter relative to the electron gun firing, but it is perfectly adequate for inhibiting the pulse processors during the gamma flash and enabling and disabling the processing for a given time interval, using standard timing delay gates developed within the Harwell linac group (Mor 83), which lock into the clock pulse stream of the MTU. A given time after the pre-pulse, an inhibit signal is sent to each pulse processor. This holds the system in restore mode, ensuring that the charge deposited by the detectors at the time of the gamma flash is dissipated as rapidly as possible. After a time of $\sim 2.5 \mu\text{s}$, when it is believed that the detectors have recovered from the gamma flash, an enable pulse is supplied to DECODER. This sets a bistable within the unit which ungates the output from the timing analysers. Up until that point, the output from the timing analysers is gated out so that the gamma flash signal is not recorded each machine cycle. When the first valid event occurs in a detector, the appropriate timing analyser produces a stop pulse. Independent of which detector observed the event, the stop pulse then initiates the following operations:

- it disables both the timing analysers by resetting the bistable which gates them both out
- it sends a stop to the TAC so that the timing word for the event is produced
- it sends a pulse to the coincidence input of the processor for the detector which has observed the event
- it sends a signal to the link transmitter, commanding it to transmit the pulse height data on the output lines of DECODER after a set period of $30 \mu\text{s}$, which is long enough to ensure that the pulse processor ADC has produced a pulse height word.

In addition:

- a stop from the EGG detector (detector A) sets the most significant bit of the pulse height word to a 1 so that the top half of the pulse height spectrum corresponds to events in detector A and the bottom half to events in detector B (the PGT detector)
- a stop from the PGT detector sends an anti-coincidence pulse to the EGG detector pulse processor.

The pulse processor produces an output word from the ADC after about $10 \mu\text{s}$ and this is placed on the output data lines of DECODER through the 'or' gates described above. When the transmit signal appears afterwards, the link transmitter turns the 1s and 0s of the pulse height word into a series of long and short pulses respectively. As soon as the last bit has been transmitted up the link, a data-received signal is returned to the pulse processor. This resets the ADC data lines to zero awaiting the next machine cycle.

The above is an example of a machine cycle in which an event is observed in a single detector, giving rise to both pulse height and timing signals. However, the system was also designed to cope with other possible sequences of events which may have occurred.

If no event was detected in the time period of interest, a disable pulse (derived from the MTU) was used to inhibit any further stop pulses in just the same way as if an event had occurred. This ensured that the electronics was restored to its prepared state well in advance of the next machine pulse.

It was possible for events to occur simultaneously in both detectors, in which case both the pulse processors would be coincided. This was the purpose of the PGT detector sending an anti-coincidence pulse to the EGG detector's pulse processor. It ensured rejection of any event in the EGG detector once the PGT had accepted an event for processing.

The Kandiah system produces a non-standard output from the pre-amplifier: a square pulse of length equal to the processing time and of height proportional to the gamma-ray energy. Because of this shape rather than the more normal shape with a long tail, the timing filter amplifier produced a sizeable output, not only when the event was detected, but also on the back edge of the pre-amplifier pulse, i.e. at a time of one processing period after the detection of the event. Therefore, if an event occurred before the system was enabled, but so close in time that by the end of the processing period the system was live, then the back edge of the pulse would provide an anomalous stop signal. To avoid this, the signal which the pulse processor issues to restore the pre-amplifier was used to veto the stop pulse from the timing analysers, ensuring that a stop pulse could only be produced at the beginning of a processing period.

There were also occasions when, for some reason, processing of an event was terminated by the Kandiah system before the ADC produced a word. This occurred for instance when a pile-up event was detected by the processor or when the stop pulse occurred before the processor had fully recovered from the gamma flash. In each case the result was the same; namely that because the stop pulse had initiated all the actions indicated previously, an event was recorded, but the pulse height associated with the event was zero. This feature provided a useful check on the frequency of such events.

3.4.3 The Data Acquisition

Attention is now turned to that part of the electronics which was situated in the counting laboratory. The pulse height word was received in serial form via a coaxial cable from the blockhouse, whilst the stop pulse was received along a separate cable. Also routed to the counting laboratory were signals from the fission chamber monitor, the machine start pulse, the MTU signals and the neutron output monitors situated in the roof of the FNT cell.

The serial form of the pulse height word was converted back to its digital form and provided the least significant 12 bits of a 21 bit event word. The lowest 11 bits were the pulse height, digitised to 2048 channels resolution, and the 12th bit was the flag denoting in which detector the event had been observed. The most significant 9 bits of the event word were provided by the timing signal from the TAC, digitised to 512 channels resolution. The limit of 21 bits of information which were recorded for each event was imposed by the data acquisition computer and its associated software.

The interface of the two words to the computer was through the standard two parameter time-of-flight scaler units which are used at HELIOS (Mor 83), except for a modification to allow the time-of-flight word to be provided by an external ADC, rather than the internal time digitiser. The use of a TAC and ADC, rather than the more conventional approach of a time digitiser, was favoured here due to its flexibility in providing any required timing channel width down to a very small value. The disadvantage of an analogue system is its vulnerability to drift. Most time-of-flight experiments use many more than the present 512 timing channels, and the stability of a TAC in such cases would not be sufficient.

When both words of information were ready for transfer to the computer, a flag was set and the data was read via direct memory access into a buffer on the PDP-11/45. The data-received signal was then returned to the timing ADC and the temporary buffers holding the time and pulse height word in the interface were set to zero.

The handling of a two parameter experiment by the PDP-11/45 has been described previously (Cha + 77). Briefly, it consists of a series of buffer levels which may be filled to cope with peaks in the count rate. The data is sorted preliminarily in these buffers so that, when full, the writing to disc may take place rapidly. A 2 byte per channel incremental histogram is firstly built up on the disc and if any channel reaches its overflow value, i.e. 2^{16} , data collection is suspended whilst the cumulative file, with 4 bytes per channel, is up-dated. Once this is completed, data collection resumes. The cumulative file is also up-dated before producing graphs of one parameter spectrum when summed over specified channels of the other parameter, or when the run is ended.

When a run was completed, the up-dated cumulative histogram file was read out to a magnetic tape, together with the contents of the CAMAC scalers and other details of the run. The tapes were archived on the mainframe computer at Harwell for subsequent off-line analysis.

3.5 Neutron Fluence Measurements

To obtain an absolute value of partial radiative widths, it is necessary to know the number of capture gamma-rays produced for a given number of neutrons incident on the sample under study. The number of neutrons which strike a sample in a given run, known as the fluence ($= \text{flux} \times \text{time}$), in a given energy range, may be deduced from a comparison of the gamma-ray output from the run with that from a separate run in which a sample of known standard (n, γ) cross-section is inserted in the same sample position, provided also that the total neutron output is known for each of the runs.

A much-used standard, applicable in the present investigations, for neutron energies below 100 keV is ^{10}B , since this provides a 478 keV gamma-ray from the $^{10}\text{B}(n, \alpha)^7\text{Li}$ reaction in 93.6% of all such absorptions. The cross-section for the reaction has been evaluated (Wat 83), and its behaviour is nearly $1/v$.

Observations were therefore made with a thin sample (7×10^{-3} atoms b^{-1}) of boron, highly enriched in ^{10}B , which was placed in the sample position on the F2 flight path, whilst the standard set up for gamma-ray detection remained unaltered from the normal capture runs. The time-of-flight spectrum for the 478 keV gamma-ray then provided a measurement of the neutron flux whilst the constancy of the set up and detectors ensured that systematic errors in this flux determination were minimized.

The normalisation of total neutron outputs for the different runs was achieved by comparing counts recorded in the in-beam fission chamber monitor placed outside the FNT cell wall. The chamber was a disc, 15 cm in diameter and 1 cm thick, filled with an inert atmosphere of argon and methane, having a central foil coated with fissile material and thin windows of beryllium through which the beam passed. The central foil was platinum, of thickness 0.254 mm, and was coated with 2.047 mg cm^{-2} of ^{235}U , providing an active area of 126 cm^2 with which the neutrons could interact. The ionisation caused by the fission fragments was collected by the electric field, established by applying a voltage between the platinum foil and the windows, and the pulse so produced was sent to a pre-amplifier. The signal from the pre-amplifier was shaped in a main amplifier and this signal was then sent to a discriminator. The level of the discriminator was set to eliminate background pulses, present due to the alpha decay of the uranium. Scalers recorded the number of events occurring in the chamber within two different timing bins, one corresponding to neutrons in the keV energy region and one covering a much lower energy region. Consistency between these two monitor values was an indication that the flux shape was not varying.

To ensure that the flux shape was constant over the period of an experimental run, the ^{10}B flux measurement could be carried out at the beginning of each run and then repeated at the end. If necessary, the average of these measurements could then be taken.

4 METHODS OF ANALYSIS

4.1 Introduction

This chapter presents the methods which were used to analyse the two parameter data, collected as described in Chapter 3. In addition, some of the techniques which were used for analysing the preliminary measurements (see Chapter 5) are given. An important feature of all the analysis is the part played by the strong correlations which exist between many of the observed variables. A rigorous estimation of errors in such circumstances requires careful consideration of the part played by the covariance terms. The manner in which these terms were incorporated into the analysis is described below in principle, whilst the mathematical detail may be found in Appendix C.

4.1.1 Analysis of Two Parameter Data

A typical portion of the two parameter data for a neutron capture gamma-ray spectrum is illustrated schematically in Figure 4.1, where the axes represent the number of events observed against the neutron time-of-flight and the gamma-ray energy. The gamma-ray channel shows two peaks (resonances) in the time-of-flight spectrum, whilst the time-of-flight channel shows three gamma-ray lines. The peaks in this two parameter space correspond to particular gamma-ray lines in neutron resonances, and the fundamental requirement of the analysis is to evaluate the strength of particular transitions in resonances, i.e to evaluate the volume under each of the peaks. The hatched area on Figure 4.1 illustrates the area over which the integration of the volume would take place for a particular resonance and gamma-ray line. To obtain the net volume under a peak, it is necessary to subtract the underlying background volume, which is non-zero since the response of a Ge detector does not go to zero for channels away from a gamma-ray line.

There are two equivalent approaches to extracting the volume integral; either the time-of-flight spectrum for the gamma-ray line may be produced and then the area over the resonance region extracted, or else the gamma-ray spectrum for the resonance may be obtained and the peak area of the gamma-ray calculated. The choice of which approach to adopt is determined by experimental effects, such as the multiple scattering of the neutrons in the sample, as well as by the greater convenience in the data handling provided by a particular method in the situation being considered.

4.1.2 Peak Extraction Techniques

The response function of a Ge detector is complicated by the variety of processes which can give rise to an output pulse. Gamma-rays interact in three ways within the detector: Compton scattering, photo-electric effects and (for sufficiently high energy gamma-rays) pair production. The result is that a high energy, monoenergetic gamma-ray source gives rise to three distinct peaks, the full energy, single escape and double escape peaks, plus a continuum background due to Compton processes. Figure 4.2 illustrates the high energy region of the spectrum obtained when the EGG detector used in these investigations was exposed to monoenergetic gamma-rays, produced from a source using the $^{13}\text{C}(\alpha,n)^{16}\text{O}$ reaction (Mas 85).

When many different energy gamma-rays are present, as in the neutron capture

case, the overall effect is to produce the required gamma-ray peaks on an unknown, but smoothly varying background. The problem then faced is to determine the area of such a peak.

For the highest resolution work, a great deal of effort has been expended in deriving parameterisations of the peak shapes produced by Ge detectors, in order to allow the fitting of suitable curves and the deduction of peak areas (see e.g. (Cif 82)). However, such methods are best suited to low energy gamma-ray peaks collected with good counting statistics, and such conditions do not apply here. Instead a very much simpler approach was adopted, requiring no fitting of peaks, in which it was assumed that the background under a gamma-ray peak was well represented by a straight line.

The gamma-ray spectra, produced by summing over suitable time-of-flight channels, were examined by eye, and upper and lower limits, defining peak and background regions were fixed (see Figure 4.3). A straight line, determined by the least squares method (see Appendix C), was fitted through the points of the two background regions, and then the area was evaluated as the integral in the peak window minus the assumed straight line background. The same method was applied in determining the gamma-ray spectrum for a particular resonance. In this case, windows were set for resonance and background regions by observing the time-of-flight spectrum summed over all gamma-ray channels corresponding to events with energies > 2.5 MeV. This showed up the resonances more clearly, as much of the contribution from background gamma-rays, which consisted mostly of low energy lines, was being omitted.

Any inaccuracy in the straight line background assumption was ameliorated in part by the fact that the same method for evaluating peak areas was applied when measuring the efficiency of the detectors. Any systematic errors associated with the method should be common to all determinations, so it was assumed that, to an extent, they would tend to cancel out.

For gamma-ray lines where the signal-to-background ratio was large, this straight line background assumption proved reliable, as indicated by the net volume under a peak being the same, independent of the order of integration. However, for smaller lines the method was not so successful. This may be understood since in these cases the gamma-ray spectrum in each time-of-flight channel has very few counts in it (the resonances were spread over more time-of-flight channels than were the gamma-ray lines), and so the statistics for extracting gamma-ray peak areas from each time-of-flight channel were poor. In these cases, it was better therefore firstly to obtain the gamma-ray spectrum from the time-of-flight region of interest, and then to use a more advanced technique to evaluate the net peak area under the gamma-ray lines, which took into account the long-range smoothness of the underlying background.

4.1.3 Experimental Complexities

Up until now, only the ideal situation has been considered in which the strength of the transition (i.e. the partial radiative width) is taken to be proportional to the net area under the gamma-ray peak in a particular resonance. There are however several experimental complexities which can introduce differences from this ideal behaviour. When investigating radiative capture in an s -wave resonance, the following effects may be observed

- capture following multiple scattering of the neutrons within the sample

- off-resonance potential scattering followed by capture in the sample
- capture in p -wave resonances following s -wave resonance scattering
- capture in the Ge detector from neutrons scattered by the sample

The most apparent of these effects is the multiple scattering within the sample. When a resonance energy neutron strikes the sample it may be captured immediately, producing a gamma-ray, but it is also possible, and in some cases most probable, that the neutron will be resonantly scattered. If the neutron does not lose too much energy in this scattering event (from kinematic considerations, the maximum fraction of its energy which a neutron may lose is $4/A$, A being the mass number of the target nucleus), and the resonance is broad, it may then undergo further interactions within the sample before eventually being captured. The timing of such events does not correspond to the energy of the captured neutron, but rather to that of the neutron before any interaction occurred, and the result is a change in the shape of the time-of-flight spectrum.

It is also possible for off-resonance energy neutrons to undergo potential scattering in which they lose enough energy to bring them to a resonance energy where the interaction probability is large, and once more the shape of the time-of-flight spectrum may be altered.

In some circumstances, a p -wave neutron resonance may lie close to, or within a broad s -wave resonance which is to be investigated. Neutrons scattered in the broad resonance may be captured in the p -wave state which, although narrow can often have a capture area comparable to that of the s -wave resonance. As the gamma-ray spectrum for capture in the p -wave state will in general differ from that for the s -wave, the presence of the p -wave resonance may not only increase the strength of a line, but also affect the shape of the measured spectrum. Regions of time-of-flight in which a scattered neutron can be captured in a p -wave resonance have therefore to be excluded before deducing the required gamma-ray spectrum.

All the processes above necessarily give rise to more gamma-ray events than would be expected in the absence of scattering, the precise enhancement being a complicated function of the neutron cross-sections and the sample geometry. This may however be calculated with a suitable computer code as discussed below, which can predict the shape of the resonance for comparison with the experimental data.

The final effect is that caused by the scattering of neutrons from the sample into the surroundings, giving rise to capture gamma-ray lines from materials in the immediate environment. By far the largest number of such capture events come from within the Ge crystals of which the detectors are made, since the gamma-rays then have a large probability of being observed. Although there are many such events, the effect is not of great importance, as the energies of the gamma-ray lines so produced correspond to transitions in the Ge isotopes, and these are not of the same energy as the gamma-ray transitions under study. In general therefore, the effect is to add a smooth contribution to the underlying background below the gamma-ray peaks of interest. It is possible that the Ge lines will overlap with those under study, but any such occurrence should be clear from observations of the time-of-flight of the particular lines since, if they arose from capture in Ge, they should be enhanced at the position of the Ge resonances and not at the position of the resonances of the sample under investigation.

4.2 Expressions for the Partial Radiative Width

Expressions will now be derived which allow the partial radiative widths to be deduced from the experimentally determined peak areas.

The peak area $A(E_{\gamma\mu}, E_n)$ for a gamma-ray transition of energy $E_{\gamma\mu}$, to a final state μ in a run with fluence F_s of neutrons with energy E_n is given by

$$A(E_{\gamma\mu}, E_n) = \varepsilon(E_{\gamma\mu})T(E_{\gamma\mu})\Omega Y_s(E_{\gamma\mu}, E_n)F_s \quad (4.1)$$

where $\varepsilon(E_{\gamma\mu})$ is the detection efficiency for the gamma-ray, $T(E_{\gamma\mu})$ is the transmission of the capture gamma-ray through the various materials between the sample and the detector, Ω is the solid angle which the detector subtends with the sample, and $Y_s(E_{\gamma\mu}, E_n)$ is the yield from the sample. The yield is defined as the number of gamma-rays of energy $E_{\gamma\mu}$ produced for each neutron of energy E_n incident on the sample. Neglecting any possible resonance-resonance interference terms, for neutrons undergoing capture in a resonance λ , the yield is proportional to the partial radiative width of the transition, $\Gamma_{\gamma\lambda\mu}$. The constant of proportionality may be evaluated with the aid of a computer code such as REFIT (Mox 85), which calculates the cross-sections of the constituent isotopes of the sample and evaluates the capture, taking into account such effects as the multiple scattering in the sample. The partial radiative width may therefore be expressed as

$$\Gamma_{\gamma\lambda\mu} = \frac{A(E_{\gamma\mu}, E_n)}{\varepsilon(E_{\gamma\mu})T(E_{\gamma\mu})k_s(E_n)\Omega F_s} \quad (4.2)$$

where the constant of proportionality $k_s(E_n)$ is calculable.

From this expression however it is clear that the relative partial radiative widths may be evaluated without the need to evaluate $k_s(E_n)$, Ω or F_s . If the relative strength of a line is defined as

$$R(E_{\gamma\mu}, E_n) = \frac{A(E_{\gamma\mu}, E_n)}{\varepsilon(E_{\gamma\mu})T(E_{\gamma\mu})}, \quad (4.3)$$

then the partial width for the transition to another final state, μ' may be deduced from the equation

$$\Gamma_{\gamma\lambda\mu'} = \frac{R(E_{\gamma\mu'}, E_n)}{R(E_{\gamma\mu}, E_n)} \Gamma_{\gamma\lambda\mu}. \quad (4.4)$$

Over energies E_n corresponding to a single resonance, the ratio between the partial widths, determined according to eqn. (4.4), should be constant. Therefore, the method of area analysis can be adopted, in which the areas used in eqn. (4.3) are integrals over all neutron energies (i.e. all time-of-flight channels) corresponding to the resonance λ . Application of this method to the present analysis is discussed in section 4.5.

To evaluate all the partial radiative widths, when their relative values have been determined from the area analysis above, only one absolute measurement need be established. This is achieved by relating the yield for one of the transitions to the yield from a run in which the standard ^{10}B is replaced for the sample under study. The area under the 478 keV gamma-ray obtained when a ^{10}B sample is exposed to neutrons of energy E_n is given by

$$A_{10}(E_n) = \varepsilon_{10} T_{10} \Omega F_{10} Y_{10}(E_n) \quad (4.5)$$

where the subscript denotes that the quantities are those defined above but for the

^{10}B gamma-ray. The fluences obtained in the sample run and boron run are proportional to the counts obtained from the fission chamber monitor in the corresponding runs, M_s and M_{10} respectively, and the geometry (and therefore Ω) is the same for each run, so

$$\Gamma_{\gamma\lambda\mu} = \frac{A(E_{\gamma\mu}, E_n)}{A_{10}(E_n)} \frac{\varepsilon_{10}}{\varepsilon(E_{\gamma\mu})} \frac{T_{10}}{T(E_{\gamma\mu})} \frac{M_{10}}{M_s} \frac{Y_{10}(E_n)}{k_s(E_n)}. \quad (4.6)$$

The value for the yield from the boron sample is given by

$$Y_{10}(E) = (1 - e^{-\sigma_T(E)n}) \frac{\sigma_{n\alpha\gamma}(E)}{\sigma_T(E)} \quad (4.7)$$

where $\sigma_T(E)$ and $\sigma_{n\alpha\gamma}(E)$ are, respectively, the total cross-section and the cross-section for the production of the 478 keV gamma-ray from ^{10}B for neutrons of energy E , and n is the thickness of the sample in atoms b^{-1} . The value adopted for the absorption cross-section (in barns) for ^{10}B was $610/\sqrt{E}(\text{eV})$ and the scattering cross-section was taken to be constant at 2.23 b (AM 70). It was assumed that 93.6% of absorptions gave the 478 keV gamma-ray (MG 68).

This expression for the ^{10}B gamma-ray yield gives only the primary yield, i.e. those contributions from absorptions after scattering are ignored. For the sample used in these measurements, and in the energy range considered, this approximation gives no more than a 2% error, which is less than that ($\sim 4\%$) due to using the approximate form for the ^{10}B cross-section given above.

An examination of eqn. (4.6) reveals that for a particular gamma-ray transition, and for neutrons of energy E_n ,

$$\frac{A(E_{\gamma\mu}, E_n)}{A_{10}(E_n)} \propto \frac{k_s(E_n)}{Y_{10}(E_n)} \quad (4.8)$$

which implies that the measured ratio of the areas for the sample run and the fluence-measuring boron run varies for different neutron energies, even within the same resonance (unlike the corresponding areas for different gamma-ray transitions). This means that there is more information available than is used if the areas are simply integrated over all neutron energies covering the energy range of the resonance (i.e. area analysis). Instead, the areas can be evaluated for each time-of-flight channel in turn, and fitted to the theoretical yield point-by-point. This procedure, called shape analysis, is described in section 4.6.

From eqns. (4.3) and (4.6), it is clear that in order to obtain the partial widths, it is necessary to calculate peak areas, the relative efficiency for detecting different energy gamma-rays, and the transmission of gamma-rays through various materials. These calculations are discussed below.

4.3 Gamma-ray Transmission Calculations

Any capture gamma-rays produced within the sample exposed to the neutron beam are attenuated as they travel through a variety of materials before entering the detector. The transmission of the gamma-rays through these materials must be calculated in order to evaluate the expressions given in section 4.2 for the partial radiative widths.

Figure 3.5 showed the sample-detector geometry in which the data were collected. If a gamma-ray event of energy E_γ occurs at a distance d into the sample,

which has a gamma-ray attenuation coefficient of $\mu_s(E_\gamma)$ per unit length, and travels at an angle θ to the perpendicular of the sample, then it is clear that the fraction of such gamma-rays transmitted through the sample, $T_s(E_\gamma)$, is

$$T_s(E_\gamma) = \exp\left(\frac{-d\mu_s(E_\gamma)}{\cos \theta}\right). \quad (4.9)$$

The assumption was made that gamma-ray events occurred uniformly throughout the sample, as the capture probability was low. The value adopted for d was therefore half the thickness of the sample, since this would be the average distance into the sample at which the gamma-rays were produced, and the attenuation was almost proportional to d for the small thicknesses of material involved. The angle θ was chosen to be that subtended by a line from the centre of the sample to the centre of the detector, which again was assumed to represent the average behaviour. Values for the attenuation coefficients were taken from the evaluation of Hubbell (Hub 82) with interpolated values produced by fitting orthogonal polynomials to the data (see Appendix C).

The effect of any inaccuracies involved in assuming the average behaviours for d and θ was investigated by allowing their values to vary as an uncertainty, i.e. calculating the difference in transmission produced by errors in d , θ and $\mu_s(E_\gamma)$ of Δd , $\Delta\theta$ and $\Delta\mu_s(E_\gamma)$ respectively. The implied overall error on the calculated transmission for a particular energy gamma-ray was calculated using the methods of error propagation described in Appendix C. The variables d , θ and μ_s are uncorrelated, but as the assumed errors in d and θ are the same for all gamma-ray energies, the errors in the calculated transmissions at different energies are correlated. It can be shown that the covariance between the transmission calculated for two gamma-rays of energies $E_{\gamma i}$ and $E_{\gamma j}$ is in fact given by

$$\frac{\text{cov}[T_s(E_{\gamma i}), T_s(E_{\gamma j})]}{T_s(E_{\gamma i})T_s(E_{\gamma j})\mu_s(E_{\gamma i})\mu_s(E_{\gamma j})d^2} = \left[\frac{\Delta d}{d}\right]^2 + \tan^2 \theta \left[\frac{\Delta \theta}{\theta}\right]^2 + \frac{\text{cov}[\mu_s(E_{\gamma i}), \mu_s(E_{\gamma j})]}{\mu_s(E_{\gamma i})\mu_s(E_{\gamma j})}. \quad (4.10)$$

Using the calculated uncertainties for the attenuation coefficients provided from the fitting procedure, and giving generous allowances for the errors on d and θ , the predicted error on the transmission was still small, and therefore the approximation of average behaviour could be assumed to be valid without affecting the overall assessment of the gamma-ray transition strengths.

Attenuation of the gamma-rays occurred not only within the sample itself, but also in the canning of the sample, in the pipe walls and in the lead shielding. These contributions were calculated from the known geometry of the experiment, and the total transmission was given by the product of the individual factors. Covariances between these different components (through the common angle θ) were found to be negligible when propagating the error on the total transmission of the capture gamma-rays.

4.4 The Detector Efficiency Determination

The gamma-ray detection efficiency of a Ge detector is a complicated function of the cross-sections for the various gamma-ray interactions which give rise to particle-hole pairs, the collection efficiency for these pairs, the size and quality of the sensitive volume of the detector, the source-detector geometry, the various materials encasing the detector, and the response of the electronic processing system. The net effect is to produce a smooth dependence with gamma-ray energy, and so it is convenient to attempt to fit a suitable smooth analytic function, dependent on not too many parameters. This was the procedure adopted in this study, in which the full energy peak efficiency at gamma-ray energy E_γ , $\varepsilon_{FE}(E_\gamma)$, was assumed to be well represented by the function

$$\ln \varepsilon_{FE}(E_\gamma) = \sum_{i=1}^m p_i \phi_i(\ln E_\gamma) \quad (4.11)$$

where the ϕ_i are orthogonal polynomials and the p_i are m parameters which may be varied in order to provide the best fit to experimental measurements of the efficiency at different gamma-ray energies (see Chapter 5). The linear least squares fitting of orthogonal polynomials to data for which correlations exist, applicable here, is described in Appendix C. The best fit so produced then allowed the efficiency to be predicted for any gamma-ray energy, together with an estimate of the associated error, and of the covariance between estimates for different gamma-ray energies.

It was only necessary to evaluate a relative efficiency curve for each detector, and experimental data for this purpose were provided from standard gamma-ray source measurements, and by observation of the gamma-ray spectra following thermal neutron capture in a variety of materials. In each case, the relative strengths of the gamma-ray lines present were known from published data, so a comparison with observation allowed a series of relative efficiency curves to be deduced, one for each source or capture gamma-ray spectrum. Each of these curves was normalised by eye to obtain a reasonably consistent set of data, but as this normalisation, applied to all measurements from the same source, was to an extent uncertain, correlations resulted between some of the data. The gamma-rays were also attenuated in passing through materials before entering the detector, just as in the case of the capture spectra discussed above, and this also lead to correlations between the estimates of the efficiencies at different energies. The covariance terms were evaluated and used when obtaining the best fit. The need to take the covariances into account in such circumstances has been discussed by Debertin (Deb 85).

The above procedure was applied to the full energy peak efficiency curve, but it was also necessary to deduce the single and double escape peak efficiencies. These were determined by fitting a smooth function to the ratio of the full energy peak area $A_{FE}(E_{\gamma i})$ to the single escape peak area $A_{SE}(E_{\gamma i})$, for lines of the same energy, $E_{\gamma i}$. Similarly, the ratio of the efficiency of the single escape peak to the double escape peak (which is constant for different gamma-ray energies) could be determined by noting the ratio of the single escape peak area to the double escape peak area $A_{DE}(E_{\gamma i})$. The expressions for the efficiencies (quantities denoted by subscripts *SE* and *DE* refer to the single escape peak and double escape peak respectively) are then

$$\varepsilon_{SE}(E_{\gamma i}) = \varepsilon_{FE}(E_{\gamma i}) R_{SF}(E_{\gamma i}) \quad (4.12)$$

and

$$\varepsilon_{DE}(E_{\gamma i}) = R_{DS}\varepsilon_{SE}(E_{\gamma i}) \quad (4.13)$$

where $R_{SF}(E_{\gamma i})$ is provided by a polynomial fit to experimentally observed area ratios for lines of energy $E_{\gamma j}$,

$$R_{SF}(E_{\gamma j}) = \frac{A_{SE}(E_{\gamma j})}{A_{FE}(E_{\gamma j})}, \quad (4.14)$$

and where the constant R_{DS} was evaluated from the experimental measurements of

$$R_{DS}(E_{\gamma j}) = \frac{A_{DE}(E_{\gamma j})}{A_{SE}(E_{\gamma j})}. \quad (4.15)$$

The covariances between estimates of efficiency from the different peaks, implied by the above relations, were determined and included in calculations of the relative transition strengths.

4.5 Area Analysis of Gamma-ray Transitions

4.5.1 The Gamma-ray Spectrum

Attention is now turned to the problem of extracting the gamma-ray line peak areas in a resonance, for the purpose of deducing the relative partial radiative widths of the primary transitions through eqn. (4.3). The first stage is to produce the gamma-ray spectrum for the resonance under consideration. To do this the method of section 4.1.2 was used, where firstly the windows for resonance and off-resonance regions were established by observing the time-of-flight spectrum for all gamma-ray energies > 2.5 MeV in order to show up the resonances clearly. An example of such a time-of-flight spectrum, for capture in ^{54}Fe , is shown in Figure 4.4.

Any number of foreground (resonance) and background (off-resonance) regions could be set, so that if a p -wave resonance occurred within a broad s -wave resonance, the time-of-flight segment corresponding to the p -wave capture could be omitted. The gamma-ray spectrum for the resonance was then obtained by adding all the foreground regions and subtracting the off-resonance background spectrum. Figure 4.5 shows part of the gamma-ray spectrum obtained from the 7.76 keV resonance in ^{54}Fe .

4.5.2 The Underlying Background

Once the gamma-ray spectrum for a particular resonance had been obtained, it was necessary to evaluate the areas under the gamma-ray peaks. As was discussed above, for small lines, the method of fitting a line under the peak through nearby background regions proved unsatisfactory, and a method was adopted in which the overall smoothness of the underlying background could be taken into account. The method was based on that of Westmeier (Wes 81).

The first stage in processing the spectrum was to take a region of 50 channels, starting at channel zero, and to fit a straight line through all the data points. If there are no peaks in a particular region, and a straight line is a good approximation to the background in this region, the number of points in the spectrum which lie above and below the straight line should be equal. Therefore the straight line fit to the 50 channel region was examined to determine if there were too many points below the

line. If the number was too large (at some statistically significant level), the point deviating most above the line was rejected as belonging to a gamma-ray peak, and a new straight line was fitted to the remaining points. This process continued until there were an acceptably equal number of points above and below the straight line fit. The final line so obtained was taken as an estimate of the background over the 50 channel region. The entire process was then repeated for another 50 channel region, which started 10 channels higher than had the previous region, and so on until the complete gamma-ray spectrum had been covered. This resulted in five different background estimates for each channel, and these were then averaged point-by-point. Finally a three-point smoothing function was applied to this averaged background.

An example of the background calculated by this method for a typical spectrum is shown in Figure 4.5. The points on the spectrum marked with a line are those which were rejected as being too high when the straight lines were fitted. Also shown on the Figure is a graph of the channel-by-channel differences of the measured spectrum from the calculated background, in which the peaks shows up clearly, and off-peak regions appear to have suitably few net counts.

4.5.3 Extracting the Peak Area

The above technique provided an estimate of the background $b(i)$ at channel i in the gamma-ray spectrum. If the spectrum value in channel i is $s(i)$ and the gamma-ray peak extends from channels l to m , then the peak area A is given by

$$A = S - B \quad (4.16)$$

where

$$S = \sum_{i=l}^m s(i) \quad (4.17)$$

and

$$B = \sum_{i=l}^m b(i). \quad (4.18)$$

Assuming for the moment that the background estimate is not systematically wrong, then the error, ΔA , on the peak area is simply governed by the counting statistics, so

$$\Delta A^2 = S + B. \quad (4.19)$$

An attempt was made to discover whether the calculated background was a good estimate of the true background by examining a region, from channels l_b to u_b , near to the peak under investigation, in which it was believed no lines were present. The mean square deviation of the spectrum points from the background over this region was evaluated, and was assumed to represent the variance on the background estimate for each channel. For a region of $(m-l+1)$ channels the variance is then just $(m-l+1)$ times as large, so the variance implied on the background to be subtracted from the peak area is

$$\Delta B^2 = \frac{(m-l+1)}{(u_b-l_b)} \sum_{i=l_b}^{u_b} [s(i) - b(i)]^2. \quad (4.20)$$

The estimate of the error produced using this formula was very close to that produced when the error in the background determination was presumed to be due to counting statistics alone, i.e. eqn. (4.19). This indicated that the calculated

background was satisfactory, as had been expected from examination by eye of graphs of the spectra and fitted background.

4.5.4 Relative Gamma-ray Transition Strengths

To obtain the final estimate of the relative strengths of the transitions in a resonance, the peak areas obtained above were used to calculate the relative strengths from eqn. (4.3). The covariance between estimates of the strength of two gamma-ray lines, of energy $E_{\gamma i}$ and $E_{\gamma j}$ is then given by

$$\frac{\text{cov}[R(E_{\gamma i}), R(E_{\gamma j})]}{R(E_{\gamma i})R(E_{\gamma j})} = \left[\frac{\Delta A(E_{\gamma i})}{A(E_{\gamma i})} \right]^2 \delta_{ij} + \frac{\text{cov}[\varepsilon(E_{\gamma i}), \varepsilon(E_{\gamma j})]}{\varepsilon(E_{\gamma i})\varepsilon(E_{\gamma j})} + \frac{\text{cov}[T(E_{\gamma i}), T(E_{\gamma j})]}{T(E_{\gamma i})T(E_{\gamma j})}. \quad (4.21)$$

Various estimates of the strength of the same line are provided from measurements of the single escape and double escape peak areas as well as the two independent results available from the two detectors. To combine these estimates, the ground state transition was arbitrarily chosen to be normalised to 100 for each detector, and then best estimates of the strengths for other transitions could be obtained by combining all the data for the particular transition, using the least squares method for evaluating a single variable. Details of this process, where covariances as calculated from eqn. (4.21) can be taken into account, may be found in Appendix C.

4.6 Shape Analysis

4.6.1 The Time-of-flight Spectrum

The method of shape analysis was applied in order to provide the absolute scale for the transition strengths, once the relative strengths had been deduced by the area analysis method. It was necessary to obtain the time-of-flight spectrum, which is used in shape analysis, for only one of the capture lines, so the strongest line could conveniently be chosen. Windows were set in peak and background gamma-ray regions, and the net area was calculated for each time-of-flight channel by the method described above, in which the background was assumed to be well represented by a straight line through off-peak regions. This approach was suitable here since the peak had a large signal-to-background ratio.

The windows defining the peak and background region were progressively altered for each time-of-flight channel to account for the changing energy of the primary gamma-ray with the kinetic energy of the incoming neutron. To set the windows for the given line, the gamma-ray spectrum was obtained for events over a small neutron energy range, chosen to ensure that the line required was clearly visible (for example the spectrum shown in Figure 4.5). The appropriate number of channels were subtracted from windows determined from this spectrum, so that they corresponded to those channels in which the gamma-ray line would have occurred had the incoming neutron had no kinetic energy. For each time-of-flight channel, the corresponding neutron energy was calculated and converted to the appropriate number of gamma-ray energy channels which were then added to the window limits before extracting the peak area. The resultant time-of-flight spectrum for the ground state transition in ^{54}Fe capture is shown in Figure 4.6.

4.6.2 Corrections to the Observed Spectrum

The raw time-of-flight spectrum obtained in the manner above had to be subjected to two corrections

- (i) for the effects of single-shot operation
- (ii) for events which occurred in the channel corresponding to zero gamma-ray energy.

If the total number of events (of all gamma-ray energies) recorded in time-of-flight channels up to and including i was Σ_i , and there were N machine pulses in the run considered, then the correction that was applied to account for the effects of single shot operation was to multiply the number of events in time-of-flight channel i by

$$C_{ss}(i) = \frac{N}{N - \Sigma_{i-1}}. \quad (4.22)$$

The correction for events in channel zero was also readily applied. If time-of-flight channel i had Z_i events recorded in gamma-ray channel zero, it was assumed that these should have been distributed throughout the gamma-ray spectrum in the same proportion as events which were recorded, i.e. pile-up events which lead to channel zero being incremented were considered to occur randomly. Thus for every gamma-ray channel at time-of-flight i , the number of events was increased by the factor

$$C_{ze}(i) = 1.0 + \frac{Z_i}{(\Sigma_i - \Sigma_{i-1}) - Z_i}. \quad (4.23)$$

This correction applied to each of the gamma-ray channels within time-of-flight channel i , so when a gamma-ray peak area was deduced, the factor $C_{ze}(i)$ could be applied to the area itself rather than to the individual gamma-ray channels. Both the above corrections to the spectrum could therefore be applied simultaneously, by multiplying the counts in time-of-flight channel i by the product of the factors $C_{ss}(i)$ and $C_{ze}(i)$.

The accuracy of these corrections was tested by observing gamma-rays from a radioactive source, with a suitably long half-life, placed above the capture sample during the experimental run. This provided several lines for which a time-of-flight spectrum could be obtained. When subjected to the above corrections, the spectra for these lines were indeed flat, as was expected for a source with a constant decay rate. The presence of the source also meant that a check could be maintained on the detector efficiency, to ensure that it was not subject to electronic drifts, by noting that the relative strengths of the lines from the source remained fixed.

4.6.3 The Yield Curve

In order to provide the yield curve for extraction of the radiative width (eqn. (4.6)), it was also necessary to obtain the time-of-flight spectrum of the 478 keV gamma-ray from the run with the ^{10}B sample. This was obtained in the same way as for observations of primary transitions in a normal sample, except that the windows for the peak were not moved up as the incident neutron energy increased, because the 478 keV gamma-ray comes from de-excitation of the first excited state of ^7Li formed in the (α, n) reaction, and therefore does not shift in energy as the incident neutron energy is altered. The spectrum obtained was however subjected to the single-shot and zero-channel corrections described above.

4.6.4 Fitting of the Yield Curve with REFIT

The code REFIT (Mox 85) was used to analyse the yield curve resulting from the above calculations. This code predicts the yield to be expected from a sample in a given geometry in a time-of-flight experiment. The multiple scattering within the sample is taken into account, and the neutron resolution function is calculated by providing the parameters of the machine pulse (width, shape, *etc.*) and the orientation of the flight path and moderator in front of the neutron-producing target. The cross-sections for the interactions in the sample are calculated using the R-matrix multi-level formalism, and these are subsequently Doppler broadened. Many of the parameters which are fed in may be allowed to vary, including an overall normalisation, an underlying background, and all the widths and positions of the resonances.

The calculation of the yield by REFIT uses a lot of CPU time, due principally to the need to follow through the history of a neutron passing through a sample in which capture may take place after undergoing multiple scattering, and so the fitting was limited to allowing the program to provide the best normalisation factor and any necessary background. An example of the fit to the observed yield of the 9298 keV gamma-ray emitted following capture in ^{54}Fe is shown in Figure 4.7.

4.6.5 Analysis of Transmission Data

Chapter 5 includes the results of a transmission measurement, carried out on the F2 flight path, which was intended to provide an estimate of the neutron background present in the time-of-flight capture measurements. The method used to estimate the background was the 'black' filter method in which the transmission sample was chosen such that at particular resonance energies essentially all neutrons interact within the sample. Any remaining neutrons being detected at these energies are assumed to be background. In practice, a resonance is rarely completely black, due to effects such as Doppler broadening and the finite timing resolution of the machine, and a code is needed to estimate how much of the remaining transmission observed at the black resonance energies arises from background neutrons. For this purpose, the REFIT code was used to analyse the transmission curve obtained, and provide an estimate of the experimental background.

The sample used for the measurements was made from manganese, and its thickness, n atoms b^{-1} , was such that the transmission,

$$T(E_R) = \exp(-\sigma_T(E_R)n) \quad (4.24)$$

at the resonance energies E_R in the region of interest ($\sim 1 \text{ keV} - 20 \text{ keV}$), was small. The transmission was measured by collecting time-of-flight spectra for gamma-rays produced by a ^{10}B sample, which was placed in the normal capture position. Two separate runs were needed; one run was with an open beam, and the second run was with the Mn sample placed in the filter position on the flight path. The transmission curve was deduced by dividing the yield obtained from the ^{10}B when the Mn was in the beam with that when it was not present.

The resulting transmission curve could then be input to the REFIT program, which was run in its transmission analysis mode. The code determines the transmission from the calculated cross-sections and the neutron resolution function in much the same way as in the capture case described above, except that the computational effort required is considerably less, since there is no need in this case to account for multiple scattering in the sample. Any interaction within the sample

is considered to remove that neutron from the beam immediately. This saving in CPU time allowed more parameters to be varied by the code than was permitted in the analysis of the capture data, and several resonance parameters could be varied as well as the normalisation and the background. The background necessary to obtain the best fit to the data was considered to be a good indication of the true background, since at the energies of the black resonances, the fit was sensitive to the underlying background.

5 PRELIMINARY MEASUREMENTS

5.1 Detector Efficiency Measurements

As indicated in Chapter 4, it was necessary to establish relative efficiency curves for each of the detectors used in these investigations, in order to be able to deduce the strengths of gamma-ray transitions in resonance capture. To cover the whole gamma-ray energy region of interest, two different sets of efficiency measurements were undertaken: one using radioactive sources and the other using thermal neutron capture spectra. The measurements are now discussed in more detail.

5.1.1 Thermal Neutron Capture Measurements

The observation of spectra following thermal neutron capture gives gamma-ray lines of known relative intensity up to high energies (~ 10 MeV), and enables values of the detector efficiency to be determined for use in the smooth function fitting process described previously. Table 5.1 shows details of the three different samples which were used in these investigations to provide the capture gamma-rays. The advantage of using thermal neutrons to produce the high energy gamma-rays was that the measurements could be made *in situ* on the F2 flight path, with exactly the same geometry as was used in the resonance capture measurements.

The experimental set-up was identical to that described in Chapter 3, except that the boron overlap filter was removed to allow thermal neutrons to be captured in the samples. Each of the samples was placed in the neutron beam in the normal position, and the machine was operated at a pulse repetition rate of 100 s^{-1} which gave an overlap energy of 8 meV, well below the peak of the Maxwellian distribution for thermal neutrons at room temperature. The enable gate was set to 2.5 ms after the machine pulse and the disable gate was set at 4.5 ms. Events were therefore recorded over the energy range 40 meV to 130 meV, which range provided the greatest count-to-background ratio. The timing of events within the thermal neutron timing gate was unimportant, so all events were combined into a single timing channel off-line before analysis of the gamma-ray spectra.

Once the data had been obtained, the analysis proceeded as described in Chapter 4, with the peak areas being evaluated for each of the strong lines, and corrections being made for the attenuation of the gamma-rays through the sample. A degree five polynomial provided an adequate fit to the relative full energy efficiency values, which were obtained by dividing the observed peak areas by published values of the relative strengths of the lines, taken from (Tul 83) for Ti and from (LT 72) for the Cr and Cl. Figure 5.1 shows the fit obtained for the PGT detector, for which a χ^2 of 1.7 per degree of freedom was obtained. The corresponding plot for the EGG detector is almost identical.

In addition to this full energy efficiency curve, the single and double escape peaks were deduced as ratios. Figure 5.2 shows the three degree polynomial fit to the ratio of the full energy peak to the single escape peak efficiency for the EGG detector. The χ^2 for the fit shown is 1.2 per degree of freedom. Once again the results were almost identical for each detector. The ratio of the double escape to single escape peak efficiency was found to be consistent with a constant value for each of the detectors (0.77 for the PGT detector and 0.83 for the EGG detector).

Table 5.1

Details of the thermal capture samples used to establish the relative efficiency curves at high gamma-ray energies for the two detectors.

Element	Chemical Form	Thickness (atoms b^{-1})
Ti	metal	0.072
Cl	NH ₄ Cl	0.013
Cr	metal	0.016

5.1.2 Standard Source Values

Complementary to the thermal measurements described above, it was necessary to obtain detailed values for the efficiency at low gamma-ray energies, particularly since the value at 478 keV must be known in order to deduce the absolute widths, and also because the efficiency is varying rapidly at this point with a large number of events being rejected through having a long rise-time.

Once more the measurements were made *in situ* with the point sources being placed at the position corresponding to the centre of a capture sample, inside the flight tube. All the electronics remained the same with a pulser providing 'start' pulses, the machine itself being off. The timing of the gamma-rays from the sources was not important so, although collected with 128 channels resolution, all events were again combined off-line into a single timing channel before carrying out the peak analysis. The two sources used were ⁵⁶Co and ¹⁵²Eu which provided an abundance of lines in the range 350 – 3500 keV. The results for the EGG detector, with a six parameter fit which gave a χ^2 value of 2.9 per degree of freedom, is shown in Figure 5.3.

The measurements with sources did not share precisely the same geometry as those of the capture gamma-ray samples, since for the capture case, the gamma-rays could originate in any part of the sample (depending on the neutron beam profile), whereas for the sources, the gamma-rays essentially came from a single point. The effect of placing the sources in different positions was therefore investigated. Only small variations were found (~ 5%) and these followed a systematic behaviour, with the ratio of the efficiency of detection of high energy to low energy gamma-ray lines being larger when the sources were very close to the detector. The reason for this behaviour was believed to be that when originating from a point close to the detector, more of the gamma-rays pass through the Ge crystal at a steep angle, and therefore on average travel through a greater thickness of the Ge detector dead layer. This increase in distance has more effect in attenuating the low energy gamma-rays than the high energy gamma-rays, and hence the relative efficiency for detection of high energy gamma-rays appears to increase. However, these effects were small, and were not considered significant, especially since the profile of the neutron beam in the capture experiment was known from the geometry of the collimation to have a maximum in the centre and to diminish towards the outside of the sample. The relative efficiency as measured at the centre of the sample was therefore adopted.

5.1.3 Combining Low and High Energy Determinations

The measurements outlined above provided two sets of full energy efficiency curves: the first set, for gamma-rays of energy > 2.0 MeV, came from the thermal neutron capture spectra, and the second, for gamma-rays < 3.5 MeV, arose from observations of the radioactive source spectra. From the small overlap of the two sets, and from the general trend of the data, a normalisation could be made to ensure that both curves were consistent in the overlapping energy range. Values for the efficiency below 3.5 MeV were then deduced from the six parameter fit to the source measurements, and those over 3.5 MeV from the five parameter fit to the thermal neutron capture gamma-ray data.

5.2 The Timing Resolution

It was necessary to ensure that the timing of events relative to their true occurrence, as obtained with the system described in Chapter 3, was made with good resolution (low jitter) and without a systematic move with respect to gamma-ray energy (walk). To measure the timing response as observed in the capture gamma-ray measurements, as much as possible of the system was kept unchanged.

Coincidence gamma-rays can be obtained from a ^{60}Co source, with 1333 keV and 1173 keV gamma-rays being produced in a cascade. Such a source was placed at the sample position whilst the machine was off, and in addition to the two detectors, a photomultiplier tube (PMT) with a fast scintillator was placed next to the source. The pulses from the PMT were input to a constant fraction discriminator and used as start pulses in the otherwise unchanged experimental set-up described in Chapter 3. The two parameter data were collected with the TAC set at 100 ns full scale, so that adequate resolution was obtained using only 128 timing channels. An exact timing calibration was provided by inserting delay cables of known length. As well as a random background, coincidence events were detected showing up as a peak in the timing spectrum. An example, for gamma-ray events occurring in coincidence in the range 810 – 920 keV for the PGT detector, is given in Figure 5.4. (Such gamma-ray events correspond to a 1332 or 1173 keV coincidence gamma-ray depositing its energy in the detector by Compton scattering. The timing response of the system is assumed to be the same as that which would have been observed had it been the full energy of the gamma-ray.)

The behaviour of the response function could be investigated by determining the timing spectrum over small ranges of gamma-ray energy, and extracting the FWHM of the peak. Figure 5.5 shows the results for the EGG detector. (The PGT detector has a similar behaviour.)

The timing response so obtained included all the factors which contribute to the experimental resolution, such as the use of discriminators to clean up the pulse shape. The additional resolution of the PMT was also present in these measurements but was negligible. The walk, as indicated by a change in the position of the peak centre, was very small (< 1 ns) and could be neglected, whilst the jitter was also small over the range measured, and was expected to continue decreasing as the gamma-ray energy increased. For the analysis of results taken with a machine pulse width of 30 ns, as in the measurements of ^{54}Fe and ^{62}Ni capture to be presented in Chapter 6, the timing response of the detectors could be ignored.

5.3 The Neutron Background Determination

In Chapter 4, it was indicated how the background present in a neutron time-of-flight experiment could be estimated using the ‘black’ resonance technique, and obtaining a fit to the observed transmission curve from the code REFIT. Such a measurement was carried out for the F2 flight path by placing a manganese sample in the filter position (see Figure 3.4) whilst a ^{10}B sample was placed in the sample position. By observing the 478 keV gamma-ray line from the ^{10}B , the sample acted as a neutron detector, and the transmission through the Mn could be deduced by comparing the ^{10}B yields with and without the filter in place.

The Mn filter was made by sintering powder into a disc of 15 cm diameter, which was large enough to cover the whole neutron beam at the filter position. It was 12.2 g cm^{-2} thick, which is equivalent to $0.133 \text{ atoms b}^{-1}$. Details of the ^{10}B sample are given in the next section. Each run lasted 16 h with HELIOS producing $\sim 4 \text{ kW}$ of power in a 30 ns pulse, at a repetition frequency of 300 s^{-1} . This length of run provided sufficient counts to give the necessary statistical accuracy.

Figure 5.6 shows the transmission curve and the best fit to these data as provided by the code REFIT. The parameters for the s -wave resonances used to give the fit are given in Table 5.2 (p -wave resonances were also included but had very little effect on the transmission). The value of the assumed constant background which provided this fit was $(9 \pm 1) \times 10^{-3}$, and the corresponding χ^2 value was 1.2 per degree of freedom.

One problem associated with measurements using the ‘black’ filter method is the effect that the filter itself has on the background that is being measured. In general, the filter will attenuate the background neutrons, so the true value for the background may well be higher than that deduced from a fit to the data. It is often assumed that, for a given time-of-flight, any background neutrons also present are still close in energy to the in-time neutrons. This is supposed since the scattering from collimators, which gives rise to most of the out-of-time neutrons, only tends to reduce their energy by a small amount. Some experimental measurements appear to bear this out (Has 78). Over the region of these measurements, the off-resonance transmission is ~ 0.5 so it is likely that the true background is $\sim 2\%$ rather than 1% . This is still not significant for the present capture measurements, and the background was therefore neglected.

Additional evidence of the presence of only a small background component to the neutron spectrum came from consideration of the off-resonance capture when a single gamma-ray line was being observed, such as that illustrated in Figure 4.6. As the potential capture is negligible at these neutron energies, any off-resonance capture can only arise from background neutrons. The small value observed therefore supports the direct measurement of a negligible background.

5.4 ^{10}B Sample Thickness Measurements

The ^{10}B sample used in determining the neutron flux from the FNT (see section 4.2), and for the background measurement described above, consisted of 7.3 g of boron powder inside an aluminium can of diameter 8.3 cm. The boron was enriched to 95.2 atom % of ^{10}B and a chemical analysis showed that 97.6% of the material was boron. The aluminium can was made in two sections; a base of thickness 0.5 mm on which the boron was spread out as evenly as possible, and a lid made from aluminium of half this thickness, which was placed on top of the boron

Table 5.2

The *s*-wave resonance parameters used to fit the ^{55}Mn transmission measurements on flight path F2. The spin-parity of the ground state of ^{55}Mn is $5/2^-$.

Energy (keV)	J^π	Neutron Width (eV)	Radiation Width (eV)
-2.83	2^-	269.0	0.5
-0.078	3^-	0.045	0.5
0.337	2^-	22.1	0.5
1.10	3^-	17.4	0.5
1.81	3^-	583.0	0.5
7.179	2^-	437.0	0.5
8.90	3^-	366.0	0.5
17.8	3^-	16.7	0.5
18.05	2^-	57.6	0.5
20.9	3^-	793.0	0.5
23.74	2^-	274.0	0.5
26.7	2^-	360.0	0.5
27.0	3^-	151.0	0.5
30.3	2^-	14.9	0.5
35.3	3^-	137.0	0.5
35.5	2^-	1320.0	0.5

powder and pressed down firmly. Repeated removal of the lid and spreading of the powder enabled an apparently uniform layer of powder to be produced. When the uniformity was considered to be satisfactory, the lid was replaced and glued into position using an epoxy resin adhesive. A small hole was drilled in the side of the can in order to allow air to escape when the sample was placed in the evacuated flight tube.

In order to see if such a thin sample (~ 2 mm) was uniform, a transmission measurement was made, to provide a direct value of the number of atoms per barn, which could be compared with that calculated on the assumption that the powder was spread uniformly throughout. The measurement was carried out using an 8.7 m flight path on the condensed matter target (CMT) of HELIOS, which had been specifically set up for transmission experiments with low energy (\sim eV) neutrons. The neutrons, observed with a lithium-glass scintillator detector, were recorded as time-of-flight events, and a sample changer allowed various filters and samples to be moved in and out of the beam remotely, whilst separate data for the filter/sample combinations were collected by a PDP-11/45 computer.

For this measurement, the ^{10}B sample was moved in and out of the beam over periods of about half-an-hour, and a run of 24 hours duration was sufficient to provide the necessary counting statistics. The transmission at four different energies was calculated by finding the ratio of the counts collected with and without the ^{10}B sample in the beam, within a small interval of time-of-flight channels. The results are summarized in Table 5.3. This simple calculation of the transmission was

Table 5.3

Results of the transmission measurement carried out on an 8.7 m flight path of the CMT on HELIOS, to determine the thickness of the ^{10}B sample used in neutron flux measurements. C_T and C_O are the counts per channel obtained respectively for the transmitted beam and for the open beam over small regions of time-of-flight centred at the value given in column 1.

TOF (μs)	Energy (eV)	C_T	C_O	Transmission (T)
68	85.2	1254 ± 12	1771 ± 14	0.71 ± 0.01
120	27.8	841 ± 10	1630 ± 10	0.52 ± 0.01
220	8.1	394 ± 8	1592 ± 16	0.247 ± 0.005
324	3.8	193 ± 4	1494 ± 10	0.129 ± 0.003

justified because the neutron background in the energy range considered is known to be less than 0.1% for this flight path (Mox 84).

For these neutron energies, the transmission T through a ^{10}B sample of thickness n atoms b^{-1} may, to a good approximation, be written as

$$T = \exp\left(-\frac{610}{\sqrt{E(\text{eV})}} n\right) \quad (5.1)$$

where E , the neutron energy, is related to the time-of-flight and path length by eqn. (3.1). A plot of $\ln T$ against time-of-flight (Figure 5.7) for the observed values of T is a straight line, and the value for n , obtained from its slope, was 7.0 ± 0.1 atoms b^{-1} . This was consistent with the value, 7.2 atoms b^{-1} , deduced from the weight of the sample, on the assumption that it was of uniform thickness.

The value of 7.0 for n was adopted in all calculations of the neutron flux, as this was a direct measurement of the thickness, whereas it was quite possible that some material may have been lost in the side of the cans, so creating a small error in the value deduced from weight considerations.

6 RESULTS

6.1 ^{54}Fe Measurements

6.1.1 Experimental Details

Measurements of the capture gamma-ray spectrum following resonance neutron capture in ^{54}Fe were made using a separated isotope sample provided by the Oak Ridge National Laboratory. The ^{54}Fe was in the form of an oxide, Fe_2O_3 , and its isotopic composition is shown in Table 6.1. The sample was made in the same way as the ^{10}B sample described in Chapter 5, with aluminium canning of a similar thickness. The quantity of iron oxide involved, 45.22 g, ensured that a good uniformity could be achieved, and the diameter of the can, 8.3 cm, provided 6.3×10^{-3} atoms b^{-1} of ^{54}Fe .

The experimental running was carried out in the manner described in Chapter 3, with the linac producing a 30 ns wide pulse at a repetition rate of 300 s^{-1} , which provided ~ 5 kW of beam power. Separate runs of 24 h duration were made and, after checking that there were no inconsistencies between the runs due to drifts in the electronics, they were added together for off-line analysis. The total period of running was the equivalent of 12 days.

Two runs were carried out with the ^{10}B sample in place, each run lasting for a period of ~ 12 h. These were also checked for consistency before being used as measurements of the neutron flux.

The data were collected with 512 time-of-flight channels and 2048 gamma-ray energy channels for each of the detectors. The TAC was set to give a timing channel width of 30 ns, and the start pulse was delayed by a suitable length of cable so that the neutron energy range covered was from 3 keV to 80 keV, although with a 30 ns pulse width, the resolution was rather poor at the higher neutron energies. These data were analysed by the methods described in Chapter 4, and the results so obtained are given below.

6.1.2 The s-wave Resonances

The time-of-flight spectrum for all gamma-rays produced in the ^{54}Fe sample having energy > 2.5 MeV is shown in Figure 4.4. The s-wave resonances at 72, 52, and 7.8 keV are evident, but the neutron energy resolution for the 72 and 52 keV resonances was insufficient to ensure separation from any narrow p-wave resonances and, together with a low count-rate, meant that analysis of the gamma-ray spectra in these resonances was not feasible. However, the gamma-ray spectrum for events occurring in the 7.8 keV resonance, part of which is shown in Figure 4.5, was suitable for analysis. The results of the analysis of this spectrum, providing information on the relative strengths of all the known E1 transitions, are given in Table 6.2.

Upper limits are given for the strengths of those transitions for which no gamma-ray lines could be seen in the spectrum. These limits were determined by setting peak windows at the positions where the lines should have appeared, and taking the calculated errors for the peak areas as an indication of the sensitivity for detection of the line. For the purpose of comparison, Table 6.2 also includes the strengths for the transitions expected from the valence model, and the only other known experimental determination of relative strengths (Ram + 80).

Table 6.1

The isotopic composition of the samples used for the capture gamma-ray measurements. The abundances of each isotope are given in atoms per cent.

Sample	Mass Number							
	54	56	57	58	60	61	62	64
⁵⁴ Fe	97.69	2.263	0.045	< 0.02				
⁶² Ni				0.47	0.55	0.15	98.83	0.02
Ni				68.3	26.1	1.1	3.6	0.9

The absolute value for the transition to the ground state was determined by the shape fitting method described in Chapter 4. Figure 4.6 shows the time-of-flight spectrum for this single gamma-ray transition, and the best fit to the deduced yield is shown in Figure 4.7. The value for the partial radiative width implied by the fit was 1.5 ± 0.3 eV, from which the values for the other partial widths, given in Table 6.2, were deduced. A breakdown of the components which contribute to the total error on the partial widths is given in Table 6.3, and may be used in assessing the correlations between the results for the different transitions.

If it is assumed that the four strong primary gamma-rays observed in the 7.8 keV resonance account for all of the gamma-ray strength, then the partial radiative width of the ground state transition will be approximately two-thirds of the total width. The implied total radiative width is then $\sim 2.3 \pm 0.5$ eV, which is consistent with the recommended value of 1.8 ± 0.3 eV given by Mughabghab *et al* (Mug + 81).

6.1.3 The p-wave Resonances

Although the study of *p*-wave resonances in this mass region is not of importance in considering the rôle to be played by non-statistical models such as the valence model, for completeness the available data on the spectra have been analysed. Referring to Figure 4.4, it can be seen that a sufficient number of events to merit analysis were observed in the *p*-wave resonances at 9.5, 11.2 and 14.5 keV. Figure 6.1 shows an example of one of the capture gamma-ray spectra; that observed in the 9.5 keV resonance. The results of the analysis of the spectra in the 9.5 and 14.5 keV resonances are summarised in Table 6.4, where, for gamma-ray energies less than 6 MeV, only transitions seen by Raman *et al* (whose data are included for comparison), or in the present measurements have been included. Because of the smaller number of events observed in these resonances, the errors on the relative strengths of the transitions are dominated by the component due to the uncertainty in the determination of the peak area. When analysing the data, a small correction was made to allow for the anisotropic nature of dipole transitions from *p*-wave capture. (The spins of the three *p*-wave resonances are all believed to be $3/2$ (Mug + 81).) No details for the 11.2 keV resonance are shown because for that resonance, the only gamma-ray observed was the strong transition to the ground state of ⁵⁵Fe.

Table 6.2

The relative strengths (normalised to 100 for the ground state transition) and partial widths for gamma-ray transitions E_γ from the 7.8 keV s -wave resonance of ^{54}Fe to final states E_x in ^{55}Fe . For comparison, the valence model predictions for the relative and absolute strengths, and the data of Raman et al for the relative strengths (Ram + 80) are also given. The values for the gamma-ray energies are those corresponding to capture by thermal neutrons.

E_x (MeV)	E_γ (MeV)	Relative Strength			Partial Width (eV)	
		Present Measurement	(Ram + 80)	Valence Model	Present Measurement	Valence Model
0.0	9.298	100 ± 10	100 ± 26	100	1.5 ± 0.3	1.21
0.413	8.885	35 ± 4	36 ± 4	31	0.5 ± 0.1	0.38
1.925	7.373	5.2 ± 2	8 ± 4	4.1	0.08 ± 0.03	0.05
2.058	7.240	< 5	< 3	8	< 0.08	0.1
2.478	6.820	6.4 ± 2	13 ± 4	14	0.10 ± 0.04	0.17
3.035	6.263	< 7	< 4	2	< 0.11	0.03
3.559	5.739	< 6	< 4	7	< 0.09	0.09
3.800	5.498	< 6	< 5	14	< 0.09	0.17
5.775	3.523	< 9	< 7	0.1	< 0.14	0.01

Table 6.3

The contributions (in per cent) to the total error for the partial radiative widths determined from the observations of capture in the 7.8 keV resonance in ^{54}Fe . The components which contribute to the total uncertainty are the peak area determination, the detector efficiency, the attenuation of the capture gamma-rays in the sample, and the normalisation either to the flux measurement run or to the ground state transition partial width as appropriate.

E_γ (MeV)	Error Components (%)				Total Error (%)
	Peak Area	Efficiency	Attenuation	Normalisation	
9.298	2	8	5	15	18
8.885	3	8	5	18	22
7.373	30	4	5	18	37
6.820	30	4	5	18	40

Table 6.4

The relative strengths (normalised to 100 for the ground state transition) of gamma-ray transitions E_γ from the 9.5 and 14.5 keV p -wave resonances of ^{54}Fe to final states E_x of spin-parity J^π in ^{55}Fe . The values for the gamma-ray energies are those corresponding to capture by thermal neutrons.

E_x (MeV)	E_γ (MeV)	J^π	Relative Strength			
			Present Results		(Ram + 80)	
			9.5 keV	14.5 keV	9.5 keV	14.5 keV
0.0	9.298	$3/2^-$	100 ± 20	100 ± 30	100 ± 26	100 ± 22
0.413	8.885	$1/2^-$	88 ± 20	125 ± 30	110 ± 23	78 ± 20
0.931	8.367	$5/2^-$	< 20	< 30	36 ± 16	< 10
1.925	7.373	$1/2^-$	18 ± 9	76 ± 30	58 ± 19	104 ± 25
2.058	7.240	$3/2^-$	30 ± 15	< 30	46 ± 19	< 15
2.478	6.820	$3/2^-$	20 ± 10	< 30	< 16	34 ± 20
3.035	6.263	$3/2^-$	< 30	< 30	30 ± 19	< 22
4.450	4.848	$1/2^+$	< 30	< 30	< 29	79 ± 40
4.494	4.804	?	< 30	< 40	< 29	100 ± 48
5.123	4.175	?	< 30	< 40	< 33	84 ± 42

From the fit to the yield for the ground state transition (Figure 4.7), the corresponding partial radiative widths for the 9.5, 11.2 and 14.5 keV resonances were deduced to be 0.17 ± 0.03 eV, 0.46 ± 0.1 eV, and 0.16 ± 0.03 eV respectively. These may be compared with total radiative width values of 0.27 ± 0.03 eV, 0.35 ± 0.04 eV, and 0.35 ± 0.04 eV respectively, given by Mughabghab *et al* (Mug + 81). From the values for the ground state partial widths, and the relative strengths given in Table 6.4, the partial widths for all the other observed transitions may also be deduced by a suitable normalisation.

6.2 ^{62}Ni Measurements

6.2.1 Experimental Details

Measurements of the capture gamma-ray spectra in ^{62}Ni were made, as for the ^{54}Fe case, using a separated isotope sample provided by the Oak Ridge National Laboratory. The isotope was in elemental form and had the composition given in Table 6.1. The sample itself was canned in aluminium in the same way as the ^{54}Fe , with a weight of 80.55 g, giving a thickness of 1.42×10^{-3} atoms b^{-1} of ^{62}Ni .

The machine running conditions were similar to the ^{54}Fe run, but the period over which the capture was observed was only 5 days. Once again two runs of 12 h duration were made with the ^{10}B sample in position to provide the neutron flux measurement. The 512 timing channels, each of width 30 ns, covered a neutron energy range from ~ 70 keV – 2.8 keV.

6.2.2 The s-wave Resonances

The time-of-flight spectrum for all gamma-ray events over 2.5 MeV in energy is shown in Figure 6.2. Over the energy range covered, the only *s*-wave resonances are those at 43 and 4.5 keV, and the 43 keV resonance has too few counts for analysis. However, the 4.5 keV *s*-wave resonance dominates the time-of-flight spectrum, and may be clearly seen, with additional structure due to the effect of the capture of scattered neutrons in Ge resonances as discussed in Chapter 4. A portion of the gamma-ray spectrum from the 4.5 keV resonance is given in Figure 6.3, and results of the calculations of the relative strengths are given in Table 6.5, where they are compared with valence model predictions and experimental thermal capture measurements (Ish + 77). Table 6.6 shows a breakdown of the errors which contribute to the partial widths (which were obtained by normalisation to the ground state width obtained using a natural nickel sample (see below)).

An attempt was made to determine the absolute value of the strong ground state transition strength by the shape analysis method used previously. However, a good fit to the yield curve for this gamma-ray line, deduced from the time-of-flight spectrum (see Figure 6.4), could not be achieved, despite attempts with a variety of different resonance parameters. The best fit which could be obtained, and which clearly does not have the correct shape, is illustrated in Figure 6.5.

It was thought that the inability to fit the data with the code REFIT was a result of inadequate modelling of the large amounts of multiple scattering taking place in the sample (REFIT predicted that the proportion of captures which occurred following multiple scattering was an order of magnitude larger than the primary capture). To test if this was the reason for the bad fit, a further measurement was undertaken, but using instead a natural nickel sample, in which the isotopic abundance of ^{62}Ni is only 3.6 % (see Table 6.1). Calculations showed that in the 4.5 keV ^{62}Ni resonance the natural nickel sample should have a factor two more primary captures than captures following multiple scattering, enabling REFIT to model accurately the various contributions. The measurements made with the natural sample are presented in section 6.3.

6.2.3 The p-wave Resonances

The only *p*-wave resonance for which sufficient events were observed to permit analysis was that at 9.4 keV. The gamma-ray spectrum for this resonance is shown in Figure 6.6, and strong transitions are seen to occur to the ground state and the first two excited states in ^{63}Ni . As these states are known to have spin-parities of $1/2^-$, $5/2^-$ and $3/2^-$ respectively (Aub + 79), and assuming that M1 primary transitions are dominant over E2 transitions, a spin assignment of $3/2^-$ may be given to this resonance.

The results for the relative strengths of the transitions which were observed is given in Table 6.7, where the components due to the peak area determinations dominate the errors. The gamma-ray observed corresponding to a transition to a final state at ~ 1670 keV has not been seen in thermal capture (Ish + 77), although (d,p) measurements have indicated states at 1657 and 1677 keV (Anf + 70). It seems likely that one of these states is being observed here and that its spin is $5/2^-$, accounting for its absence in thermal spectra and in the 4.5 keV *s*-wave spectrum, whilst permitting an E1 or M1 transition from the $3/2^-$ *p*-wave state.

Table 6.5

The relative strengths (normalised to 100 for the ground state transition) and partial widths of gamma-ray transitions E_γ from the 4.5 keV s-wave resonance of ^{62}Ni , to final states E_x of spin-parity J^π in ^{63}Ni . For comparison, the valence model predictions for the relative and absolute strengths, and the results of the relative strengths in a thermal capture measurement (Ish + 77) are also included. Gamma-ray energies are those corresponding to capture by thermal neutrons.

E_x (MeV)	E_γ (MeV)	Relative Strength			Partial Width (eV)	
		Present Measurement	Valence Model	Thermal Capture	Present Measurement	Valence Model
0.0	6.838	100 ± 5	100	100 ± 7	3.0 ± 0.6	0.34
0.155	6.683	1.3 ± 0.5	168	1.7 ± 0.1	0.04 ± 0.02	0.57
0.515	6.323	2.5 ± 0.3	44	4.8 ± 0.3	0.08 ± 0.02	0.15
1.003	5.835	5.6 ± 0.6	68	7.6 ± 0.5	0.17 ± 0.04	0.23
1.327	5.511	2.3 ± 0.4	12	2.0 ± 0.1	0.07 ± 0.02	0.04

Table 6.6

The contributions (in per cent) to the total error for the partial radiative widths determined from the observations of capture in the 4.5 keV resonance in ^{62}Ni . The components contributing to the total error are the peak area determination, the detector efficiency, the attenuation of the gamma-rays in the sample, and the normalisation either to the flux measurement run or else to the ground state transition partial width as appropriate.

E_γ (MeV)	Error Components (%)				Total Error (%)
	Peak Area	Efficiency	Attenuation	Normalisation	
6.838	0.1	4	3	20	21
6.683	40	4	2	21	45
6.323	12	5	2	21	25
5.835	8	4	2	21	23
5.511	15	4	2	21	26

Table 6.7

The relative strengths (normalised to 100 for the ground state transition) of gamma-ray transitions E_γ from the 9.4 keV p -wave resonances of ^{62}Ni to final states E_x of spin-parity J^π in ^{63}Ni . The values for the gamma-ray energies are those corresponding to capture by thermal neutrons.

E_x (MeV)	E_γ (MeV)	J^π	Relative Strength
0.0	6.838	$1/2^-$	100 ± 20
0.087	6.751	$5/2^-$	210 ± 33
0.155	6.683	$3/2^-$	150 ± 20
0.515	6.323	$3/2^-$	< 70
1.003	5.835	$1/2^-$	< 70
1.327	5.511	$3/2^-$	< 70
1.668	5.170	$5/2 ?$	110 ± 22

The yield curve for this transition (Figure 6.7) was produced and was adequately fitted by REFIT, using a value of 0.36 eV for the neutron width and 1.0 eV for the total radiation width. This gave a value of 0.2 ± 0.05 eV for the partial width of the transition, from which the other partial widths may be deduced.

6.3 Natural Nickel Measurements

6.3.1 Experimental Details

As indicated above, it was necessary to carry out some measurements of the ^{62}Ni capture using a natural nickel sample in order to reduce the contributions from multiple scattering events in the 4.5 keV resonance. The sample used was a disc of nickel metal, of 99 % chemical purity, and with a thickness of 1.8 g cm^{-2} , which gave 6.6×10^{-4} atoms b^{-1} of ^{62}Ni .

The machine running conditions were similar to the previous measurements and the total running time was 12 days for the Ni sample, and one day for the ^{10}B sample.

6.3.2 The 4.5 keV ^{62}Ni s-wave Resonance

The yield curve for the ground state transition was produced in the normal way, and the fit provided by the code REFIT, using a neutron width of 2075 eV (Mox 74), is shown in Figure 6.8.

The statistical errors on the points are large due to the small count-rate achieved with such a low abundance of ^{62}Ni in the natural nickel sample, but the fit is seen to be acceptable and the associated value deduced for the partial radiative width of

the transition is 3.0 ± 0.6 eV. Using this value, other partial radiative widths were deduced from the relative strengths of the transitions (see Table 6.5).

If it is assumed that all the strength in the resonance was observed in the measurements using the separated isotope, then the partial radiative width to the ground state accounts for approximately 85 % of the total width, i.e. the total width is predicted to be 3.5 ± 0.7 eV. This is rather large compared with the measurement of Hockenbury *et al* who give the value of 0.76 eV (Hoc + 69). However, the evaluation by Moxon (Mox 74) casts doubt on this figure, since an unreasonable value for the neutron width (1.3 keV) was used, and he suggests that the Hockenbury *et al* measurement may imply a total width as large as 1.7 eV. Bearing in mind the large uncertainty in the present measurement, and the lack of good data elsewhere, the discrepancy may not be as large as it at first appears.

7 DISCUSSION AND CONCLUSIONS

7.1 Capture in ^{54}Fe

The results for s -wave capture in ^{54}Fe , presented in Chapter 6, show clear evidence of the applicability of the valence model. The data on the partial widths given in Table 6.2 are illustrated graphically in Figure 7.1, where a comparison with the valence model is made. The agreement is seen to be good, at least for the transitions to the low-lying states. It should be noted that this agreement is one of *absolute* values, and that it confirms and extends the findings of Raman *et al* (Ram +80) that the relative strengths are as predicted by the valence model.

It should be noted that the present comparison of the *absolute* values of the partial widths is a more severe test of the valence model, since any capture mechanism which predicts a correlation between transition strengths and the (d,p) spectroscopic factors of final states leads to an apparent agreement of relative strengths. The additional prediction of the valence model is that the radiation widths of a resonance are also proportional to the neutron width of the resonance. This aspect of the model may only be confirmed by observing spectra from several resonances; by comparing measured total radiation widths with the valence model predictions (and assuming that there are no strong transitions other than those used in the valence model calculations); or by finding an agreement with absolute values of partial radiation widths in particular resonances (as in the present studies).

Besides valence capture, it was thought that these measurements might show some signs of resonance-resonance interference in the capture channel. The effect of such interference would show up as asymmetric resonance shapes in the time-of-flight spectrum of a single gamma-ray line. Interference may be evident in such a case because only a single channel is being examined, unlike in a total capture measurement in which the sum of several decay channels is observed, for which the random signs of the interference terms will lead to cancelling of the effect. Asymmetric resonances which have been observed in total capture measurements are usually attributed to the effect of scattered neutrons in the detectors, and a convincing case of interference in a capture channel has not yet been observed. Examination of the yield curve for the transition to the ground state from the 7.8 keV s -wave (Figure 4.7), shows no evidence of any asymmetry, the fit provided by the code REFIT being perfectly adequate without inclusion of interference effects. The absence of any such effects may be attributed to the fact that the 7.8 keV resonance is well separated from any other s -wave resonances.

7.2 Capture in ^{62}Ni

The results of the capture in the ^{62}Ni 4.5 keV resonance (Table 6.5) show a marked difference from the corresponding data for the ^{54}Fe 7.8 keV resonance. In the ^{62}Ni case, there is no evidence for the applicability of the valence model, with both the relative and the absolute strengths of the transitions being poorly reproduced. How can this difference be explained?

When considering the valence model, it is important to remember that higher order (compound) nuclear processes may still take place during capture. If the valence component to the partial width from resonance λ to final state μ is denoted $\Gamma_{\lambda\mu}^V$, and there is an additional compound nucleus (statistical) component to the width, $\Gamma_{\lambda\mu}^{\text{CN}}$, then the complete expression for the partial width is given by

$$\Gamma_{\gamma\lambda\mu} = \left[(\Gamma_{\gamma\lambda\mu}^V)^{1/2} + (\Gamma_{\gamma\lambda\mu}^{CN})^{1/2} \right]^2 \quad (7.1)$$

where it is apparent that a cross-term exists between the valence and the statistical component of each partial width. The effect of this cross-term, which should be of random sign, can be large even for small values of the compound nucleus contribution. For example, even if the valence component is an order of magnitude larger than the compound nuclear part, the value of the width will still differ from that due to the valence part alone by +70% or -50%, depending on the sign of the interference term. As the compound nuclear component is governed by Porter-Thomas statistics, large values for this component can be expected, even when the average partial width is small. It is therefore not surprising that valence effects are often obscured, and this appears to be the case in ^{62}Ni .

The reason that the model works so well for ^{54}Fe appears to be due to the fact that ^{54}Fe has a closed neutron shell, leading to predictions of very large valence components, sufficient in fact to ensure that the compound nuclear part does not significantly perturb the partial widths.

How might valence effects be uncovered in the presence of a statistical component to the capture? A comparison of the absolute values of the strengths should be more sensitive than a comparison of relative values, as the absolute values should fluctuate about the predictions of the model. There is in fact some indication of this in the ^{62}Ni measurements made here, where the data on the absolute strengths of the three lowest energy transitions are at least of the correct magnitude. It should also be possible to uncover the effects more readily if measurements are averaged over a series of resonances.

Having seen very little evidence of valence effects in ^{62}Ni capture, there is still the possibility that interference effects might be occurring. In particular, is this the reason that it was impossible to get a good fit to the capture data obtained with the separated ^{62}Ni isotope?

The fit to the natural nickel data (Figure 6.7) appears to be adequate without needing to include any interference terms, but there are two possible anomalies requiring some further consideration. Firstly, is there evidence of some additional structure in the region of five time-of-flight channels at about 5 keV, and secondly, is the value for the radiation width too large compared with the measurement of Hockenbury *et al* (Hoc + 69)?

The question of some structure at about 5 keV might be answered by the presence of a previously unknown p -wave resonance. However, using reasonable values for the parameters of a p -wave resonance, it was not possible to reproduce such structure using the code REFIT. It is therefore possible that there is a more fundamental reason for the unusual shape.

One possibility is that the 4.5 keV resonance is in fact two separate, interfering resonances which are close together, and appear as one. However, this was dismissed on the grounds that the gamma-ray spectrum observed in the high energy portion of the resonance was the same as that observed in the low energy part. This indicates that only one resonance is present, since similar spectra from two resonances would only be expected in the case of some non-statistical process such as valence capture, and this has been shown to be most unlikely.

Another possibility is that the shape is the result of interference with a bound level (there is evidence of a close bound level provided by the fact that the coherent scattering length is negative). If such a level contributed a large amount to the

capture at thermal energies, it would determine the corresponding gamma-ray spectrum. In Figure 7.2, a comparison is made between the transition strengths observed in the 4.5 keV resonance spectrum, and the corresponding thermal neutron capture data of Ishaq *et al* (Ish + 77) (see Table 6.5), and it is apparent that the two spectra are very similar. It would therefore appear that thermal capture is largely accounted for by the tail of the 4.5 keV resonance, and that the contribution from bound levels is small. Although possible, it therefore seems unlikely that any interference terms could be large enough to produce the structure observed.

Taking the above arguments into account, it would seem that the structure at 5 keV is just a product of the poor statistics of the data. It may, however, be necessary to investigate further the possibility of the existence of either a *p*-wave resonance at 5 keV, or of interference effects.

A corollary to the argument given above, that the contribution to thermal capture from bound levels is small, helps to answer the second question posed, concerning the measured value for the radiation width of the 4.5 keV resonance. If there is only a small contribution from bound levels, all the capture at thermal energies must be accounted for by the 4.5 keV resonance (and higher energy resonances). This implies that the radiation width of the resonance is 2.3 eV (Mox 74), which is within two standard deviations of the value deduced from the current observations (3.5 ± 0.7 eV), but contradicts the value of Hockenbury *et al* (0.76 ± 0.12 eV). There appears therefore to be no reason to reject the current figures for the partial radiative widths.

7.3 Future Measurements

These measurements have highlighted the usefulness of analysing gamma-ray spectra to deduce information concerning the capture process, and of observing single channels (gamma-rays) as a function of neutron energy to obtain absolute partial widths. They have been achieved with small systematic errors, made possible by measuring the neutron flux and detector efficiencies in the same geometry as the capture measurements, and by taking into account covariances in the efficiency determination.

However, the need to extend these measurements is evident, particularly by looking at higher neutron energies, and observing several resonances from one nuclide simultaneously. In the case of ^{54}Fe , it would be of interest to see if subsequent *s*-wave resonances provide the same spectra as the 7.8 keV resonance, in accord with the valence model and, if so, whether their strengths are proportional to the neutron widths. Further studies of ^{62}Ni capture would be of interest in revealing whether residual valence effects were present when averaged over several resonances, and in allowing more investigations of the shape of the capture resonances. It would also be useful to make measurements in other nearby nuclides, although the arguments advanced to explain the failure of the valence model for ^{62}Ni would appear to limit the number of nuclides in which valence effects would be apparent.

These investigations are part of a continuing study, and the suggestions for measurements given above are in hand. It is intended that the nuclides ^{58}Ni and ^{52}Cr (which has a closed neutron shell) will be studied, and that the extension to higher energies will be possible with increased machine output, and with running conditions optimised for this type of experiment. Although it appears that in the

mass region $A \approx 55$, single particle effects in s -wave capture will only be apparent when the valence model predicts a transition strength at least an order of magnitude larger than the statistical model, there is clearly much more exciting work to be done in this area of capture gamma-ray spectroscopy.

APPENDIX A

SOLVING THE SCHRÖDINGER EQUATION

A.1 Introduction

This appendix describes the numerical methods which were used to solve Schrödinger's equation in order to evaluate the valence width estimates. The wave function solutions correspond to the motion of a single neutron in a central potential produced by an inert nuclear core, and solutions were obtained for two different cases: an initial unbound state and a final bound state. For the initial state, a complex optical model potential was used (it was, however, real at the origin) and only the s -wave, i.e. $l = 0$, part was considered. The final state was bound in a real potential with $l = 1$.

A.2 The Radial Equation

Given a central potential, $V(r)$, the Schrödinger equation

$$H\psi = [T + V(r)]\psi = E\psi \quad (\text{A.1})$$

may be solved by the separation of variables method (see e.g. Merzbacher (Mer 70)), so that if

$$\psi(\mathbf{r}) = R(r)Y_{lm}(\theta, \phi) \quad (\text{A.2})$$

where $Y_{lm}(\theta, \phi)$ are spherical harmonics, then $R(r)$ satisfies the equation

$$\left[-\frac{\hbar^2}{2\mu r^2} \frac{d}{dr} \left(r^2 \frac{d}{dr} \right) + l(l+1) \frac{\hbar^2}{2\mu r^2} + V(r) \right] R(r) = ER(r) \quad (\text{A.3})$$

where μ is the reduced mass of the system and E is the centre-of-mass energy.

By making the substitution

$$u(r) = rR(r) \quad (\text{A.4})$$

it is found that u obeys the radial equation

$$-\frac{\hbar^2}{2\mu r^2} \frac{d^2 u}{dr^2} + \left[l(l+1) \frac{\hbar^2}{2\mu r^2} + V(r) \right] u = Eu \quad (\text{A.5})$$

so the equation may be written in the form

$$\frac{d^2 u}{dr^2} = u''(r) = f(u, r). \quad (\text{A.6})$$

A.3 Numerical Method

The equation was solved numerically, taking steps of 0.1 fm from the origin to a radial distance of 30 fm (where the nuclear potential, $V(r)$, may be taken as zero), using eqn. (A.6) and the following relations which may be deduced from a simple linear approximation:

$$u(r + 0.1) \approx u(r) + 0.1u'(r + 0.05) \quad (\text{A.7})$$

and

$$u'(r + 0.05) \approx u'(r - 0.05) + 0.1u''(r). \quad (\text{A.8})$$

In addition, it was also necessary to establish some initial values for the wave

function and its derivative near the origin, $u(0)$ and $u'(0.05)$. These were obtained by considering the boundary conditions for the radial equation.

A.4 Boundary Conditions

Boundary conditions were determined by the behaviour of the radial equation as $r \rightarrow 0$. Firstly, as the wave function must be finite everywhere, it follows from eqn. (A.4) that $u(0)$ must equal zero. Values for the derivative near the origin in general depend on the form of $V(r)$. In the two cases being considered, $V(r)$ is a negative real constant near the origin so that eqn. (A.5) approximates to

$$\frac{d^2u}{dr^2} - \frac{l(l+1)}{r^2}u - k^2u = 0. \quad (\text{A.9})$$

For the bound state, k is a completely imaginary number whereas for the unbound state it is a real number. The solution of this equation depends on the value of l , the angular momentum.

(i) $l = 0$

In this case, eqn. (A.9) becomes

$$\frac{d^2u}{dr^2} - k^2u = 0. \quad (\text{A.10})$$

Only the behaviour of an unbound state needs to be considered for the case of zero angular momentum, so k is real and the general solution to this equation is

$$u(r) = A \sin kr + B \cos kr \quad (\text{A.11})$$

for some constants A and B . The value of B must be zero in order to satisfy the condition that $u(0)$ is zero, giving, for small r ,

$$u(r) = A \sin kr \approx Akr \quad (\text{A.12})$$

and

$$u'(r) = kA \cos kr \approx Ak. \quad (\text{A.13})$$

The value of $u(0.1)$ may be chosen arbitrarily, as normalisation takes place subsequently. It was set to be 1.0 so that $u'(0.05)$ took the value 10.0.

(ii) $l \neq 0$

For small r , the centrifugal term dominates the potential, and so eqn. (A.9) becomes

$$\frac{d^2u}{dr^2} - \frac{l(l+1)}{r^2}u = 0 \quad (\text{A.14})$$

which has the general solution

$$u(r) = Ar^{l+1} + Br^{-l}. \quad (\text{A.15})$$

Once more, B must be zero in order to maintain a well-behaved wave function at the origin, and the most general physically reasonable solution is

$$u(r) = Ar^{l+1} \quad (\text{A.16})$$

which implies that

$$u'(r) = (l+1)Ar^l = (l+1)\frac{u(r)}{r}. \quad (\text{A.17})$$

The bound state being considered has $l = 1$ so, for this state, choosing $u(0.1)$ to be 1.0, required $u'(0.05)$ to be 10.0 once more.

A.5 Finding the Bound State Energy

For the bound state, the energy E was unknown (for the unbound state it was just the energy of the neutron approaching the target nucleus), and had to be found in an iterative manner. The procedure adopted was to set E to zero initially, and carry out the numerical solution of the radial equation out to 30 fm. The number of nodes (i.e. places where the wave function crosses the axis) was counted, and if there were no more than required (two for $2p_{1/2}$ and $2p_{3/2}$ states provided that the node at the origin is included), then no bound state existed for that particular potential and the procedure was aborted. Provided there were too many nodes, the value of E was reduced, initially in 5 MeV steps, until there were the correct number of nodes or fewer. Once the value of E was determined to be too negative, the energy increment of 5 MeV was reduced, and E was incremented by the new value until it was too positive (i.e. until there were too few nodes). At this point the increment was again reduced and E was decremented in value until it was once more too negative. This process continued until a criterion for the final solution was reached, or until it was clear that, within rounding errors, the best solution had been found.

The criterion adopted to decide if the final solution had been found was to ensure that the wave function had the correct number of nodes and behaved as a decaying exponential for large radii. In practice, the behaviour at large radii was satisfied provided the absolute value at 29.9 fm was greater than that at 30 fm.

The convergence to solution was rapid as the energy increment to be applied was found by interpolation of the wave function values at a radius of 30 fm for those closest energies E known to be larger and smaller than the required solution.

A.6 Normalisation of the Wave Functions

The bound state wave function was multiplied by a constant N so that its integral over all space was unity. N was therefore determined by the condition

$$\int_0^{\infty} N^2 u(r)^2 dr = 1 \quad (\text{A.18})$$

since $u(r)$ is real and equals $rR(r)$.

The unbound state was normalized so that it represented unit flux incident on the target. For an $l = 0$ wave function, the asymptotic solution as $r \rightarrow \infty$ corresponding to unit flux is

$$u_{l=0}(r) \sim \sqrt{\frac{2\mu}{\pi\hbar^2 k}} (\sin kr + \tan \delta_0 \cos kr) \quad (\text{A.19})$$

where δ_0 is the s -wave phase shift and k is the wave number of the incident neutron. The corresponding asymptotic behaviour of the derivative of the wave function is given by

$$u'_{l=0}(r) \sim \sqrt{\frac{2\mu}{\pi\hbar^2 k}} (k \cos kr - k \tan \delta_0 \sin kr). \quad (\text{A.20})$$

The value of $\tan \delta_0$ was found by matching the numerical solutions for the complex values $u(a)$ and $u'(a)$ to the asymptotic values provided by eqns. (A.19)

and (A.20). The radius a was chosen to be 15 fm, which was large enough for the asymptotic solution to be valid. The value of $\tan\delta_0$ was then given by

$$\tan \delta_0 = \frac{k(u(a)\cos ka - u'(a)\sin ka)}{u'(a)\cos ka + u(a)\sin ka}. \quad (\text{A.21})$$

Having found $\tan \delta_0$, eqn. (A.19) was used to normalize the numerical solution at radius a , and subsequently for all radii.

APPENDIX B

EXPRESSIONS FOR OBSERVABLES

B.1 The s-wave Scattering Matrix Element

The solution of the optical model wave function for $l = 0$ allows certain experimental observables to be estimated. The s -wave scattering matrix element S_0 is related to the s -wave phase shift, δ_0 , by the expression

$$S_0 = \frac{1 + i \tan \delta_0}{1 - i \tan \delta_0}. \quad (\text{B.1})$$

B.2 The s-wave Neutron Strength Function

The above relationship may be used to deduce the s -wave neutron strength function from the formula (Hod 63)

$$\frac{g_J \bar{\Gamma}_n^0}{\bar{D}_0} = \frac{1}{2\pi\sqrt{E}} [2(1 - \text{Re}S_0) - |1 - S_0|^2] \quad (\text{B.2})$$

where $\bar{\Gamma}_n^0$ is the mean of the reduced neutron widths of the s -wave resonances (the reduced widths are defined as $\Gamma_n \sqrt{1eV/E_R}$ for a resonance at energy E_R with neutron width Γ_n), and \bar{D}_0 is the mean level separation of the s -wave resonances. g_J is the usual statistical spin factor for a resonance of total angular momentum J .

B.3 The Scattering Radius

The scattering radius R' may also be deduced from S_0 ,

$$R' = \frac{|1 - S_0|}{2k} \quad (\text{B.3})$$

where k is the neutron wave number.

APPENDIX C

ERROR ANALYSIS USING COVARIANCES

C.1 Introduction

When carrying out an error analysis of experimental data, it should be remembered that correlations may exist between the variables which contribute to the total error. If these correlations are small, they may usually be ignored without producing any significant differences to the result of the analysis. However, if the correlations are large, inclusion of their effects may change not only the estimate of the experimental error, but also, when fitting functions to experimental data for evaluation or interpolation purposes, the value of the fitted function itself.

It was realized that there were strong correlations affecting much of the data analysis of the capture gamma-ray spectra in the present work, and therefore covariance information was included wherever it was deemed to be significant. This appendix describes the mathematical detail involved in propagating the errors of functions having correlated variables, and also the use of the least squares fitting procedure for the case of correlated data points. Examples are given which illustrate how the general formulae apply to some specific cases in the analysis of the capture gamma-ray data.

C.2 Definitions

If there are n random variables x_i ($i = 1, \dots, n$) described by some joint probability distribution function, the covariance of any two variables x_i and x_j is defined as

$$\text{cov}[x_i, x_j] = \text{cov}[x_j, x_i] \equiv E[(x_i - \mu_i)(x_j - \mu_j)] \quad (\text{C.1})$$

where $E[x]$ denotes the expectation value of variable x , and where $\mu_k = E[x_k]$.

The special case of the covariance of a variable with itself is the familiar variance statistic

$$\sigma^2(x_i) \equiv \text{cov}[x_i, x_i] = E[(x_i - \mu_i)^2] \quad (\text{C.2})$$

and the error on the variable x_i is just the square root of the variance, $\sigma(x_i)$. This leads to the definition of the correlation coefficient $\rho(x_i, x_j)$ for the variables x_i and x_j , which is a number lying between -1 and $+1$ indicating the degree of correlation between the variables. It is related to the covariance by

$$\rho(x_i, x_j) \equiv \frac{\text{cov}[x_i, x_j]}{\sigma(x_i)\sigma(x_j)}. \quad (\text{C.3})$$

Frequently the values for the covariances or correlation coefficients are put into the form of an $(n \times n)$ matrix. The covariance matrix V_x has components

$$(V_x)_{ij} = \text{cov}[x_i, x_j] \quad (\text{C.4})$$

and the corresponding correlation matrix C_x has components

$$(C_x)_{ij} = \rho(x_i, x_j). \quad (\text{C.5})$$

Similarly, the error vector E_x for the variables x_i may be defined as a column vector with components

$$(E_x)_i = \sigma(x_i). \quad (\text{C.6})$$

From these definitions it is apparent that the diagonal elements of the covariance matrix are the variances of the variables. Therefore, once the full covariance matrix has been established in a particular case, the errors are also known and a separate calculation is unnecessary.

C.3 The Propagation of Errors

An experiment frequently involves the measurement of n variables x_i ($i = 1, \dots, n$) from which some quantity of interest, f , which is a function of these variables may be deduced. As the variables are only determined to within experimental errors and, in general, also have covariance terms relating them, there is an associated uncertainty in the calculated value of f . More generally, a second quantity g may be deduced from the same set of measured variables x_i . In this case there will be non-zero covariance terms between the estimates of f and g .

It can be shown (see e.g. (Smi 81)) that

$$\text{cov}[f,g] = (\mathbf{S}_f \cdot \mathbf{E}_x)^T \cdot \mathbf{C}_x \cdot (\mathbf{S}_g \cdot \mathbf{E}_x) \quad (\text{C.7})$$

where \mathbf{S}_h denotes a sensitivity matrix of size $(n \times n)$ for the function h with elements

$$(\mathbf{S}_h)_{ij} = \begin{cases} \frac{\partial h}{\partial x_i}, & i = j \\ 0, & i \neq j \end{cases} \quad (\text{C.8})$$

\mathbf{E}_x is the error vector for the variables x_i , and \mathbf{C}_x is the corresponding correlation matrix.

Further, it may readily be shown from eqn. (C.7) that the covariance between a particular variable x_j (which may itself be a function of other variables), and a function f is given by

$$\text{cov}[f, x_j] = \text{cov}[x_j, f] = \sum_{i=1}^n \frac{\partial f}{\partial x_i} \text{cov}[x_j, x_i]. \quad (\text{C.9})$$

Successive use of eqn. (C.9) allows all the necessary error propagation to be carried out.

C.4 Example: Relative Transition Strengths

In the body of the text, it is shown that the relative strength $R(E_i)$ of a gamma-ray line of energy E_i may be deduced from the measured peak area $A(E_i)$, the gamma-ray detector efficiency $\epsilon(E_i)$, and the transmission of the gamma-ray through the sample and shielding $T(E_i)$, with the relation

$$R(E_i) = \frac{A(E_i)}{\epsilon(E_i)T(E_i)}. \quad (\text{C.10})$$

It is necessary to know not only the error on the value of $R(E_i)$ but also its covariance with the relative strength deduced for another gamma-ray line, $R(E_j)$. The covariance will be non-zero because, although the peak areas for different gamma-ray energies are not correlated, the efficiency and transmission terms are.

If the following identities are made,

$$\begin{aligned}x_1(E_i) &= A(E_i) \\x_2(E_i) &= 1/\varepsilon(E_i) \\x_3(E_i) &= 1/T(E_i)\end{aligned}\quad (\text{C.11})$$

then the example may be seen to belong to the general set of problems of evaluating $\text{cov}[f(E_i), f(E_j)]$ for a function, f , of the form

$$f(E) = \prod_p x_p(E). \quad (\text{C.12})$$

To solve this problem, eqn. (C.9) may be applied, giving

$$\begin{aligned}\text{cov}[f(E_i), f(E_j)] &= \sum_k \left. \frac{\partial f}{\partial x_k} \right|_{E_i} \text{cov}[f(E_j), x_k(E_i)] \\ &= \sum_k \frac{f(E_i)}{x_k(E_i)} \text{cov}[f(E_j), x_k(E_i)].\end{aligned}\quad (\text{C.13})$$

Using eqn. (C.9) a second time, it is found that

$$\begin{aligned}\text{cov}[f(E_j), x_k(E_i)] &= \sum_l \left. \frac{\partial f}{\partial x_l} \right|_{E_j} \text{cov}[x_k(E_i), x_l(E_j)] \\ &= \sum_l \frac{f(E_j)}{x_l(E_j)} \text{cov}[x_k(E_i), x_l(E_j)]\end{aligned}\quad (\text{C.14})$$

so the covariance is determined by the equation

$$\frac{\text{cov}[f(E_i), f(E_j)]}{f(E_i)f(E_j)} = \sum_{kl} \frac{\text{cov}[x_k(E_i), x_l(E_j)]}{x_k(E_i)x_l(E_j)}. \quad (\text{C.15})$$

For the problem being considered, the covariances between x_k and x_l are all zero unless $k = l$, so

$$\begin{aligned}\frac{\text{cov}[R(E_i), R(E_j)]}{R(E_i)R(E_j)} &= \frac{\text{cov}[A(E_i), A(E_j)]}{A(E_i)A(E_j)} + \frac{\text{cov}[1/\varepsilon(E_i), 1/\varepsilon(E_j)]}{1/\varepsilon(E_i)1/\varepsilon(E_j)} \\ &\quad + \frac{\text{cov}[1/T(E_i), 1/T(E_j)]}{1/T(E_i)1/T(E_j)}.\end{aligned}\quad (\text{C.16})$$

It can be shown from eqn. (C.9) that

$$\text{cov}[1/x, 1/y] = \frac{\text{cov}[x, y]}{x^2 y^2} \quad (\text{C.17})$$

and also that, as the peak areas are uncorrelated, the only non-zero covariance term for the variable A is the variance, $\Delta A^2(E_i)$, so

$$\begin{aligned}\frac{\text{cov}[R(E_i), R(E_j)]}{R(E_i)R(E_j)} &= \frac{\Delta A^2(E_i)}{A(E_i)A(E_j)} \delta_{ij} + \frac{\text{cov}[\varepsilon(E_i), \varepsilon(E_j)]}{\varepsilon(E_i)\varepsilon(E_j)} \\ &\quad + \frac{\text{cov}[T(E_i), T(E_j)]}{T(E_i)T(E_j)}.\end{aligned}\quad (\text{C.18})$$

C.5 Linear Least Squares Fitting

The dependence of an experimentally determined quantity y on a variable x can frequently be expressed in the linear functional form

$$y(x) = \sum_{k=1}^m p_k \psi_k(x) \quad (\text{C.19})$$

where the m parameters p_k ($k = 1, \dots, m$) are unknown. The fitting problem is to determine values of the parameters which best explain the observed behaviour of y as a function of x . This may be achieved by making a series of n experimental measurements of y for different values of x , yielding n pairs of points, (y_i, x_i) ($i = 1, \dots, n$). The best estimates of the parameters \hat{p}_k may then be defined as those values which minimize the χ^2 statistic, defined as

$$\chi^2 = (\mathbf{Y} - \hat{\mathbf{Y}})^T \cdot \mathbf{V}_y^{-1} \cdot (\mathbf{Y} - \hat{\mathbf{Y}}) \quad (\text{C.20})$$

where the column vectors \mathbf{Y} and $\hat{\mathbf{Y}}$ have components

$$Y_i = y_i \quad (\text{C.21})$$

and

$$\hat{Y}_i = \sum_{k=1}^m \hat{p}_k \psi_k(x_i) \quad (\text{C.22})$$

and where \mathbf{V}_y is the covariance matrix for the observed values y_i .

If the values \hat{p}_k are expressed as a column vector $\hat{\mathbf{p}}$ so the i th component is the value of \hat{p}_i , it can be shown (Mar 71) that

$$\hat{\mathbf{p}} = \mathbf{V}_{\hat{\mathbf{p}}} \cdot \mathbf{A}^T \cdot \mathbf{V}_y^{-1} \cdot \mathbf{Y} \quad (\text{C.23})$$

where $\mathbf{V}_{\hat{\mathbf{p}}}$ is the covariance matrix for the parameter values and is given by

$$\mathbf{V}_{\hat{\mathbf{p}}} = (\mathbf{A}^T \cdot \mathbf{V}_y^{-1} \cdot \mathbf{A})^{-1}. \quad (\text{C.24})$$

The design matrix \mathbf{A} relates the values of $\hat{\mathbf{Y}}$ to the parameters $\hat{\mathbf{p}}$ through the equation

$$\hat{\mathbf{Y}} = \mathbf{A} \cdot \hat{\mathbf{p}} \quad (\text{C.25})$$

so that

$$A_{lm} = \psi_m(x_l). \quad (\text{C.26})$$

Once the best set of parameters has been determined using eqns. (C.21 – C.26), values of y may be predicted for different values of x using eqn. (C.19). Any two such estimates, y_1 and y_2 , for x values x_1 and x_2 will have correlated errors, since they depend on the same set of parameters $\hat{\mathbf{p}}$, which are uncertain through the covariance matrix $\mathbf{V}_{\hat{\mathbf{p}}}$.

By application of eqn. (C.9) to expressions for two different estimates of y , it can easily be shown that

$$\text{cov}[y_1, y_2] = \boldsymbol{\Psi}_1^T \cdot \mathbf{V}_{\hat{\mathbf{p}}} \cdot \boldsymbol{\Psi}_2 \quad (\text{C.27})$$

where $\boldsymbol{\Psi}_j$ is a column vector with components

$$(\boldsymbol{\Psi}_j)_i = \psi_i(x_j). \quad (\text{C.28})$$

C.6 The Fitting of Polynomials

One simple choice for the functions ψ_k in eqn. (C.19) is

$$\psi_m(x) = x^{m-1} \quad (\text{C.29})$$

so that y is expressed as a polynomial in x of order m , and the fitted parameters are just the coefficients of the polynomial. There is, however, a problem encountered

when this choice of functions is adopted, due to the ill-conditioned behaviour of the covariance matrix for the parameter values, defined by eqn. (C.24). It is possible to choose a set of polynomials, known as orthogonal polynomials, which avoids this problem. They are defined by the relations

$$\begin{aligned}\psi_1(x) &= 1/2 \\ \psi_2(x) &= 1/2(2x + \beta_1) \\ \psi_{r+1}(x) &= (2x + \beta_r)\psi_r(x) + \gamma_{r-1}\psi_{r-1}(x)\end{aligned}\quad (\text{C.30})$$

and the functions β and γ are given by

$$\beta_r = \frac{-2 \sum_j W(x_j)x_j\psi_r^2(x_j)}{\sum_j W(x_j)\psi_r^2(x_j)} \quad r = 1, 2, \dots \quad (\text{C.31})$$

and

$$\gamma_{r-1} = \frac{-\sum_j W(x_j)x_j\psi_r^2(x_j)}{\sum_j W(x_j)\psi_{r-1}^2(x_j)} \quad r = 2, 3, \dots \quad (\text{C.32})$$

where the weights $W(x_j)$ are the reciprocals of the variances of y_j at the points x_j .

With this choice of functions, the resultant covariance matrix for the parameters, V_p is well-defined. If the covariance matrix for the experimental data points has zero off-diagonal elements (i.e. there are no correlations present), then this choice of polynomials diagonalizes the parameter covariance matrix. In the more general case where some correlations are present, it allows the use of single precision arithmetic on a computer without introducing problems due to rounding errors, provided that the values of x_i are also normalized to lie within the range $-1 < x_i < 1$.

The equations of section C.5 may now be applied, once the design matrix, A has been constructed using relations (C.26) and (C.30).

C.7 Applications of Polynomial Fitting

The simplest application of the method given in the previous section is the evaluation of the best estimate of a single physical variable of which several, correlated measurements have been made. This may be looked upon as fitting a polynomial of degree one (i.e. a constant) to the various measurements. A useful feature of following this procedure is that the evaluation so obtained has an associated χ^2 statistic as well as an error. Some idea is therefore given of how consistent the contributing data are.

If the precise behaviour of a physical variable y as a function of x is unknown, or is highly complex, but its general behaviour is thought to be smooth (e.g. the detection efficiency of a Ge detector as a function of gamma-ray energy), then it can be useful to attempt a polynomial fit of $\ln y$ in terms of $\ln x$. In this case the following substitutions are made

$$z = \ln y \quad (\text{C.33})$$

and

$$t = \ln x \quad (\text{C.34})$$

so that z is fitted as an (orthogonal) polynomial of t .

To apply the equations of section C.5, it is necessary to find the covariance matrix for the new variable z , from the covariances of y , the measured variable. Eqn. (C.9), and the definition of z gives the required relation

$$V_{zij} = \text{cov}[z_i, z_j] = \frac{\text{cov}[y_i, y_j]}{y_i y_j}. \quad (\text{C.35})$$

Once the fitted set of parameters has been obtained, values of z may be predicted for any value of t in the normal way for a polynomial. The corresponding values of y and x are then obtained from eqns. (C.33) and (C.34), and the covariances between the estimates of y are deduced from calculations of the covariances for z , eqn. (C.27), and the transformation to the variable y with eqn. (C.35).

REFERENCES

- (AC 85) B.J. Allen and F.Z. Company, in *Capture Gamma-ray Spectroscopy and Related Topics – 1984*, American Institute of Physics, New York, (1985) p. 501.
- (AM 70) A. Asami and M.C. Moxon, *J. nucl. Energy* **24** 85 (1970).
- (AM 79) B.J. Allen and A.R. de L. Musgrove, *Adv. Nucl. Phys.* **10** 129 (1979).
- (Ama + 35) E. Amaldi, O. D'Agostino, E. Fermi, B. Pontecorvo, F. Rasetti and E. Segrè, *Proc. Roy. Soc.* **A149** 522 (1935).
- (Anf + 70) T.R. Anfinsen, K. Bjørndal, A. Graue, J.R. Lien, G.E. Sandvik, L.O. Tveita, K. Ytterstad and E.R. Cosman, *Nucl. Phys.* **A157** 561 (1970).
- (Aub 79) R.L. Auble, *Nucl. Data Sheets* **28** 585 (1979).
- (Axe 62) P. Axel, *Phys. Rev.* **126** 671 (1962).
- (Bar + 73) G.A. Bartholemew, E.D. Earle, A.J. Ferguson, J.W. Knowles and M.A. Lone, *Adv. Nucl. Phys.* **7** 229 (1973).
- (Bee 69) M. Beer, *Phys. Rev.* **181** 1422 (1969).
- (Bee 71) M. Beer, *Ann. of Phys.* **65** 181 (1971).
- (Bet 35) H.A. Bethe, *Phys. Rev.* **47** 747 (1935).
- (BM 73) E. Borridy and C. Mahaux, *Nucl. Phys.* **A209** 604 (1973).
- (Boc 59) C.K. Bockelman, *Nucl. Phys.* **13** 205 (1959).
- (Boh 36) N. Bohr, *Nature*, London. **137** 344 (1936).
- (Bri 55) D.W. Brink, Thesis, Oxford University (unpublished, 1955), and in *Proc. Int. Conf. on Nucl. Phys. with Reactor Neutrons*, Argonne National Lab. Report ANL-6797 (Ed. F.E. Throw), p. 194. (1963).
- (BT 67) L.M. Bollinger and G.E. Thomas, *Phys. Rev. Lett.* **18** 1143 (1967).
- (BW 52) J.M. Blatt and V.F. Weisskopf, in *Theoretical Nuclear Physics*, John Wiley and Sons, New York (1952).
- (Cam 59) A.G.W. Cameron, *Can. J. Phys.* **37** 322 (1959).
- (Car + 82) R.F. Carlton, S. Raman and E.T. Journey, in *Neutron Capture Gamma-ray Spectroscopy and Related Topics 1981*, The Institute of Physics, Bristol (1982) p. 375.
- (CC 71) Z.H. Cho and R.L. Chase, *Nucl. Instr. and Meth.* **98** 335 (1971).
- (Cha + 77) W.S. Chapman, D.A. Boyce, J.B. Brisland, A.E. Langman, D.V. Morris, M.G. Schomberg and D.A. Webb, *UKAEA Report AERE-R 8597* (1977).
- (Chr 84) R.E. Chrien, in *Neutron Radiative Capture*, Pergamon Press, Oxford, (1984) p. 187.
- (Cif 82) Ö. Ciftcioglu, *Nucl. Instr. and Meth.* **198** 391 (1982).
- (CM 75) J. Cugnon and C. Mahaux, *Ann. of Phys.* **94** 128 (1975).
- (Cug 76) J. Cugnon, *Nucl. Phys.* **A263** 61 (1976).
- (Deb 85) K. Debertin, *Nucl. Instr. and Meth. for Phys. Res.* **226** 566 (1985).
- (Enc + 85) Z. Enchen, H. Junde, Z. Chunmei, L. Xianc and W. Lizheng, *Nucl. Data Sheets* **44** 594 (1985).
- (Fer + 34) E. Fermi, E. Amaldi, O. D'Agostino, F. Rasetti and E. Segrè, *Proc. Roy. Soc.* **A146** 438 (1934).
- (FM 63) R.H. Fulmer and A.L. McCarthy, *Phys. Rev.* **131** 2133 (1963).
- (Gro 55) L.V. Groschev, *Dohl. Akad. Nauk*, SSSR, **100** 651 (1955).
- (Gro + 58) L.V. Groschev, A.M. Demidov, U.N. Lutsenko and V.I. Pelekhov, in *Proceedings on the Peaceful Uses of Atomic Energy Second Geneva Conference*, Vol. 15, (1958) p. 138.
- (Gro + 59) L.V. Groschev, A.M. Demidov, U.N. Lutsenko and V.I. Pelekhov, *Atlas of*

- Gamma-ray Spectra from Radiative Capture of Thermal Neutrons*. Pergamon Press, London. (1959).
- (GT 48) M. Goldhaber and E. Teller, *Phys. Rev.* **74** 1046 (1948).
- (Gya + 74) B. Gyarmati, A.M. Lane and J. Zimanyi, *Phys. Lett.* **50B** 316 (1974).
- (Has 78) T.J. Haste, *UKAEA Report AERE-R 8967* (1978).
- (HC 78) D. Halderson and B. Castel, *Phys. Rev. C* **18** 1542 (1978).
- (Hoc + 69) R.W. Hockenbury, E.M. Bartolome, J.R. Tarareczuk, W.R. Moyer and R.C. Block, *Phys. Rev.* **178** 1746 (1969).
- (Hod 63) P.E. Hodgson, in *The Optical Model of Elastic Scattering*, Clarendon Press, Oxford (1963) p. 25.
- (Hod 71) P.E. Hodgson, in *Nuclear Reactions and Nuclear Structure*, Clarendon Press, Oxford (1971) p. 129.
- (Hod 82) P.E. Hodgson, private communication (1982).
- (Hon + 80) J. Honzatko, K. Konecny, F. Bečvář and E.A. Eissa, *Czech. J. Phys.* **B30** 763 (1980).
- (HR 61) J. Humblet and L. Rosenfeld, *Nucl. Phys.* **26** 529 (1961).
- (Hub 82) J.H. Hubbell, *Int. J. Appl. Radiat. Isot.* **33** 1269 (1982).
- (Hut + 74) G.A. Huttlin, S. Sen, W.A. Yoh and A.A. Rollefson, *Nucl. Phys.* **A227** 389 (1974).
- (Ish + 77) A.F.M. Ishaq, A. Robertson, W.V. Prestwich and T.J. Kennett, *Z. Physik A* **281** 365 (1977).
- (KB 54) B.B. Kinsey and C.A. Bartholomew, *Phys. Rev.* **93** 1260 (1954).
- (Kla 85) H.V. Klapdor, in *Capture Gamma-ray Spectroscopy and Related Topics – 1984*, American Institute of Physics, New York, (1985) p. 732.
- (KH 72) D.C. Kocher and W. Haeblerli, *Nucl. Phys.* **A196** 225 (1972).
- (Kom + 84) H. Komano, M. Igashira, M. Shimizu and H. Kitazawa, *Phys. Rev. C* **29** 345 (1984).
- (Kop + 84) J. Kopecky, M.G. Delfini and R.E. Chrien, *Nucl. Phys.* **A427** 413 (1984).
- (KP 39) P.L. Kapur and R. Peierls, *Proc. Roy. Soc.* **A166** 277 (1939).
- (Kra + 68) H.W. Kraner, C. Chasman and K.W. Jones, *Nucl. Instr. and Meth.* **62** 173 (1968).
- (KW 81) K. Kandiah and G. White, *IEEE Trans. on Nucl. Sci.* **NS-28** 613 (1981).
- (Lan 59) A.M. Lane, *Nucl. Phys.* **11** 625 (1959).
- (Lan 71) A.M. Lane, *Ann. of Phys.* **63** 171 (1971).
- (Lan 74) A.M. Lane, *Phys. Lett.* **50B** 204 (1974).
- (Lan 82) A.M. Lane, private communication (1982).
- (Lea 34) D.F. Lea, *Nature* **133** 24 (1934).
- (Len 70) E.M. Lent, *Lawrence Radiation Lab. Report UCRL-50857* (1970).
- (LL 60) A.M. Lane and J.E. Lynn, *Nucl. Phys.* **17** 553,586 (1960).
- (LM 74) A.M. Lane and S.F. Mughabghab, *Phys. Rev. C* **10** 417 (1974).
- (LT 58) A.M. Lane and R.G. Thomas, *Rev. Mod. Phys.* **30** 257 (1958).
- (LT 72) G.D. Loper and G.E. Thomas, *Nucl. Instr. and Meth.* **105** 453 (1972).
- (LW 55) A.M. Lane and D.N. Wilkinson, *Phys. Rev.* **97** 1199 (1955).
- (LW 55a) A.M. Lane and E.P. Wigner, *Phys. Rev.* **98** 693 (1955).
- (Lyn 68) J.E. Lynn, in *The Theory of Neutron Resonance Reactions*, Clarendon Press, Oxford (1968) p. 326.
- (Lyn 79) J.E. Lynn, *Atom* **276** 263 (1979).
- (Mar 71) B.R. Martin, in *Statistics for Physicists*, Academic Press Inc., London (1971) p. 86.
- (Mas 85) J.P. Mason, *Nucl. Instr. and Meth. for Phys. Res.* **A241** 207 (1985).
- (McC + 81) C.M. McCullagh, M.L. Stelts and R.E. Chrien, *Phys. Rev. C* **23** 1394 (1981).
- (Mer 70) E. Merzbacher, in *Quantum Mechanics*, second edition, John Wiley & Sons, New York, (1970) p. 176.

- (MG 68) R.L. Macklin and J.H. Gibbons, *Phys. Rev.* **165** 1147 (1968).
(Mol 63) P.A. Moldauer, *Nucl. Phys.* **47** 65 (1963).
(Mor 83) D.V. Morris, *Harwell Internal Document HL 83/3504* (1983).
(Mox 74) M.C. Moxon, *UKAEA Report AERE-R 7568* (1974).
(Mox 82) M.C. Moxon, private communication (1982).
(Mox 84) M.C. Moxon, private communication (1984).
(Mox 85) M.C. Moxon, *UKAEA Report AERE-R 11986* (1985).
(MP 64) J.R. Maxwell and W.C. Parkinson, *Phys. Rev.* **1352** B82 (1964).
(MT 36) P.B. Moon and R. Tillman, *Proc. Roy. Soc.* **153** 421 (1936).
(Mug + 71) S.F. Mughabghab, R.E. Chrien, O.A. Wasson, G.W. Cole and M.R. Bhat, *Phys. Rev. Lett.* **26** 1118 (1971).
(Mug 79) S.F. Mughabghab, *Phys. Lett.* **81B** 93 (1979).
(Mug + 81) S.F. Mughabghab, M. Divadeenam and N.E. Holden, in *Neutron Cross Sections Volume 1*, Academic Press, New York (1981).
(Mug + 82) S.F. Mughabghab, M.A. Lone and B.C. Robertson, *Phys. Rev. C* **26** 2698 (1982).
(Nel 82) J.M. Nelson, private communication (1982).
(Peh + 79) R.H. Pehl, N.W. Madden, J.H. Elliot, T.W. Raudorf, R.C. Trammell and L.S. Darken, Jr., *IEEE Trans. on Nucl. Sci.* **NS-26** 322 (1979).
(PT 56) C.E. Porter and R.G. Thomas, *Phys. Rev.* **104** 483 (1956).
(Ram + 80) S. Raman, G.G. Slaughter, J.C. Wells and B.J. Allen, *Phys. Rev. C* **22** 328 (1980).
(Ras + 36) F. Rasetti, E. Segrè, G. Fink, J.R. Dunning and G.B. Pegram, *Phys. Rev.* **49** 104 (1936).
(Ros + 56) A.A. Ross, H. Mark and R.D. Lawson, *Phys. Rev.* **102** 1613 (1956).
(SA 73) A.M.J. Spits and J.A. Akkermans, *Nucl. Phys.* **A215** 260 (1973).
(Smi 81) D.L. Smith, *Argonne National Lab. Report ANL/NDM-62* (1981).
(Sol 74) V.G. Soloviev, in *Neutron Capture Gamma-ray Spectroscopy, Reactor Centrum Nederland, Petten, Netherlands* (1974).
(Sym 82) D.B. Syme, private communication (1982).
(TC 80) T. Taylor and J.A. Cameron, *Nucl. Phys.* **A337** 389 (1980).
(Tho 51) R.G. Thomas, *Phys. Rev.* **84** 1061 (1951).
(Tul 83) J.K. Tuli, *Brookhaven National Laboratory Report BNL-NCS-51647* (1983).
(TW 52) T. Teichmann and E.P. Wigner, *Phys. Rev.* **87** 123 (1952).
(Vog 62) E. Vogt, *Rev. Mod. Phys.* **34** 723 (1962).
(Wat 83) E. Wattecamps, *Nuclear Data Standards for Nuclear Measurements, IAEA Technical Reports Series 227* (1983).
(WB 36) E.P. Wigner and G. Breit, *Phys. Rev.* **49** 519 (1936).
(WE 47) E.P. Wigner and L. Eisenbud, *Phys. Rev.* **71** 29 (1947).
(Wei + 79) H. Weigmann, S. Raman, J.A. Harvey, R.L. Macklin and G.G. Slaughter, *Phys. Rev. C* **20** 115 (1979).
(Wel + 78) J.C. Wells, S. Raman and G.G. Slaughter, *Phys. Rev. C* **18** 707 (1978).
(Wes 81) W. Westmeier, *Nucl. Instr. and Meth.* **180** 205 (1981).

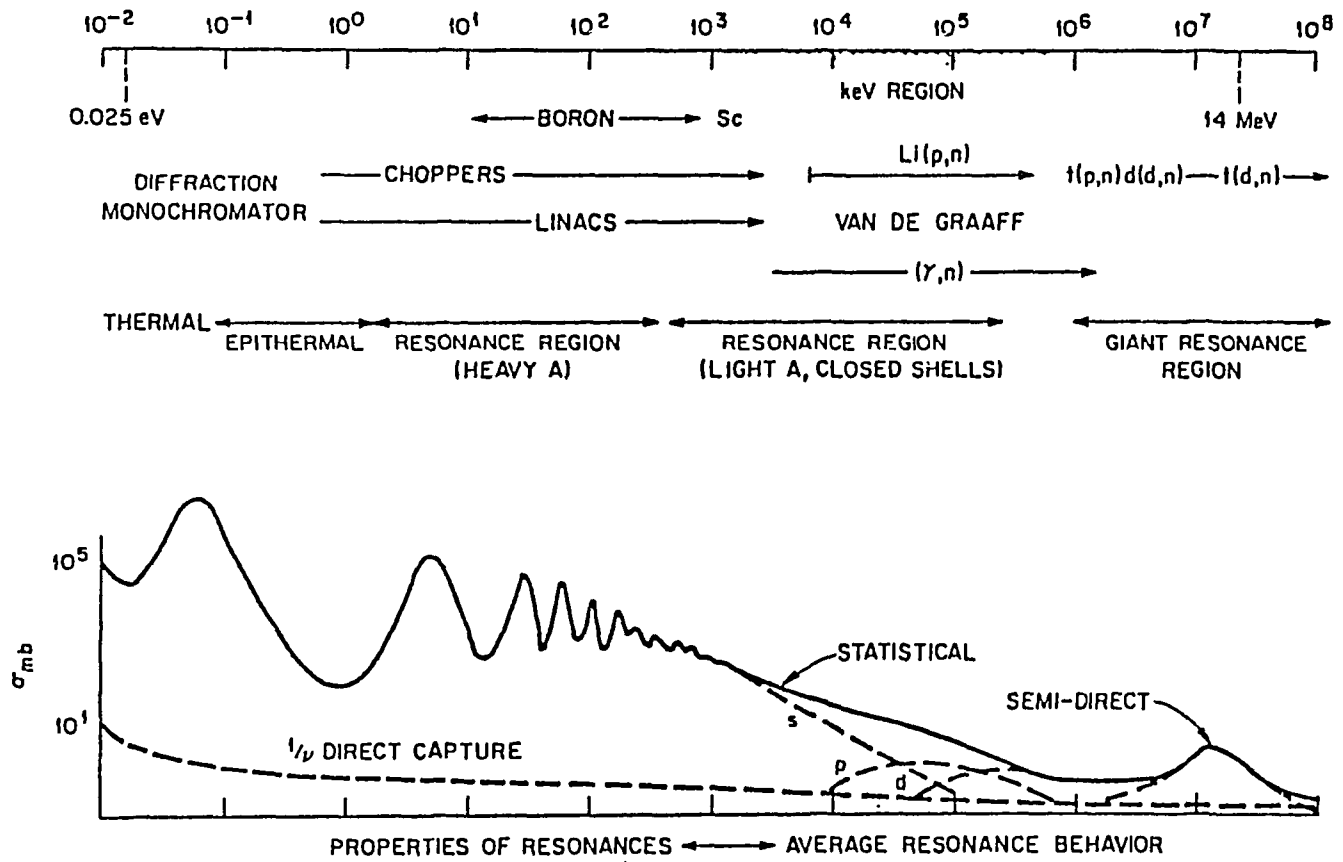


Fig. 1.1. Neutron capture research over nine orders of magnitude.

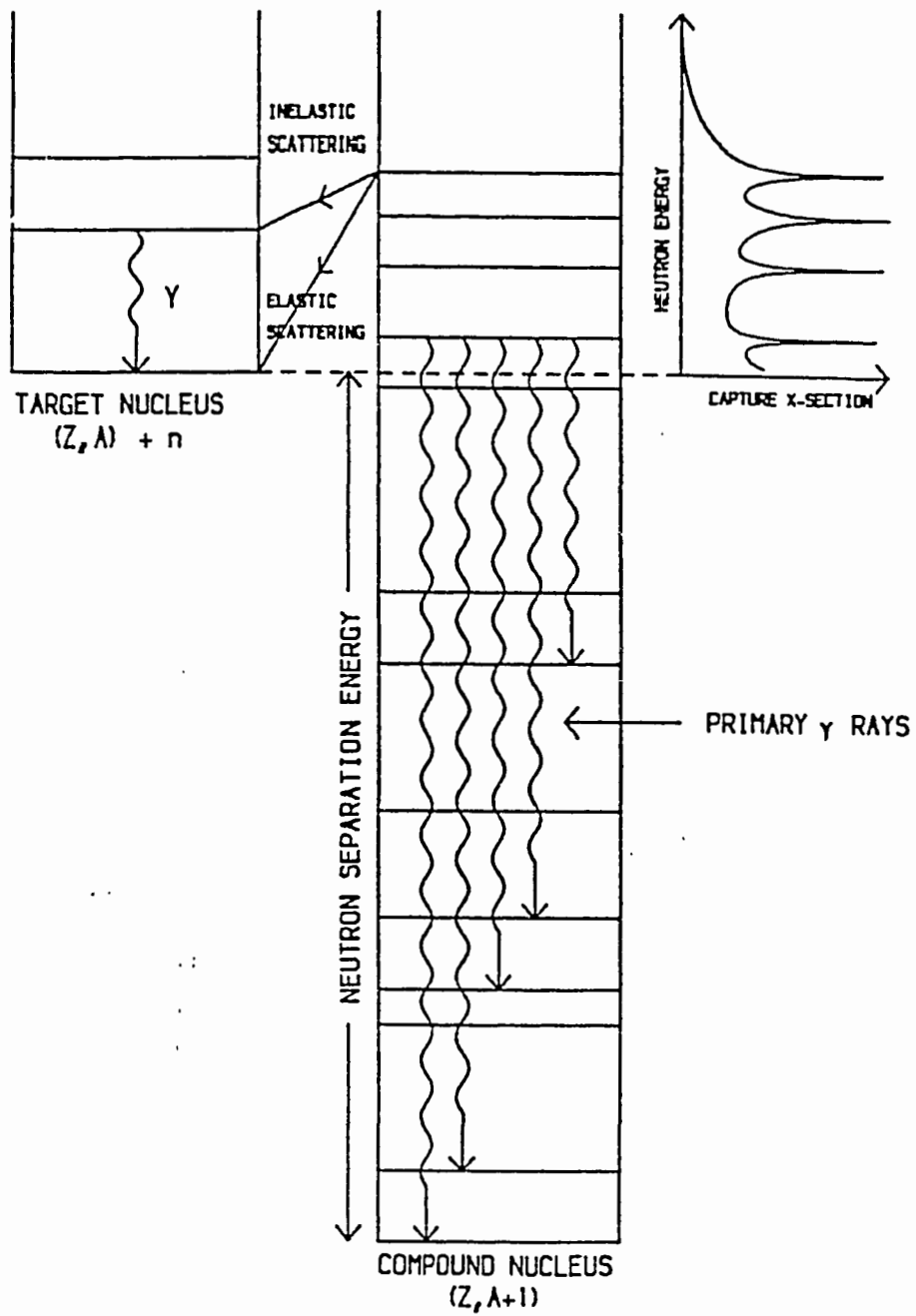


Fig. 1.2. Neutron capture level scheme. Inelastic scattering is possible only when the incident neutron energy is above threshold. Possible primary gamma-rays from a particular resonance are indicated.

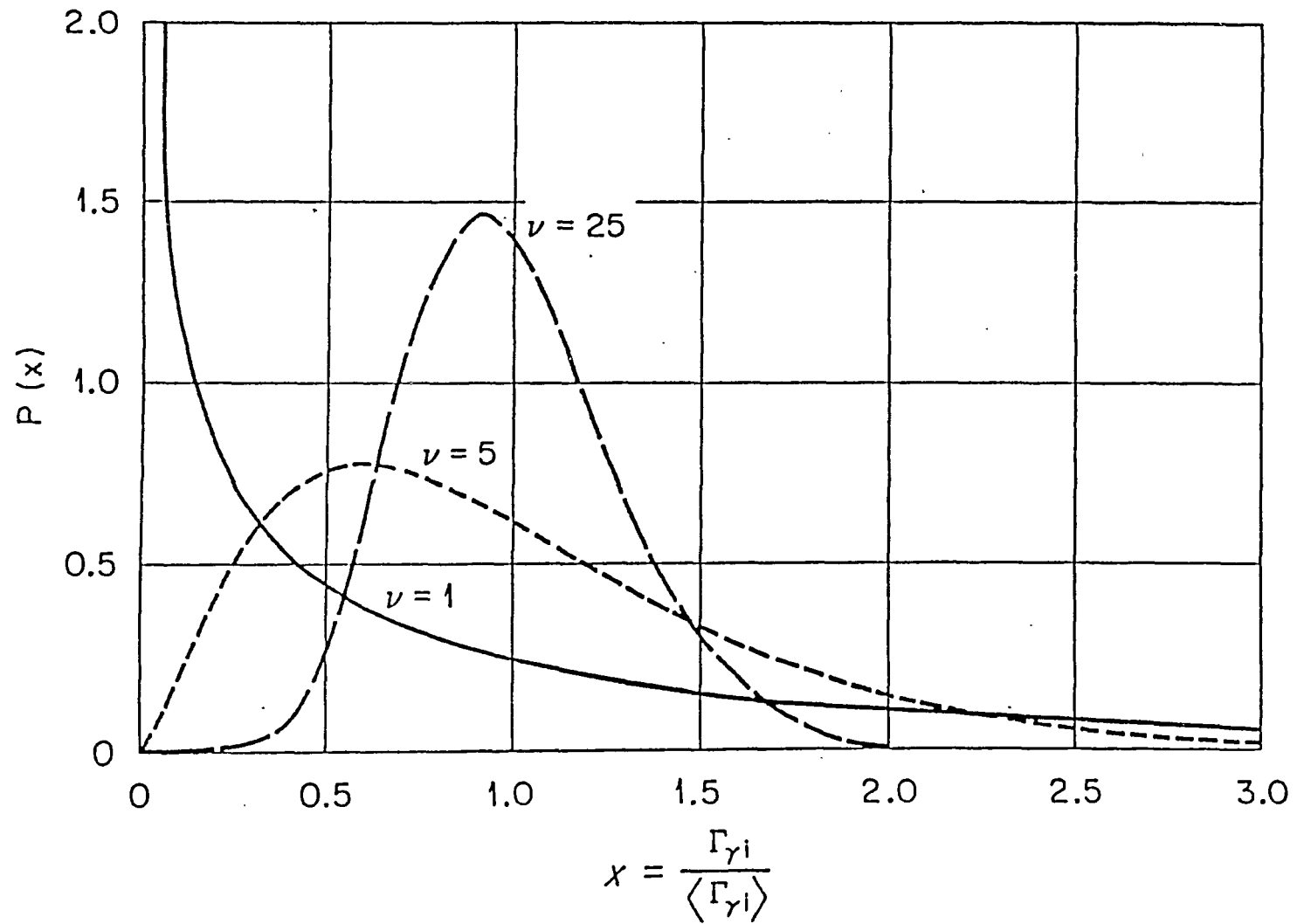


Fig. 1.3. χ^2 distributions with 1, 5 and 25 degrees of freedom.

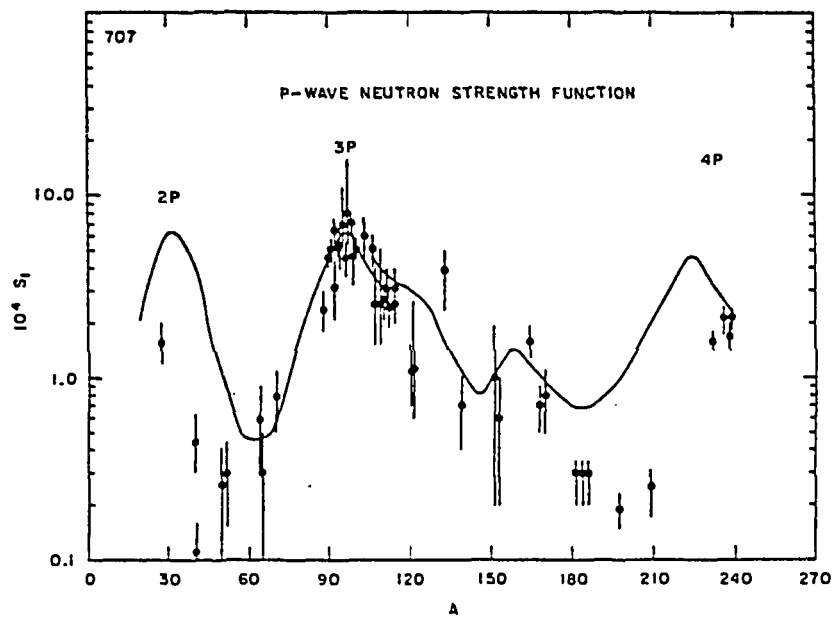
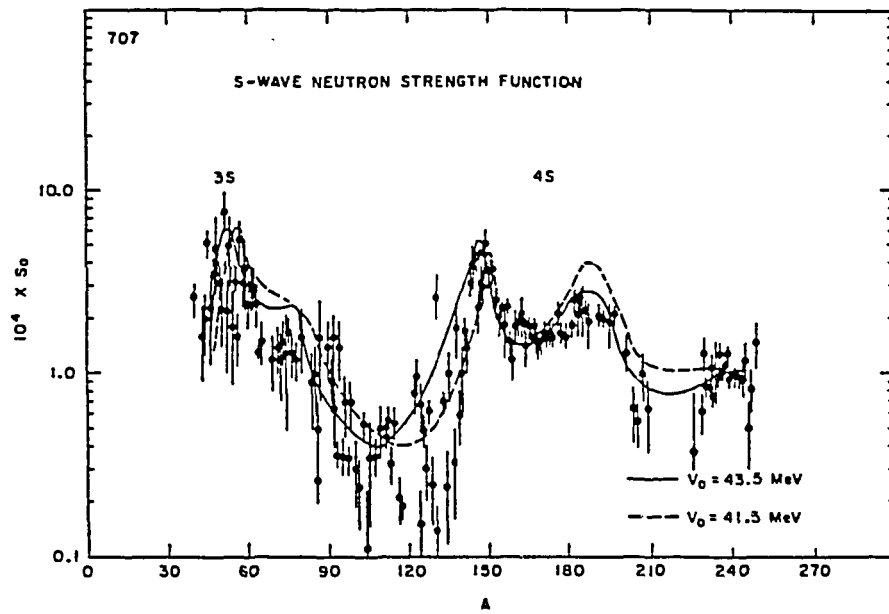


Fig. 1.4. Neutron strength functions plotted against mass number. The curves are optical model fits to the data.

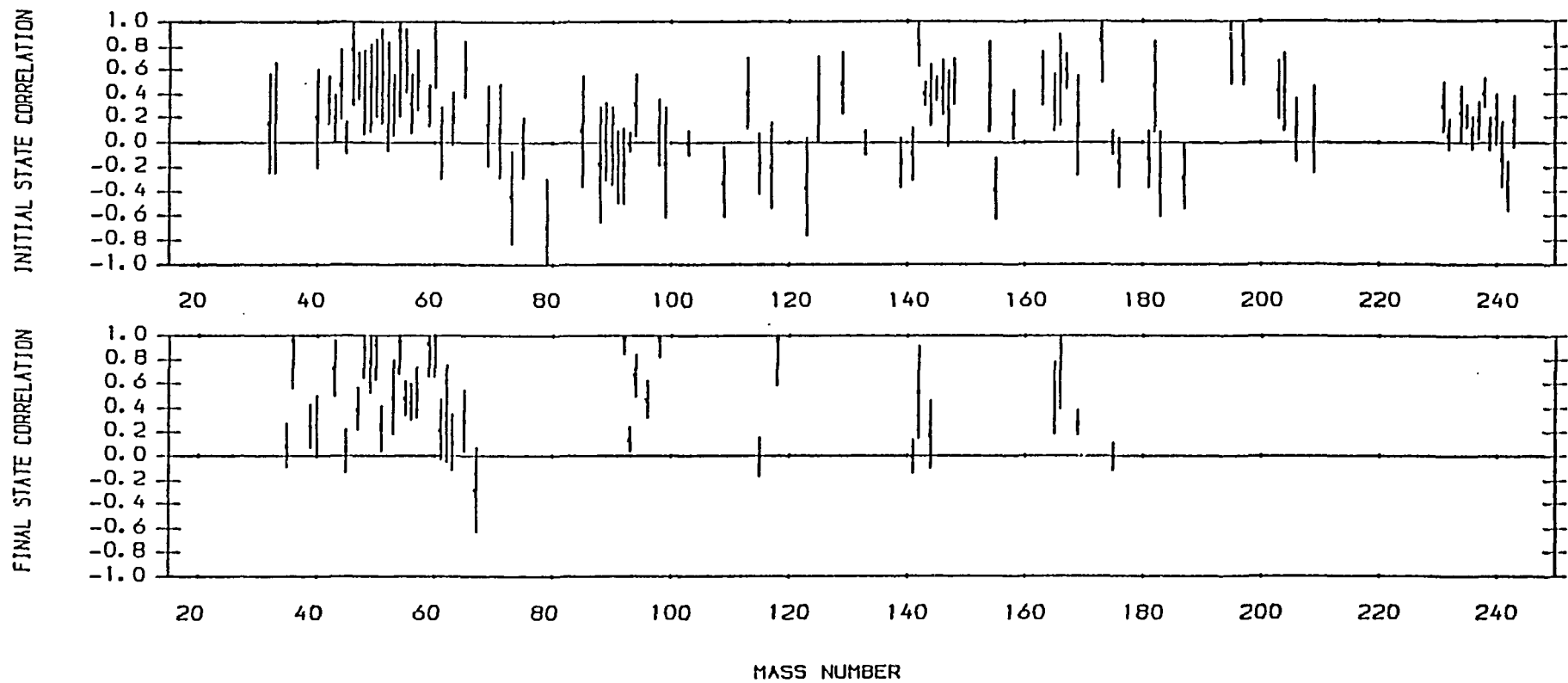
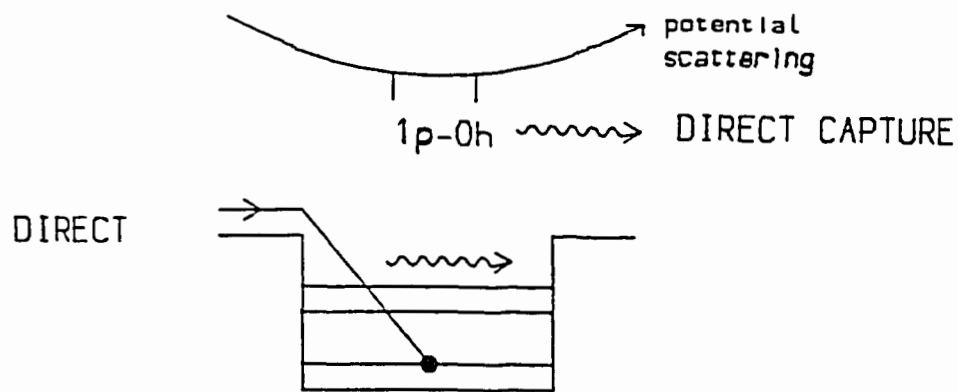


Fig. 1.5. Initial and final state correlations for s -wave resonances plotted as a function of mass number. Initial state correlations are between the reduced neutron width and the total radiative width. Final state correlations are between the reduced partial radiative width and the spectroscopic factor of the final state.

(a) NON-RESONANT CAPTURE



(b) RESONANT CAPTURE

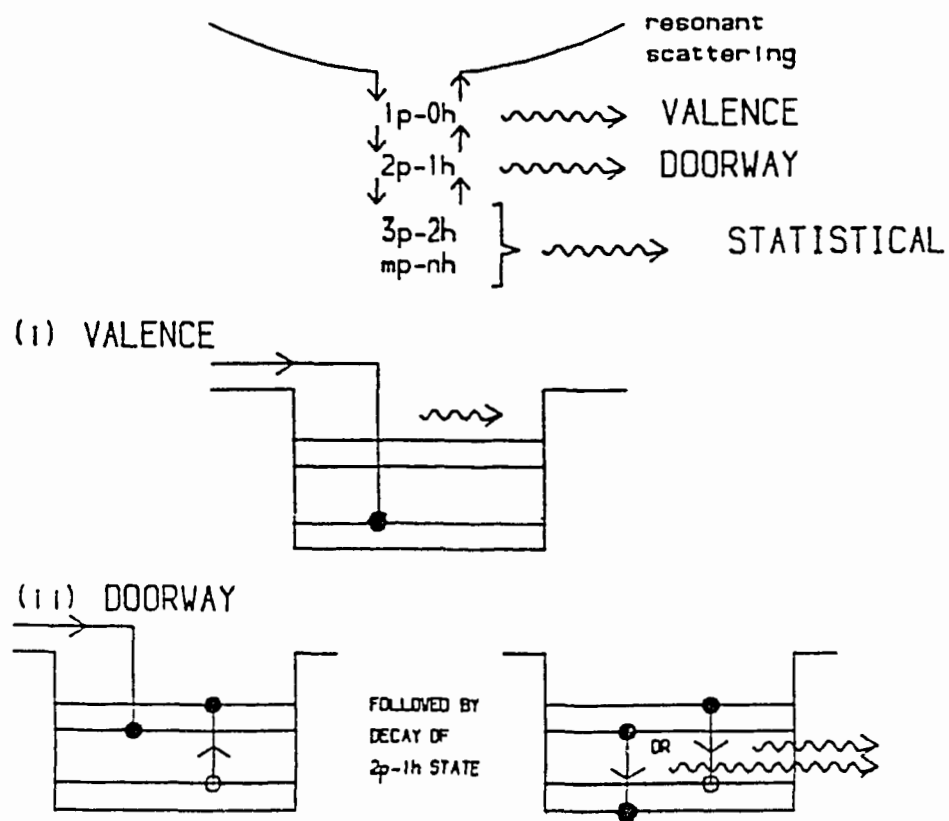


Fig. 1.6. Schematic representations of the various neutron capture mechanisms. The direct capture occurs without formation of a compound nucleus. Valence and doorway capture occur when the $1p-0h$ and $2p-1h$ configurations respectively dominate decay of the compound nucleus.

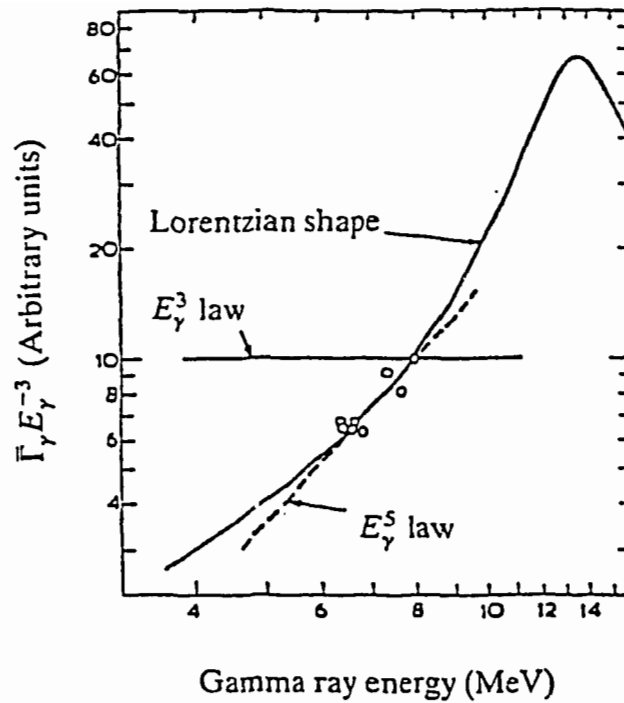


Fig. 2.1. The energy dependence of reduced partial radiation widths in ^{196}Pt . The E_γ^5 rule is seen to be a valid form for the extrapolation of a Lorentzian in the region of the neutron separation energy. The experimental data (BT 67) are for resonance-averaged gamma-ray transitions and are clearly consistent with the predictions of extrapolating the giant dipole resonance. The strong coupling model would imply an E_γ^3 dependence for which there is no evidence.

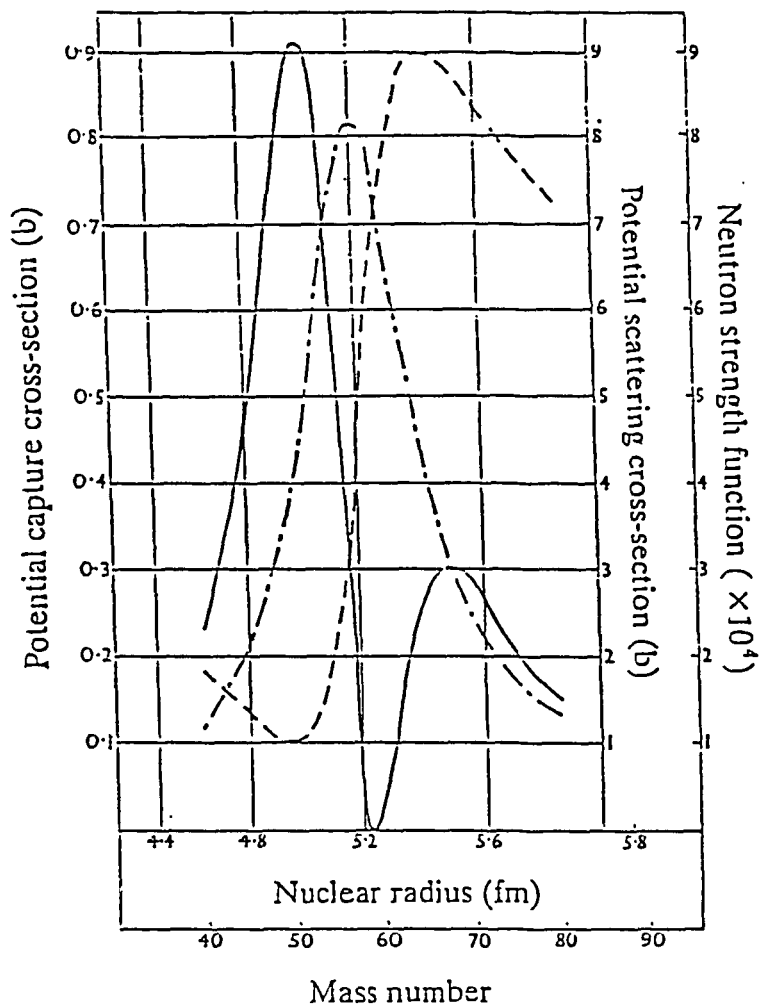


Fig. 2.2. The potential capture cross-section (full curve) calculated in the $3s$ peak of the neutron strength function under the intermediate coupling assumption (LL 60). Also shown are the potential scattering cross-section (---) and the neutron strength function (----).

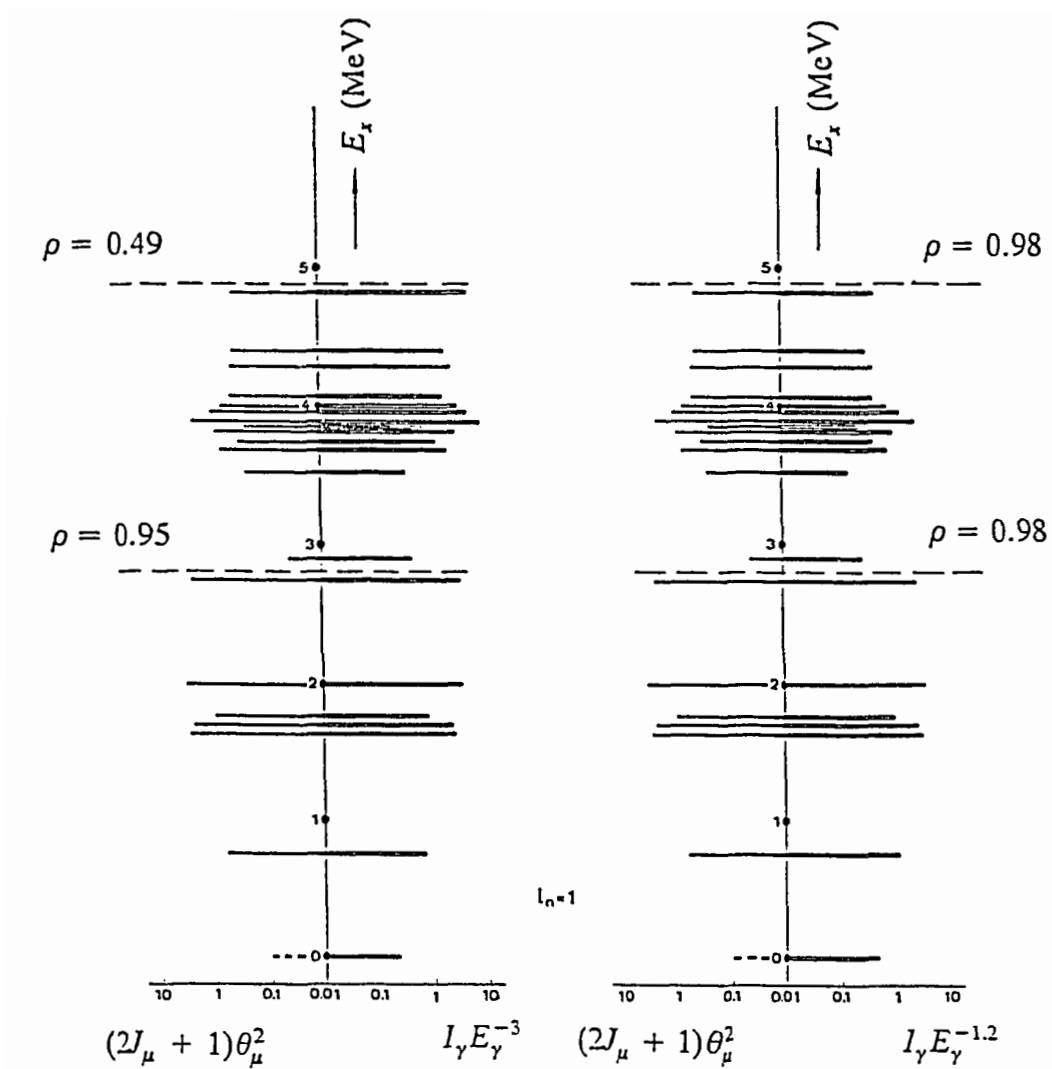


Fig. 2.3. Comparison of the stripping strengths, $(2J_\mu + 1)\theta_\mu^2$ of the (d,p) reaction with the reduced transition strengths from thermal neutron capture in ^{37}Cl to levels having $l = 1$ (SA 73). The results for reduction factors of E_γ^3 and $E_\gamma^{1.2}$ are shown on the left and right respectively. The correlation coefficients are given in each case when only transitions up to 2.8 MeV are considered as well as the values if all states are included.

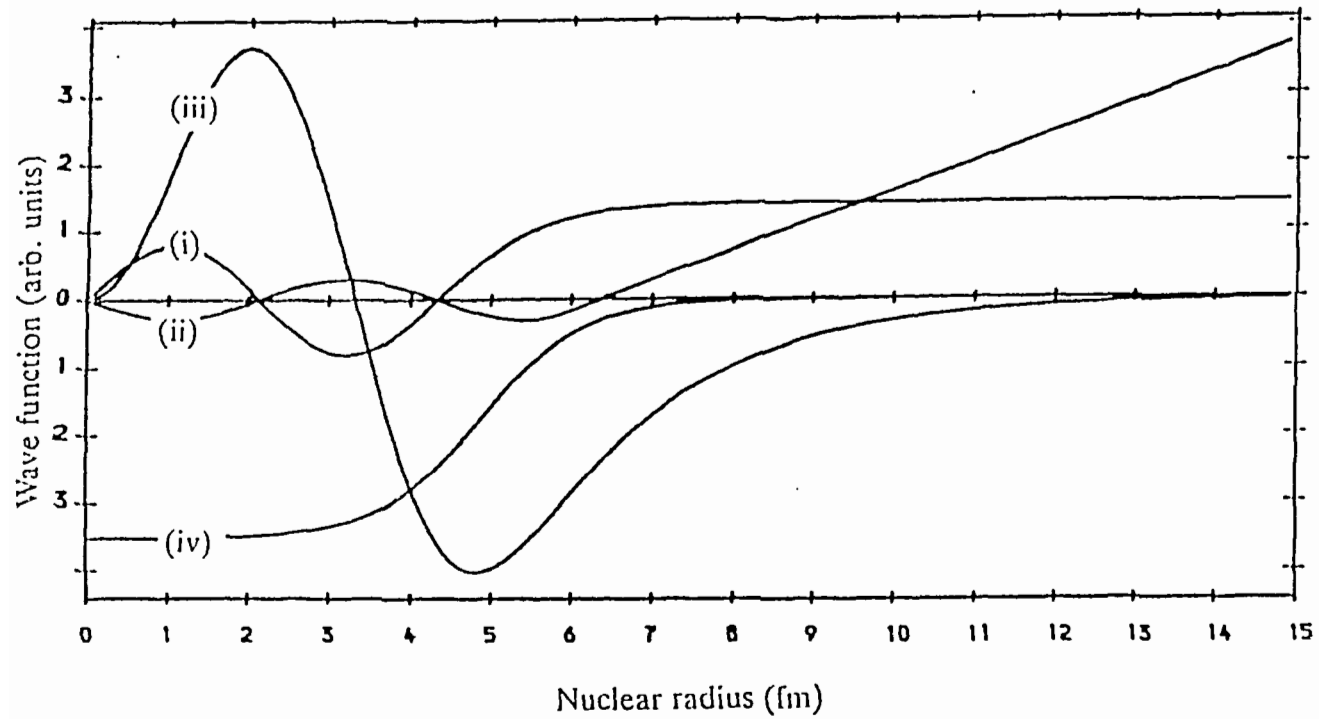


Fig. 2.4. Radial wave functions evaluated in the valence model calculations for $A = 54$. The initial state is unbound with real and imaginary parts to the wave function (curves (i) and (ii) respectively). The final state is bound and the wave function (curve (iii)) is real. Also shown is the real part of the potential (curve (iv)). Optical model parameter values are those of Moldauer (Mol 63).

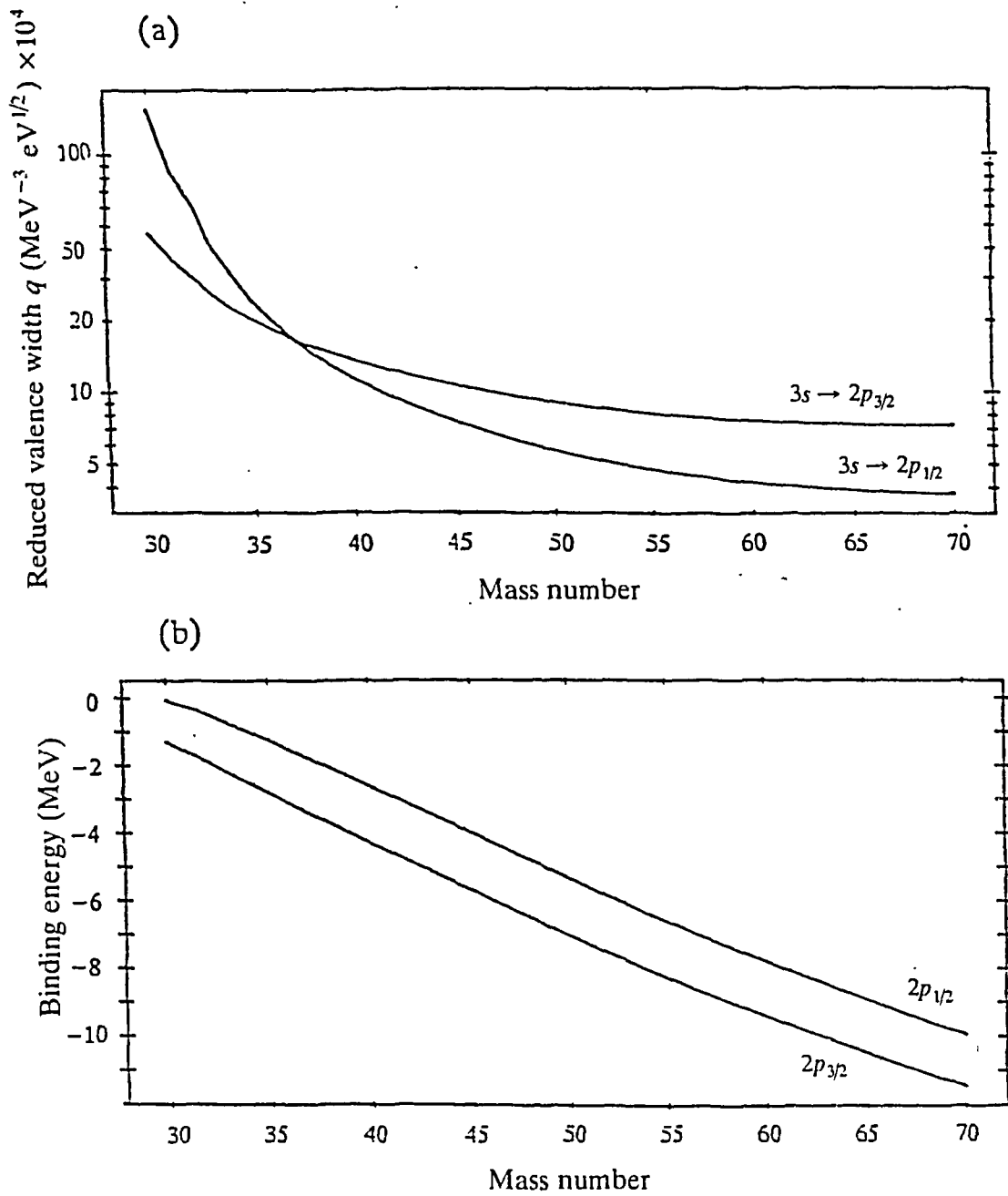


Fig. 2.5. The dependence of (a) the reduced valence width, q , and (b) single particle binding energies on mass number for final $2p_{1/2}$ and $2p_{3/2}$ states. q is evaluated for thermal energy neutrons. Optical model parameter values are those of Moldauer (Mol 63).

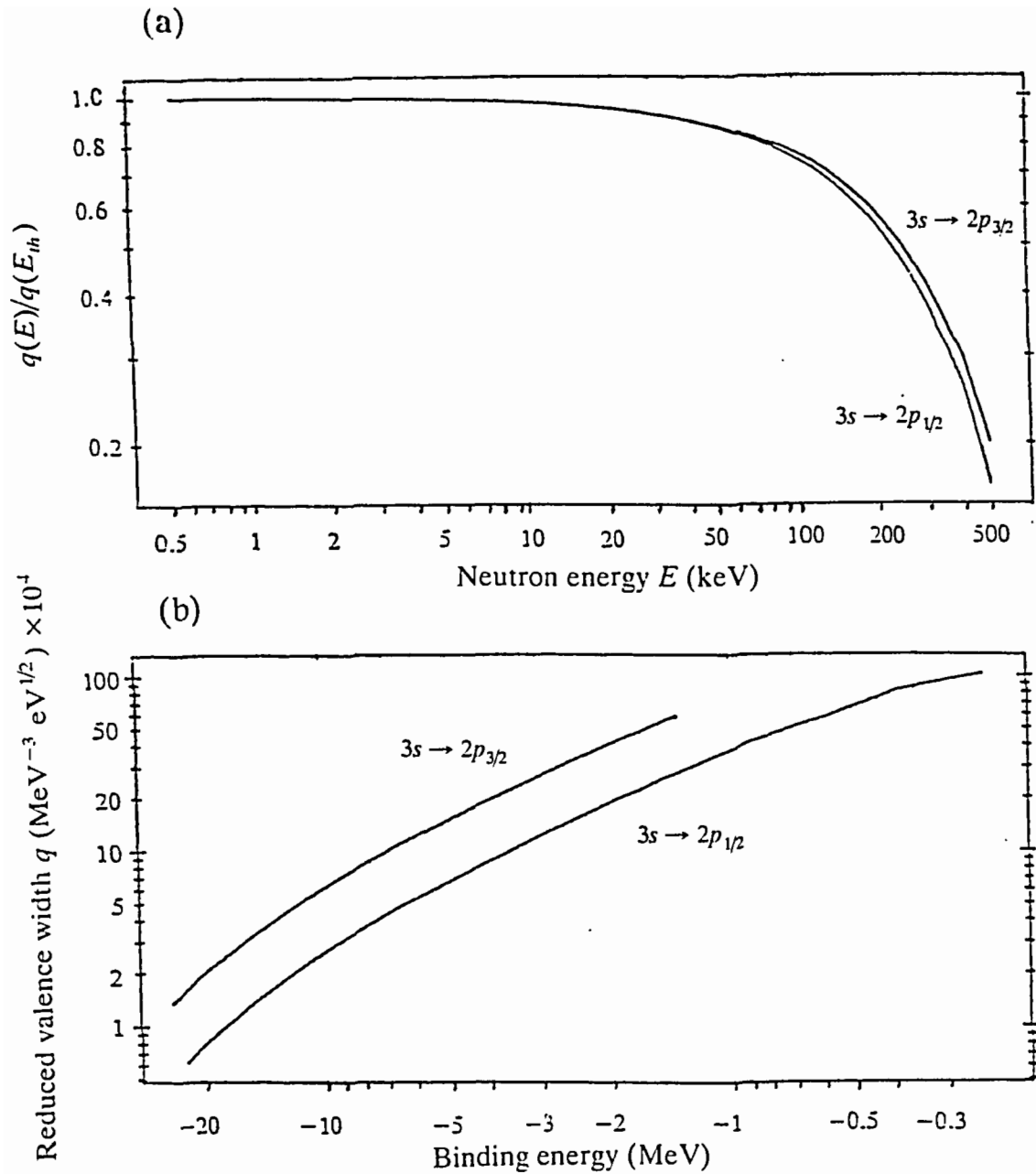


Fig. 2.6. (a) The ratio of the reduced valence width at resonance energy E compared with its value for a resonance at thermal energy. Optical model parameter values are those of Moldauer (Mol 63). (b) The reduced valence width as a function of the binding energy. The initial state is evaluated with the parameters of Moldauer whilst the final state well depth is varied to produce different binding energies (B.E.). Over the range of interest, the behaviour is well represented by $q \propto (B.E.)^{-1}$ for final state $2p_{1/2}$ and $2p_{3/2}$.

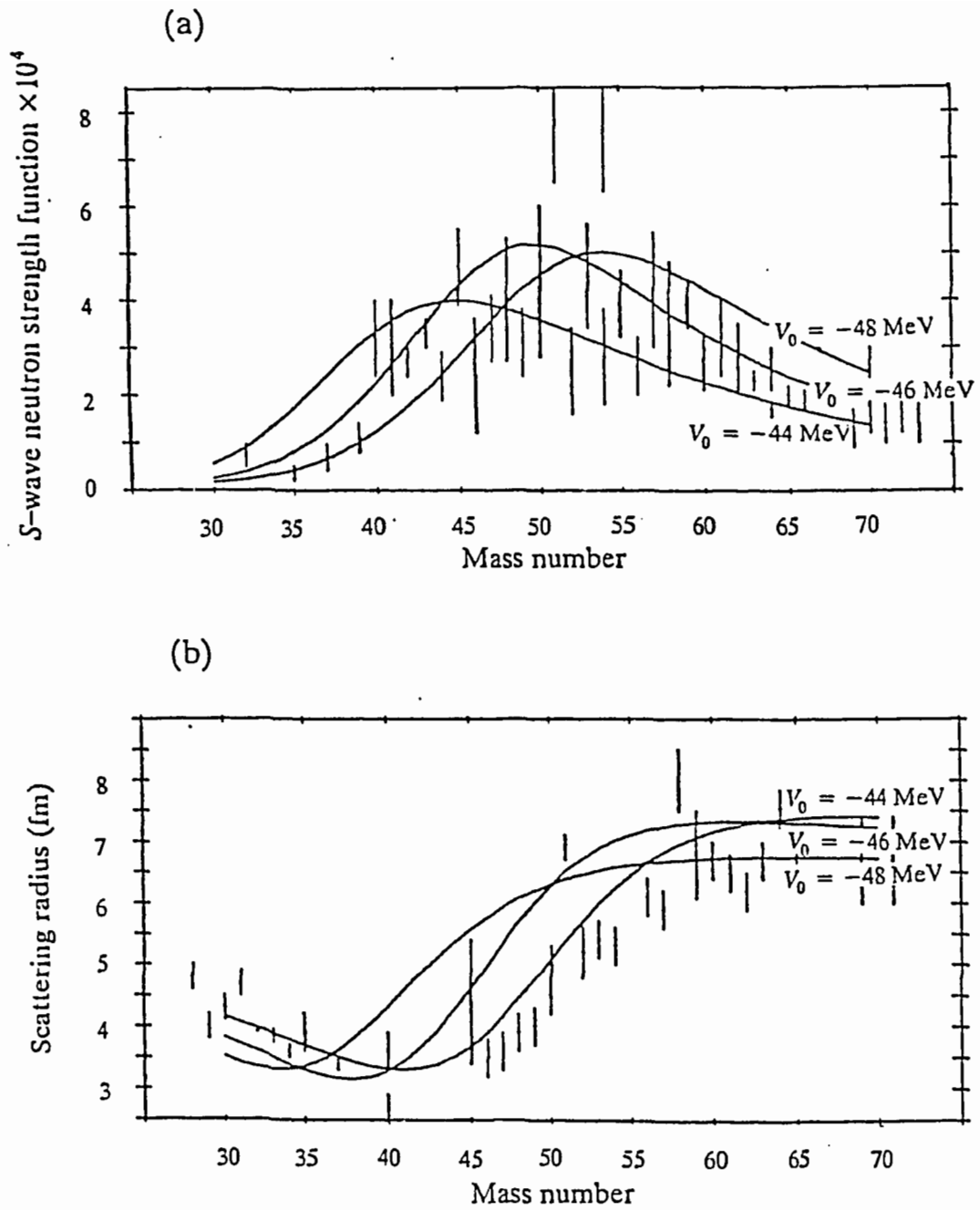


Fig. 2.7. Comparison of optical model predictions for (a) the s -wave neutron strength function and (b) the scattering radius for various values of V_0 with other parameters fixed at the values given by Moldauer (Mol 63). The experimental data are taken from (Mug + 81).

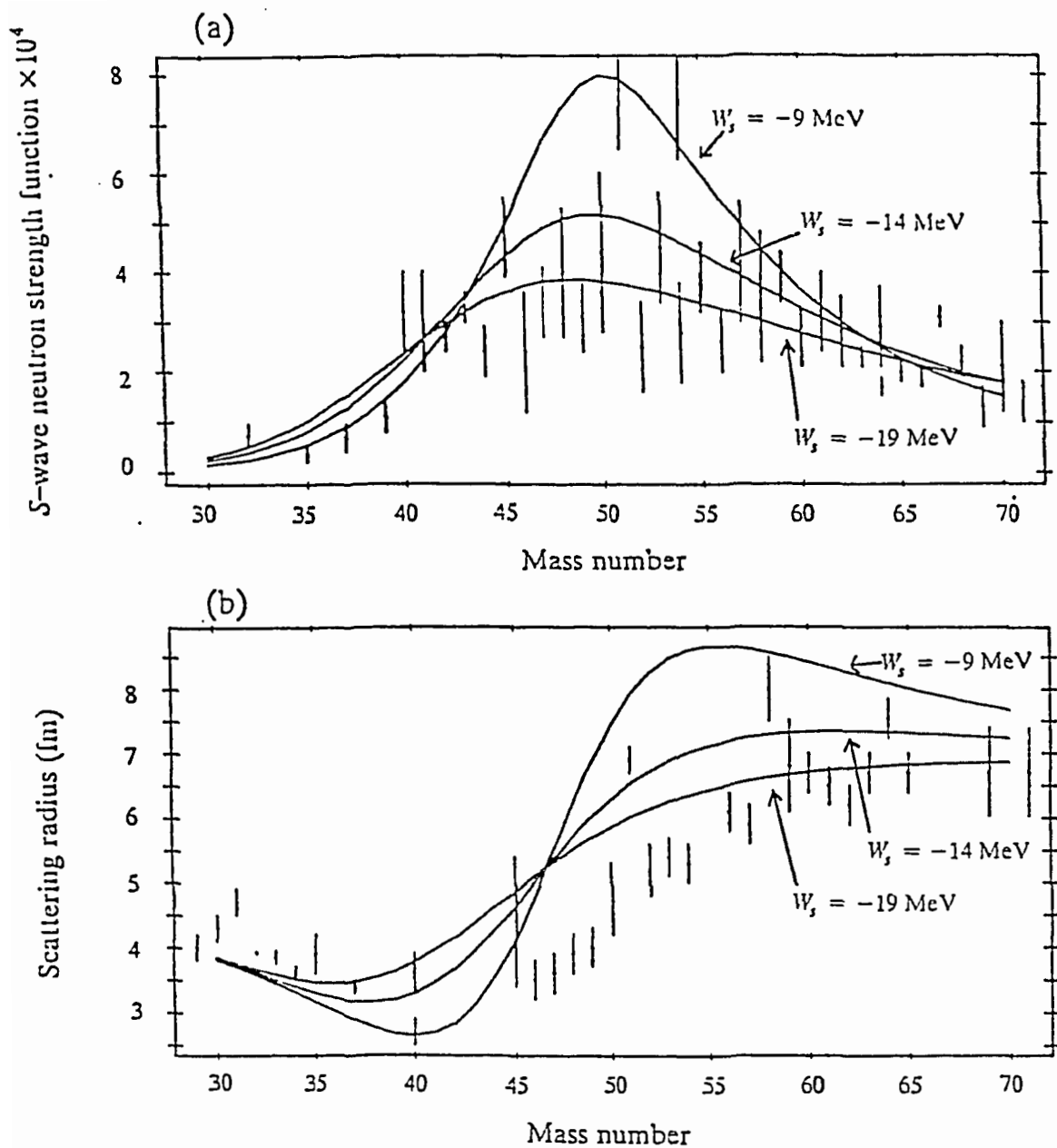


Fig. 2.8. Comparison of optical model predictions for (a) the *s*-wave neutron strength function and (b) the scattering radius for various values of W_s with other parameters fixed at the values given by Moldauer (Mol 63). The experimental data are taken from (Mug + 81).

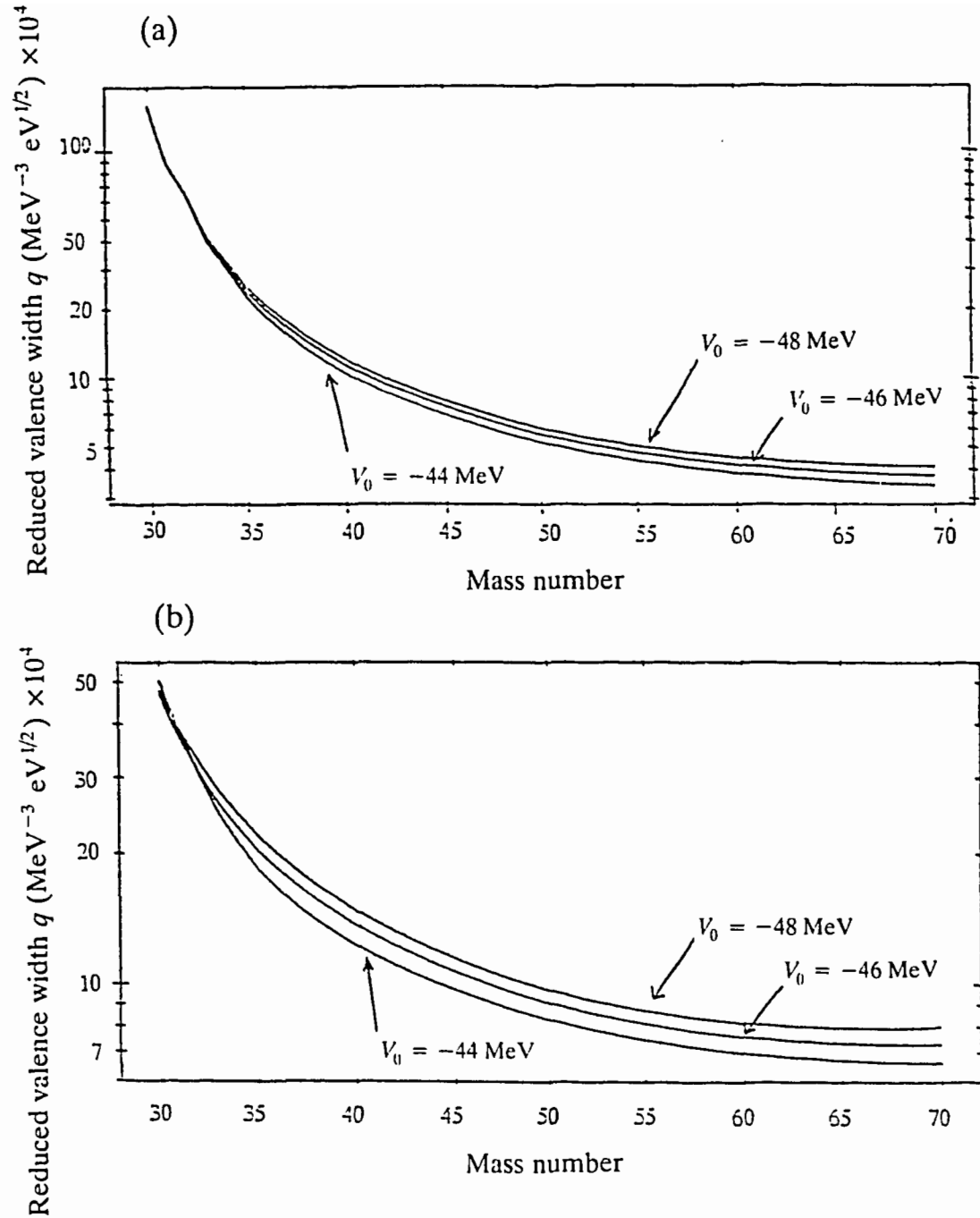


Fig. 2.9. The behaviour of the reduced valence width for different values of the depth of the real part of the optical potential with other parameters fixed at the values given by Moldauer (Mol 63). The final state potential remains fixed as the real part of the Moldauer potential. (a) is for transitions $3s \rightarrow 2p_{1/2}$ and (b) is for transitions $3s \rightarrow 2p_{3/2}$.

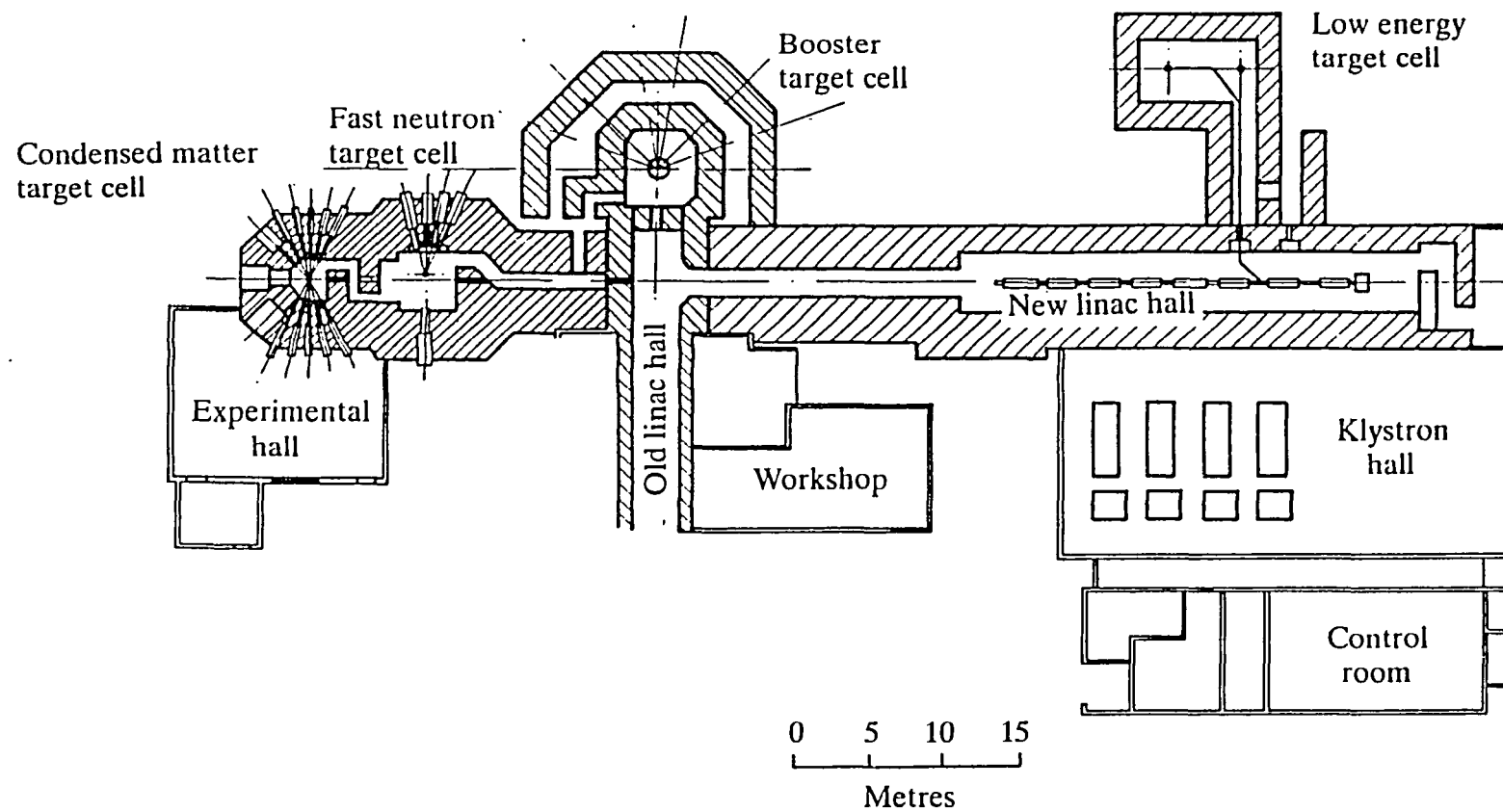
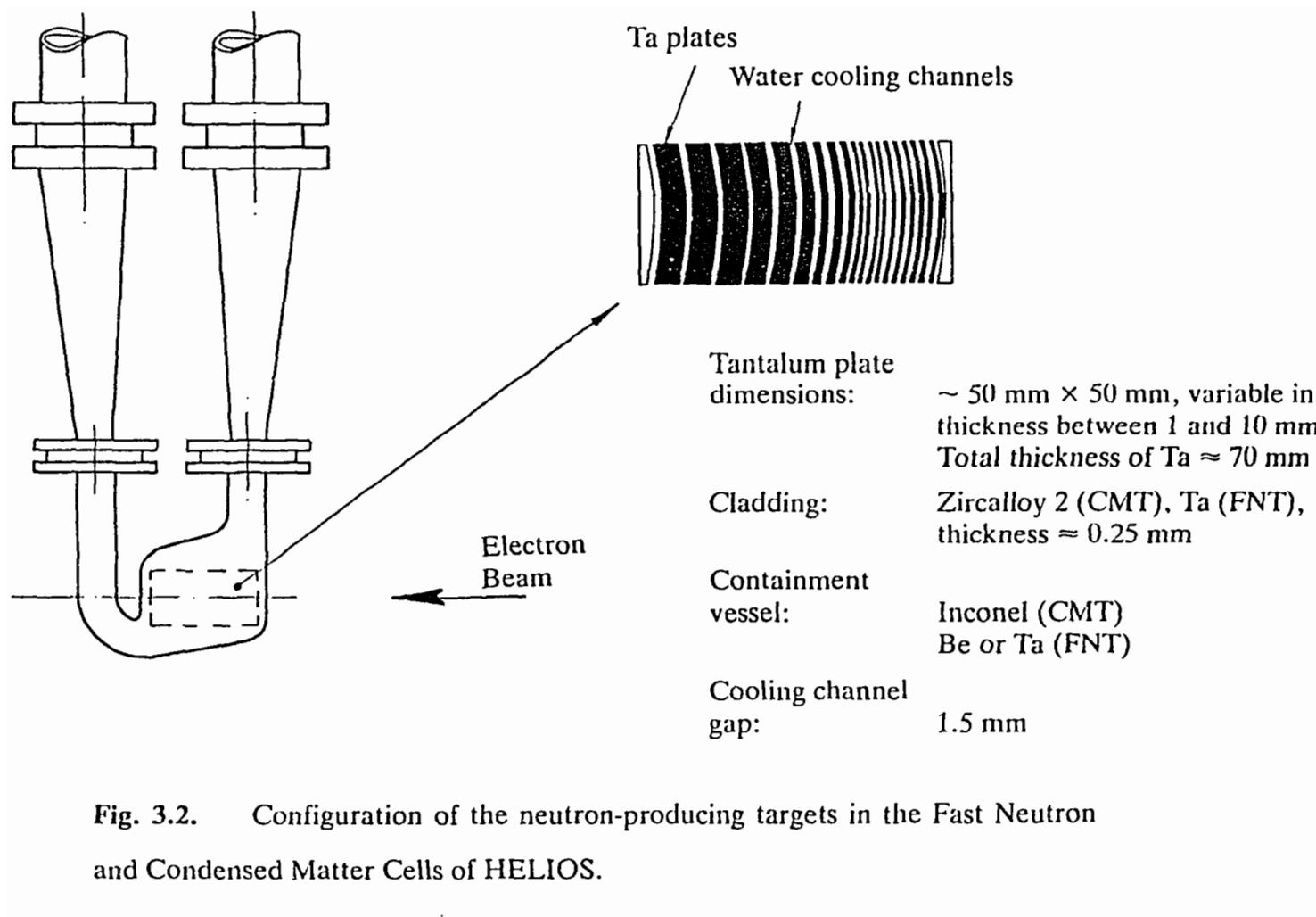


Fig. 3.1. General plan of the Harwell 136 MeV electron linac HELIOS.



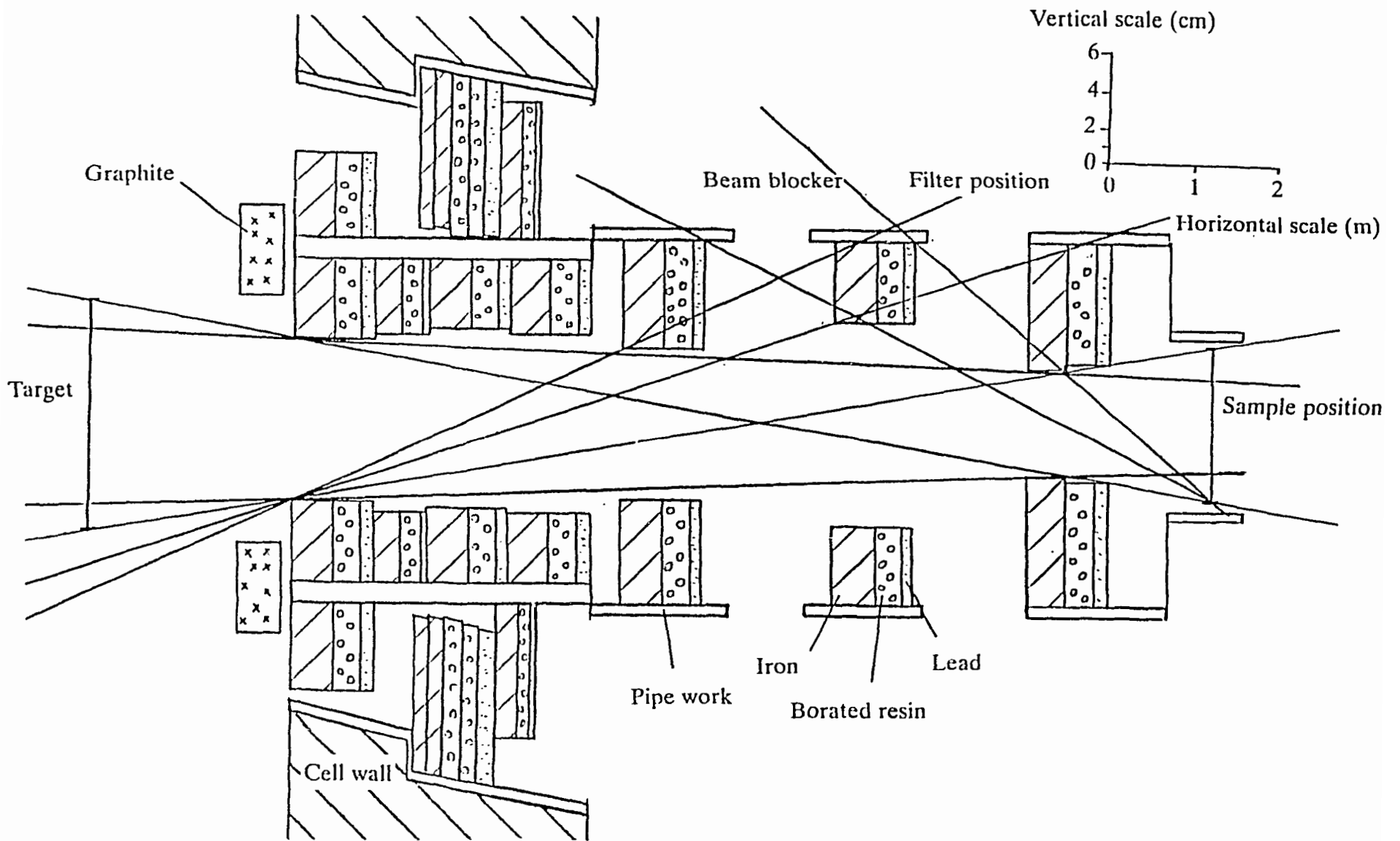


Fig. 3.3. Plan view of the collimation of the F2 flight path on the FNT of HELIOS.

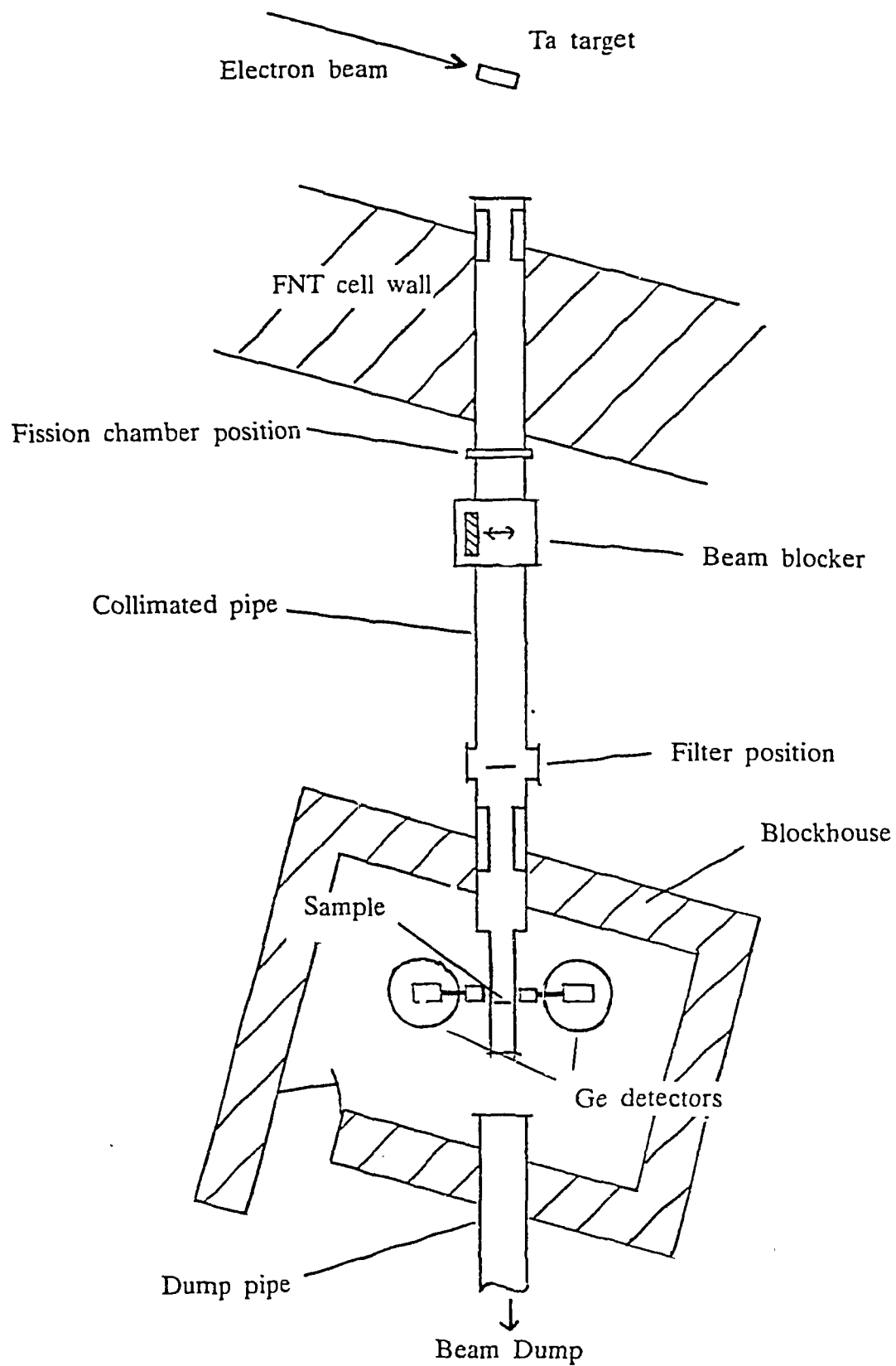


Fig. 3.4. Schematic representation of the various components of flight path F2 on the FNT of HELIOS.

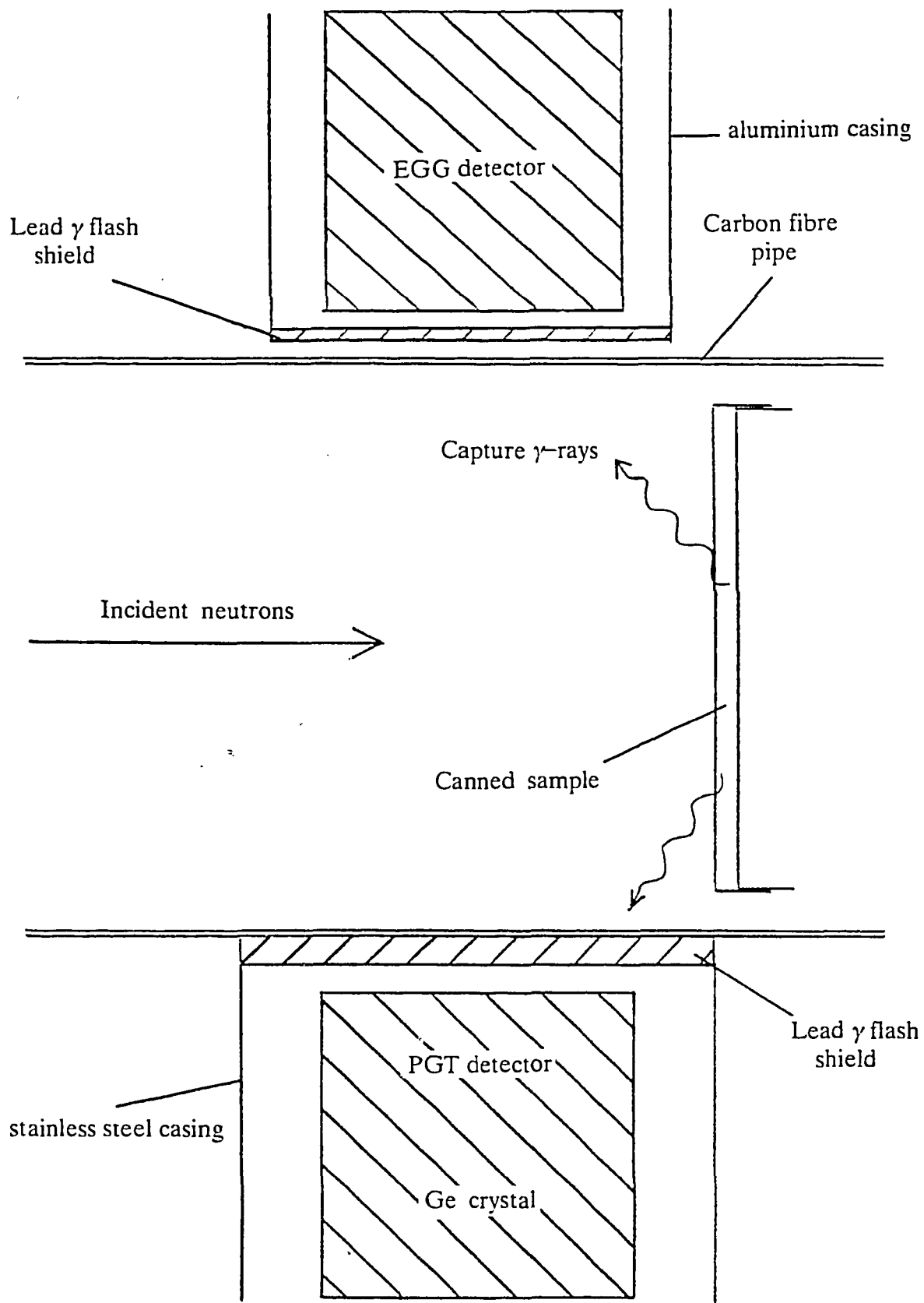


Fig. 3.5. The chosen geometry of the sample-detector arrangement for capture gamma-ray spectrum measurements on flight path F2

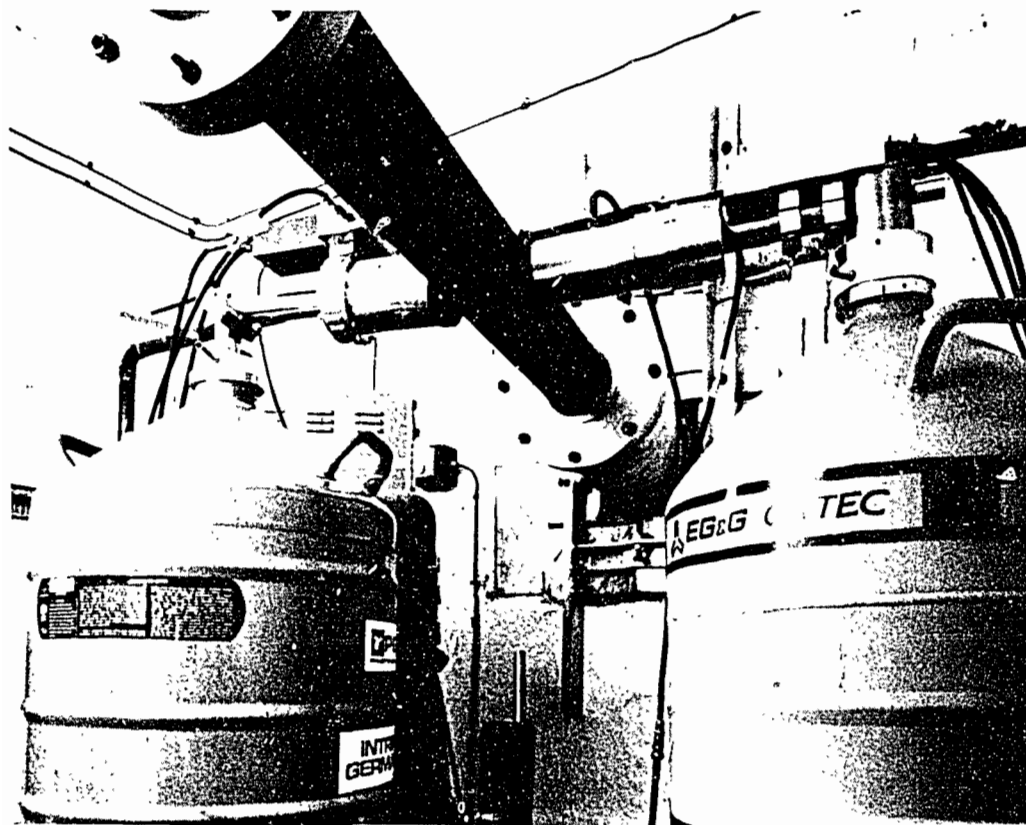
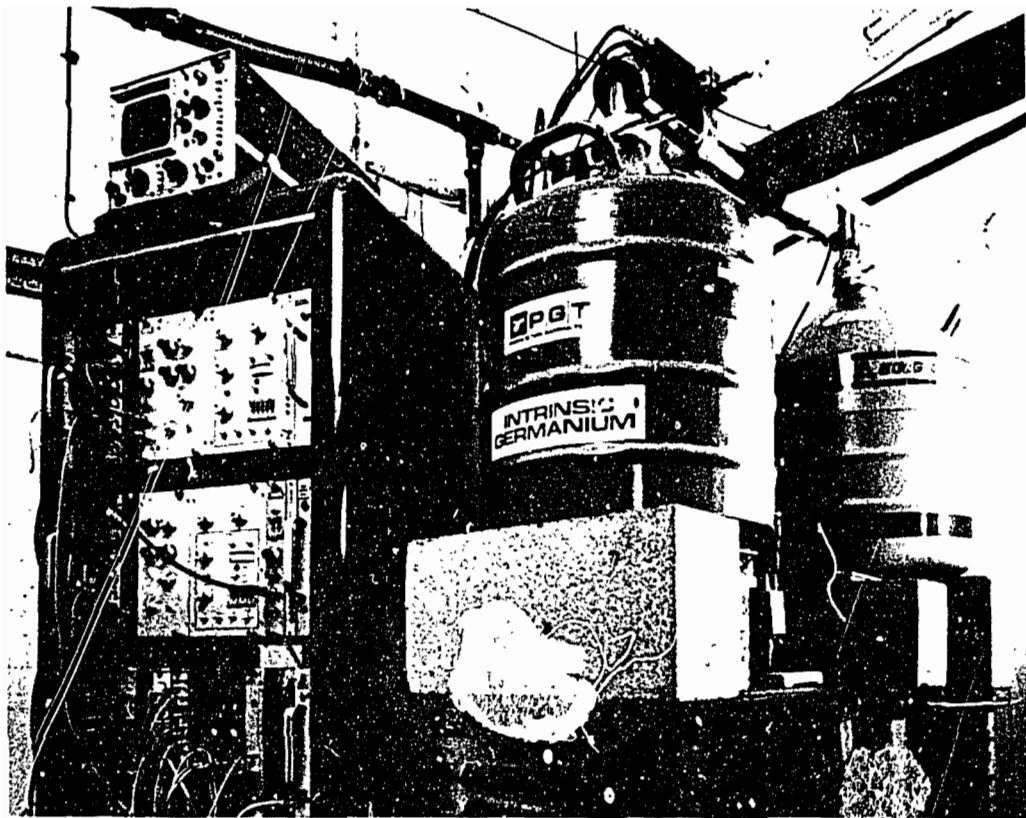


Fig. 3.6. The electronics and experimental set up in the F2 blockhouse (top) and a close-up of the detector arrangement (bottom).

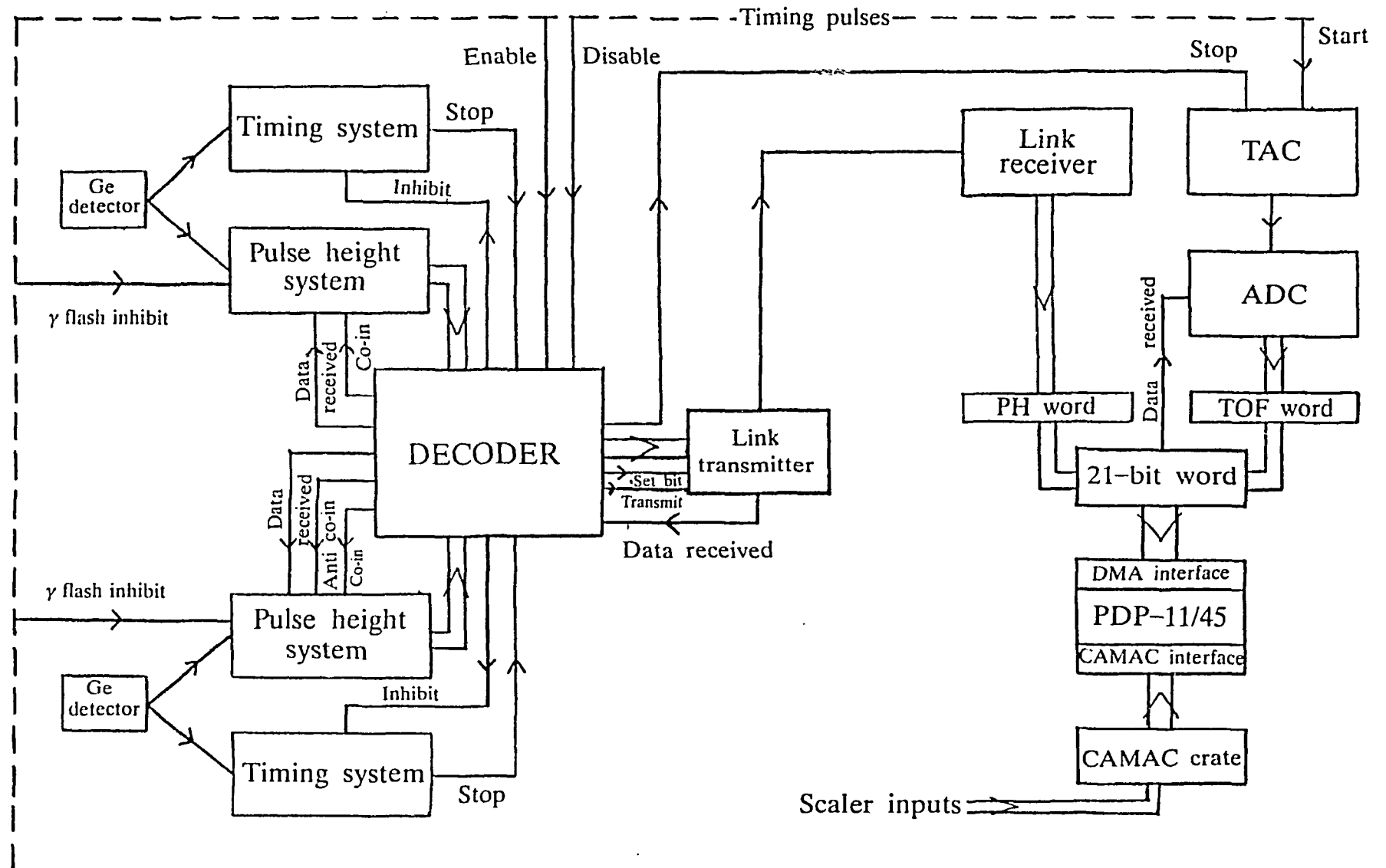


Fig. 3.7. Block diagram of the detector and data collection electronics.

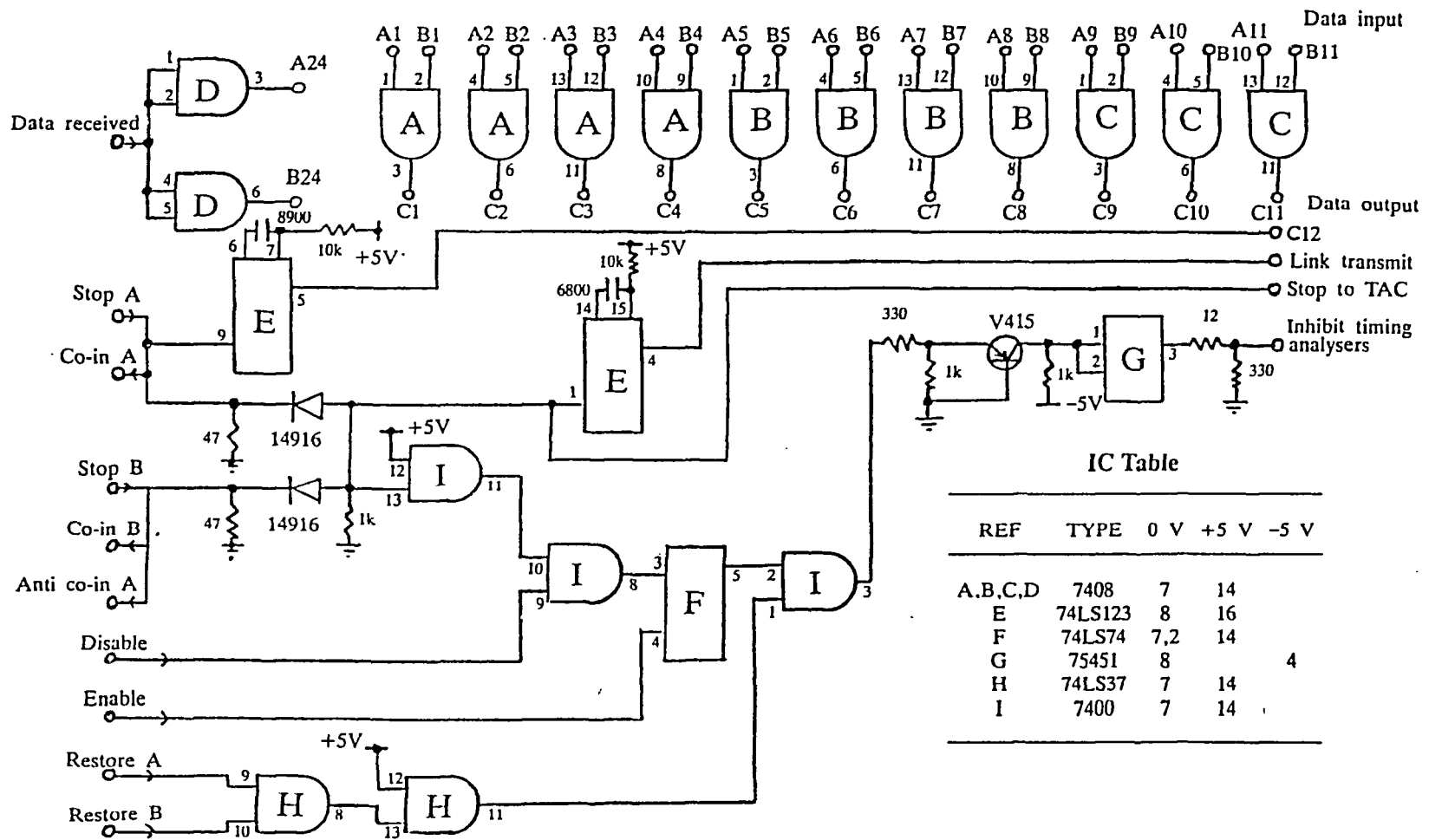


Fig. 3.8. Circuit diagram of the electronics unit DECODER which combines the outputs of the two detectors, A and B, and arranges for the data to be transmitted to the data acquisition computer.

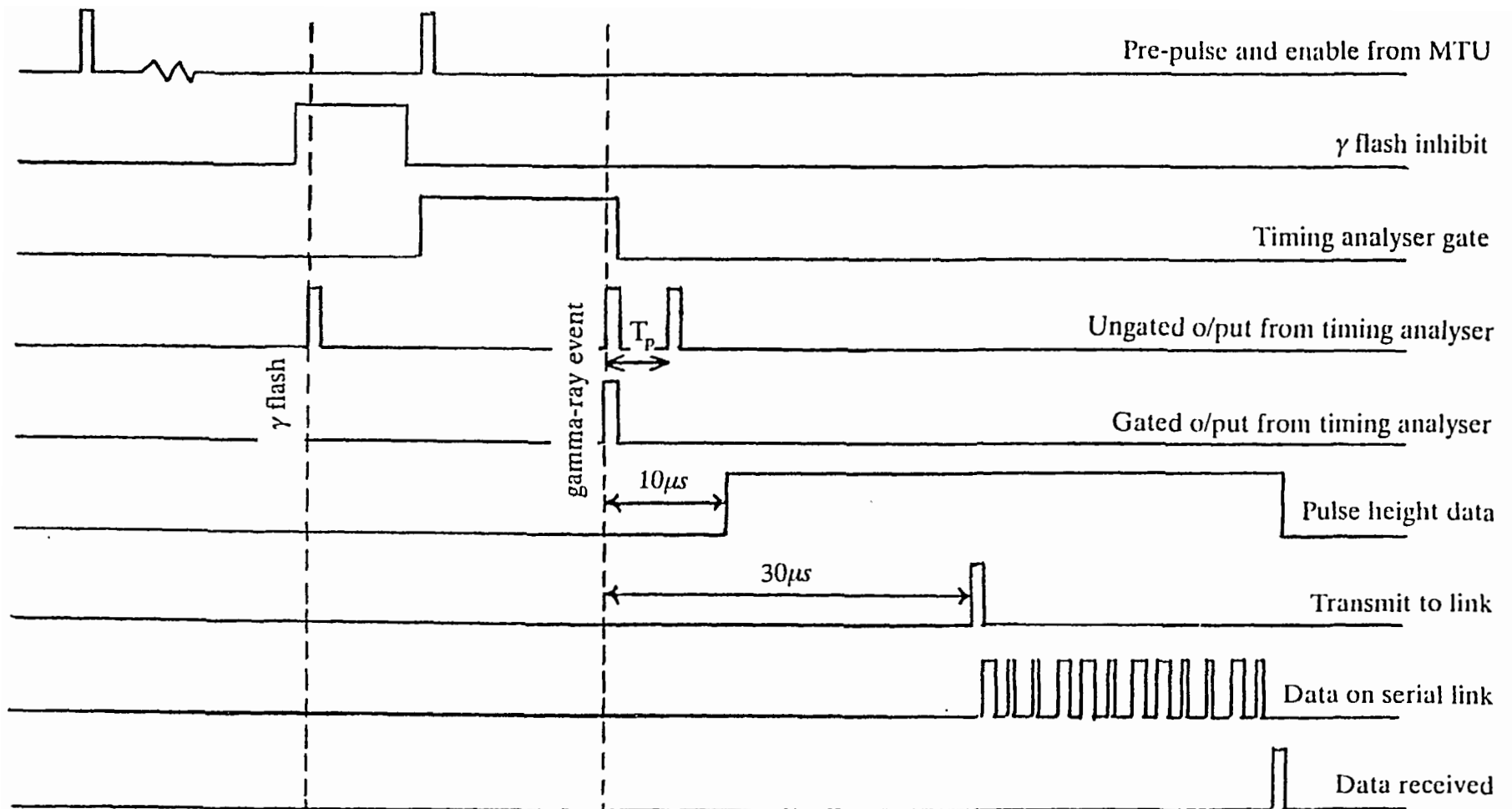


Fig. 3.9. Timing diagram for one machine cycle in which a gamma-ray event is detected. (T_p is the pulse processing period.)

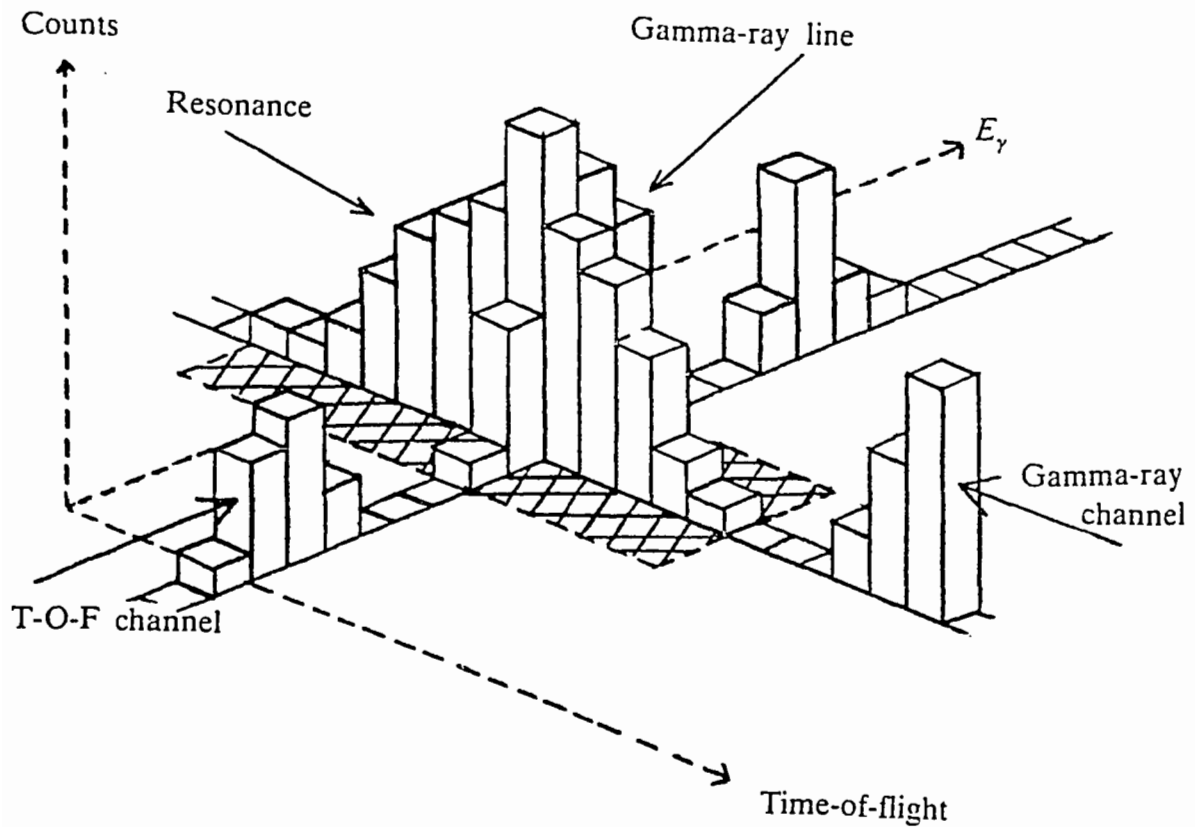


Fig. 4.1. Schematic representation of a portion of the 2-D histogram obtained in a resonance capture gamma-ray experiment. The volume under a particular peak can be summed over the area of integration (shown hatched), by producing the gamma-ray spectrum for the resonance of interest, or alternatively, the time-of-flight spectrum for the gamma-ray of interest, and then evaluating the appropriate area.

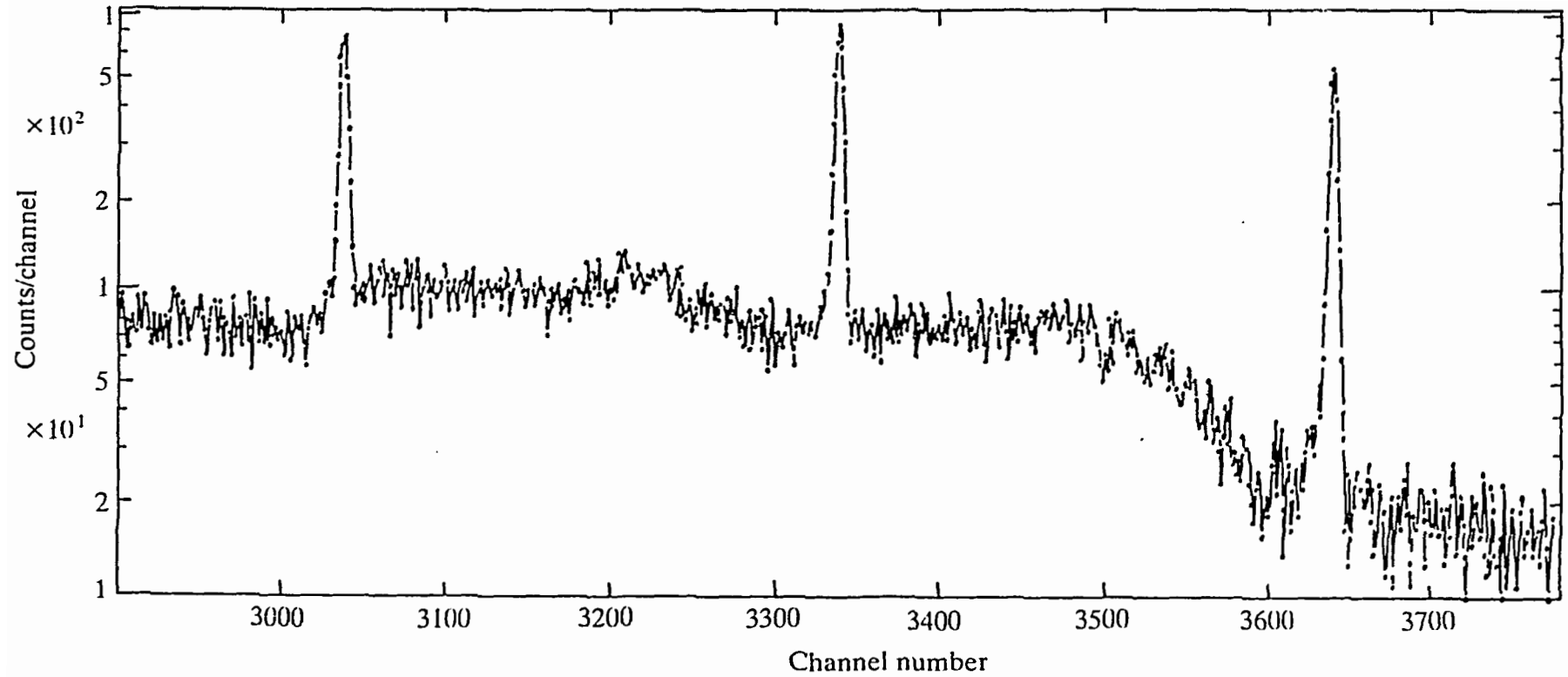


Fig. 4.2. The high energy portion of the pulse height spectrum produced by a Ge detector exposed to a monoenergetic source of 6130 keV gamma-rays. The full energy, single escape and double escape peaks (channels 3620, 3320 and 3020 respectively), plus a continuum due to Compton processes can be seen, on top of a small background due to natural radiation in the surroundings.

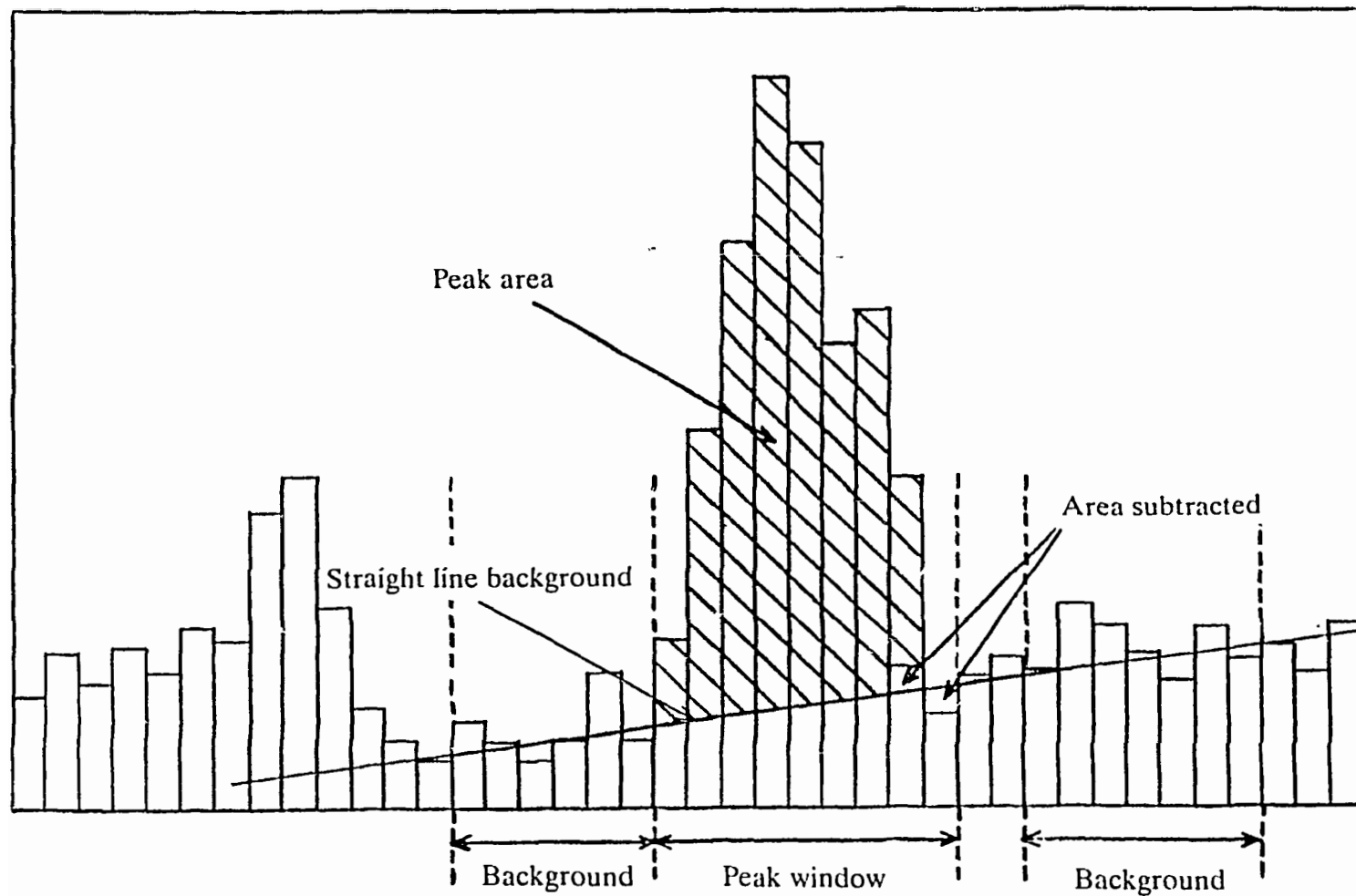


Fig. 4.3. Calculation of the peak area by assuming the background to be represented by a straight line fitted through two appropriate windows determined by eye. The net peak area is the shaded region and is the total area above the background line within the peak window.

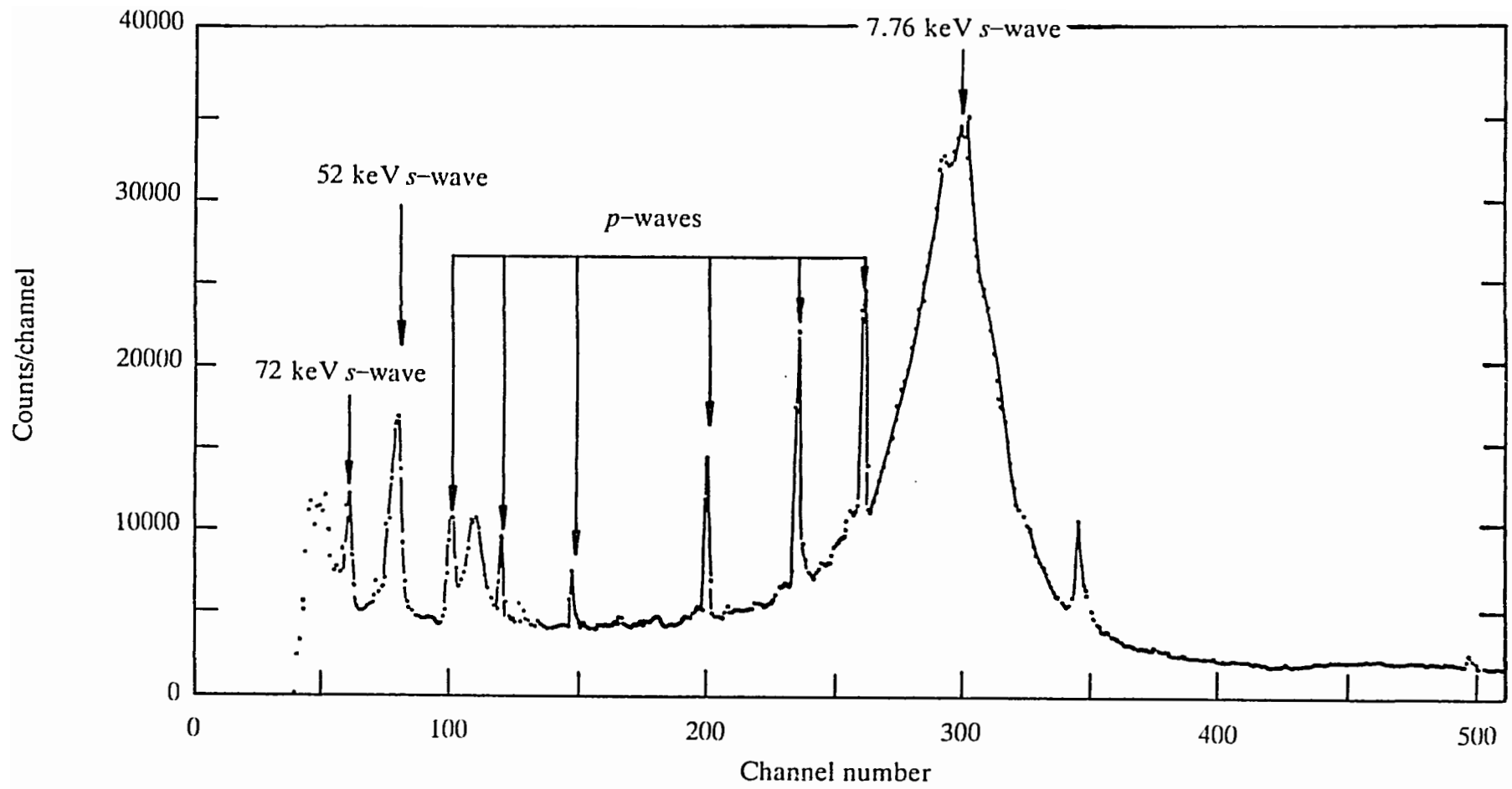


Fig. 4.4. The time-of-flight spectrum for all capture events in ^{54}Fe for which the gamma-ray energy was > 2.5 MeV. Individual resonances have been marked. The peaks at channels 110 and 340 are due to the Al canning of the sample.

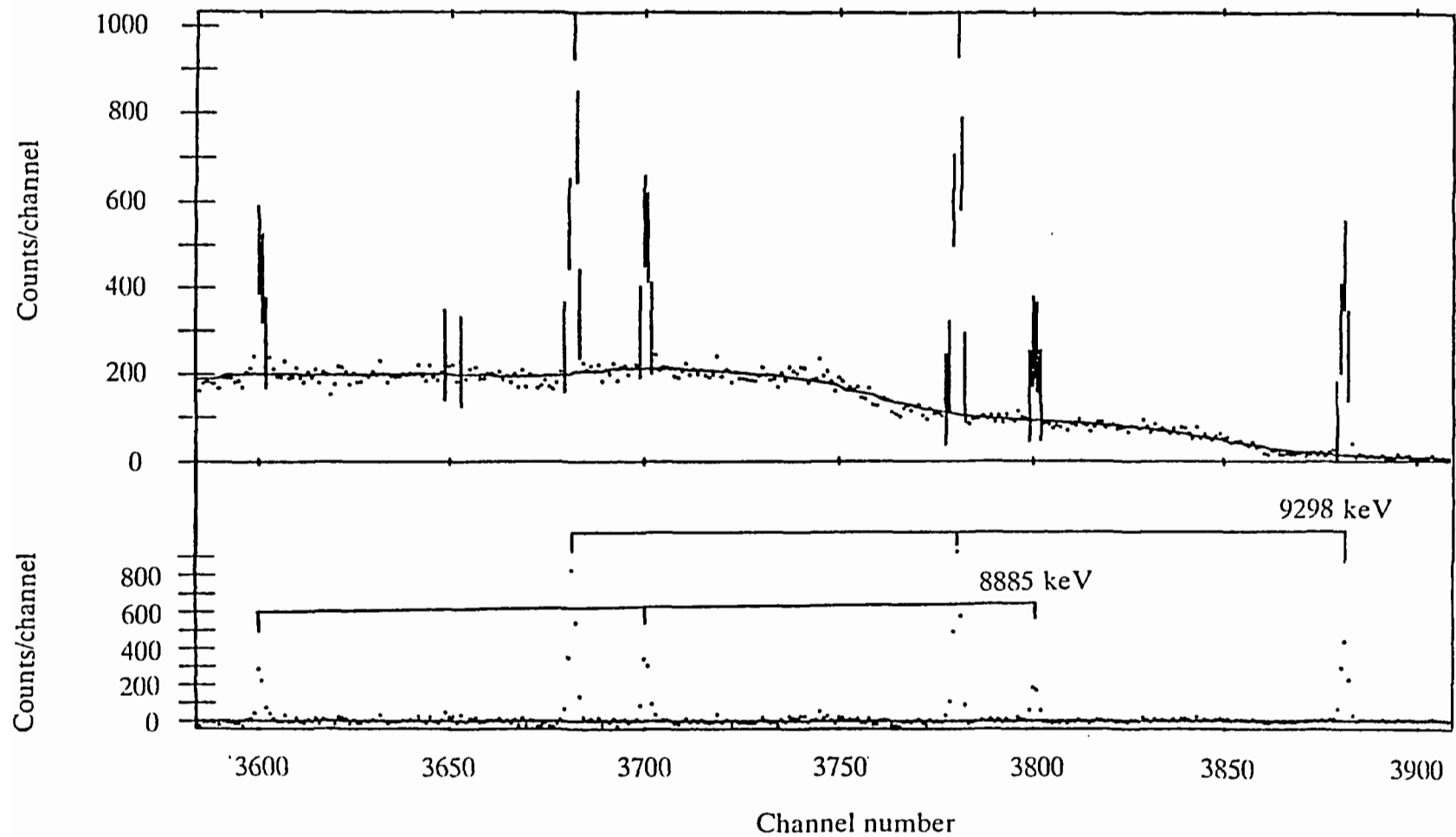


Fig. 4.5. The high energy region of the capture gamma-ray spectrum (top) observed in the 7.76 keV ^{54}Fe s -wave resonance together with the calculated background. The points with lines through them are those rejected in the background determination as belonging to peaks. The bottom graph shows the gamma-ray lines once the background has been subtracted.

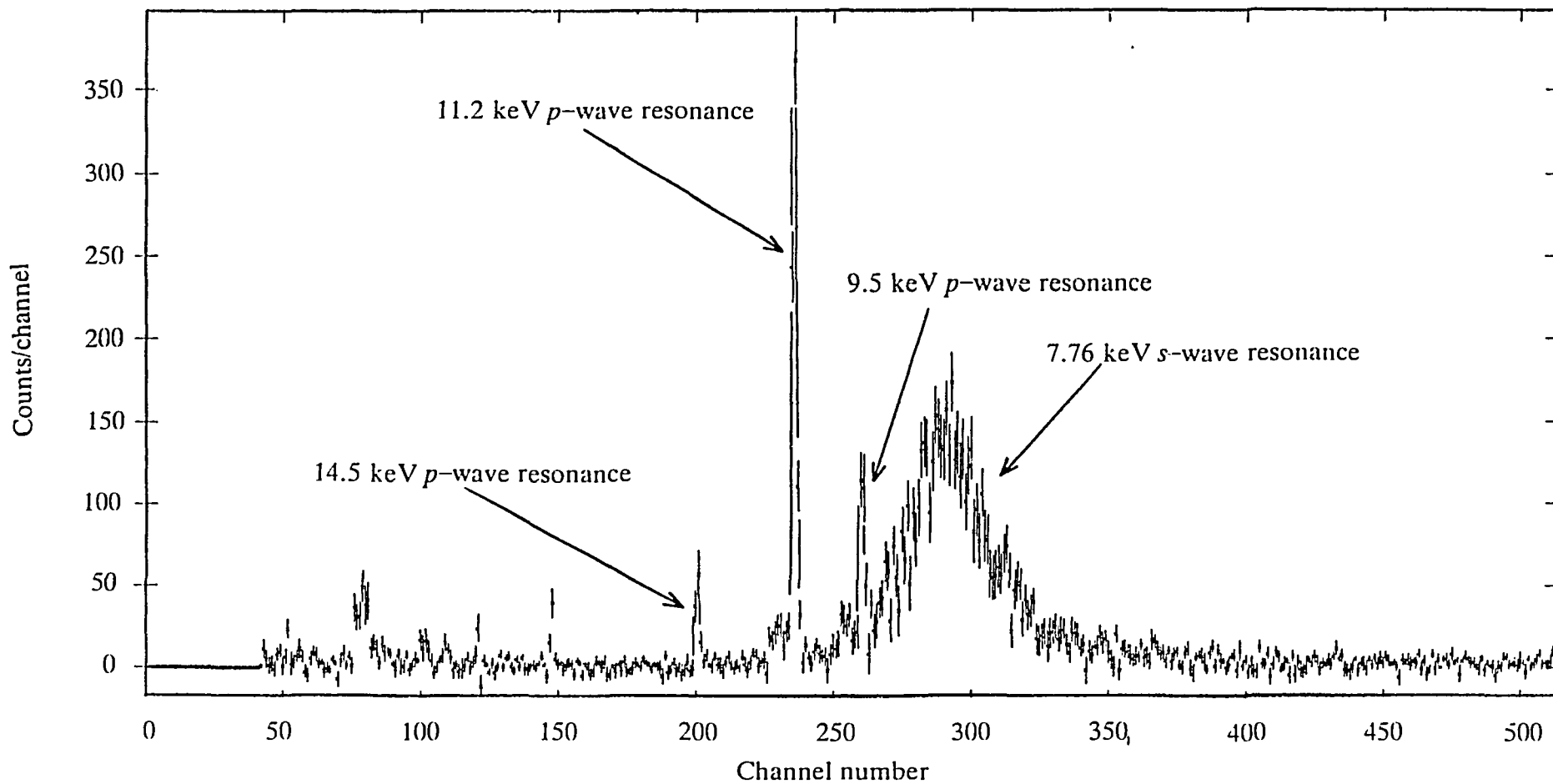


Fig. 4.6. The time-of-flight spectrum for the ground state transition following capture in ^{54}Fe . The most prominent resonances are marked. The off-resonance capture is seen to be small as would be expected, since potential capture is negligible at these neutron energies.

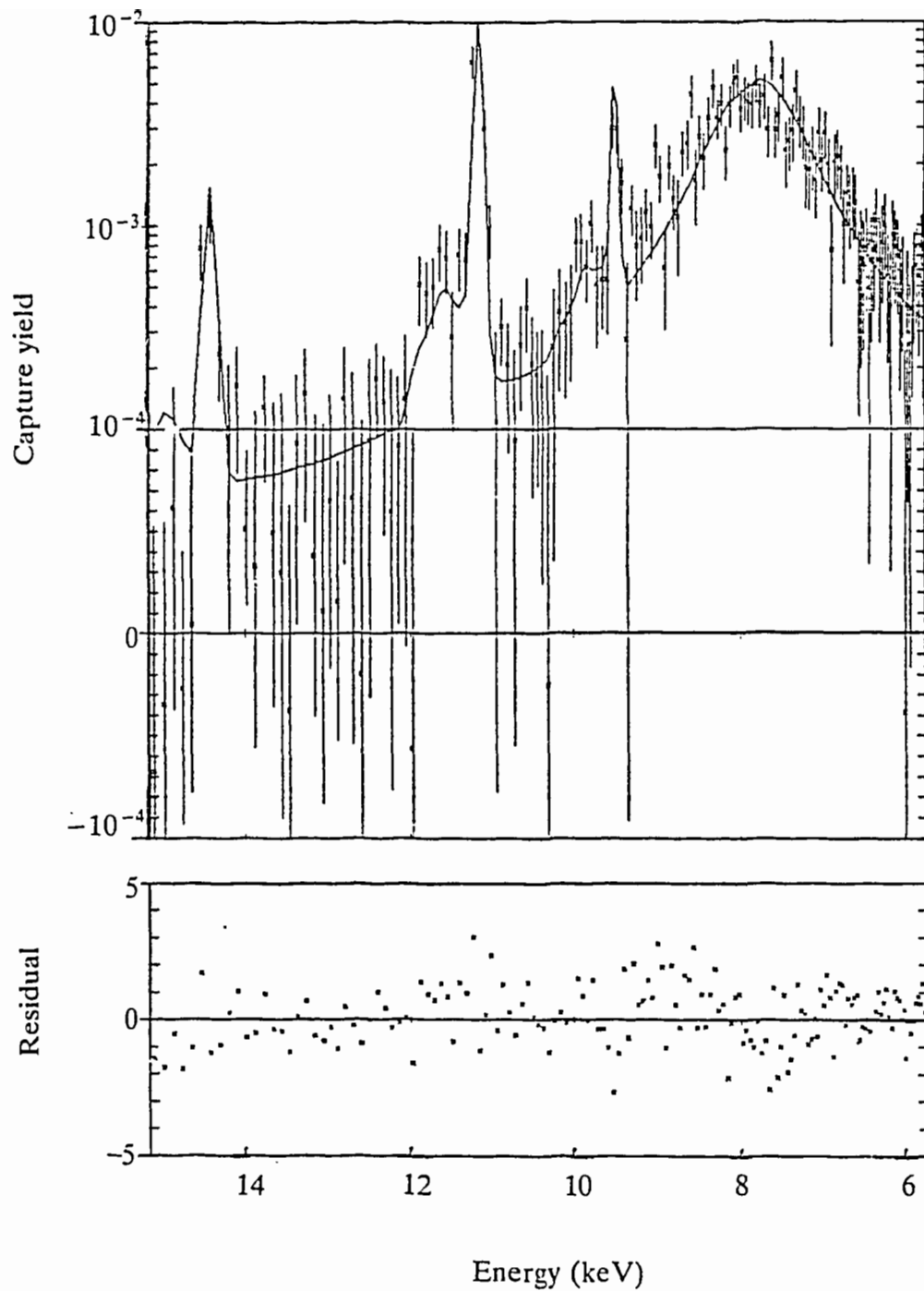


Fig. 4.7. The experimentally determined yield for the transition to the ground state following neutron capture in ^{54}Fe . The fit to the data was provided by the code REFIT and the corresponding residuals (deviations of the fit from the data divided by the error) are shown in the lower graph. The abscissa is a descending energy scale, not a time-of-flight scale, and corresponds to channels 195 to 350 of Figure 4.6.

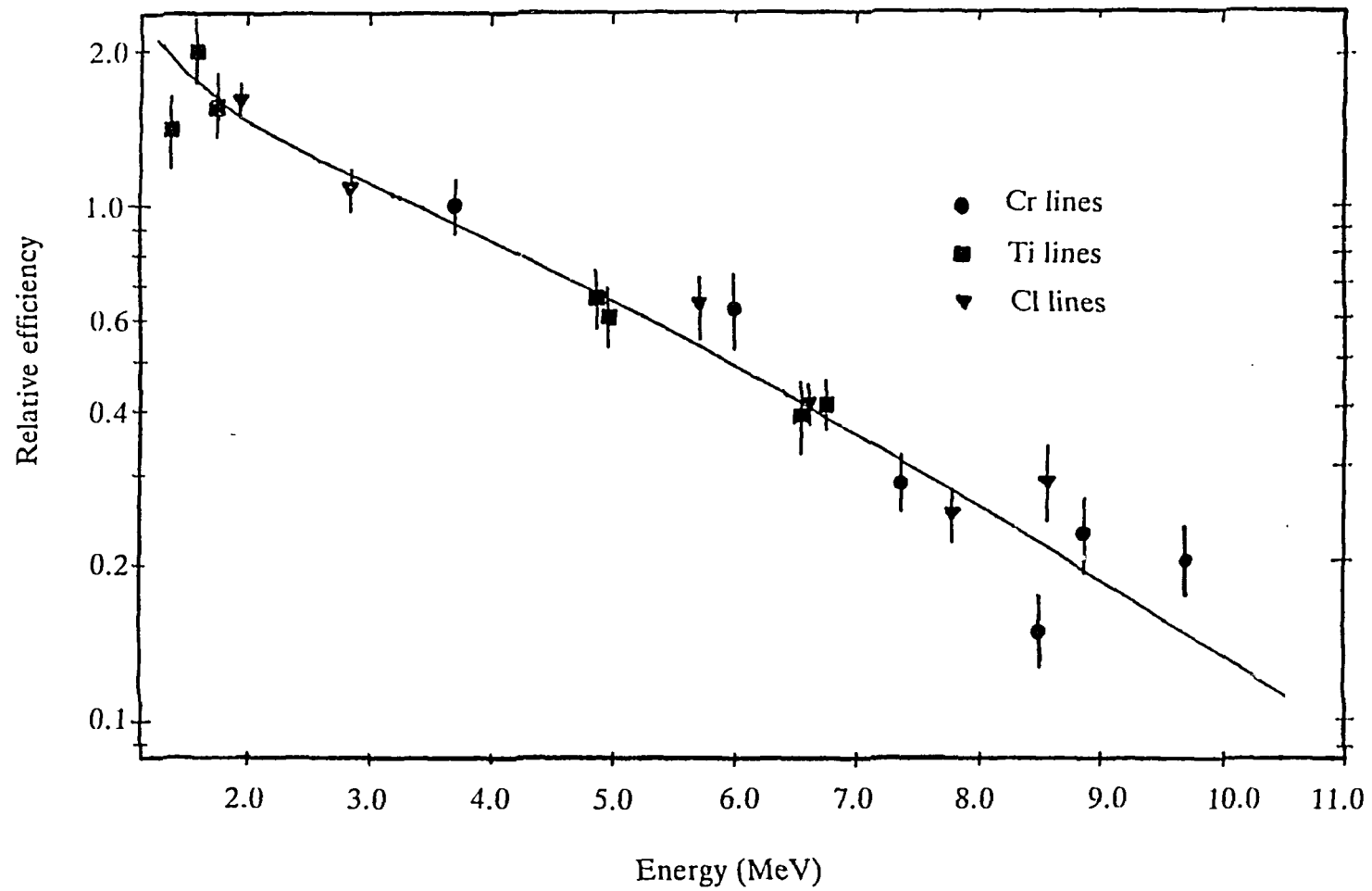


Fig. 5.1. The full energy efficiency curve for the PGT detector, provided by a five parameter fit to the data obtained from thermal neutron capture measurements.

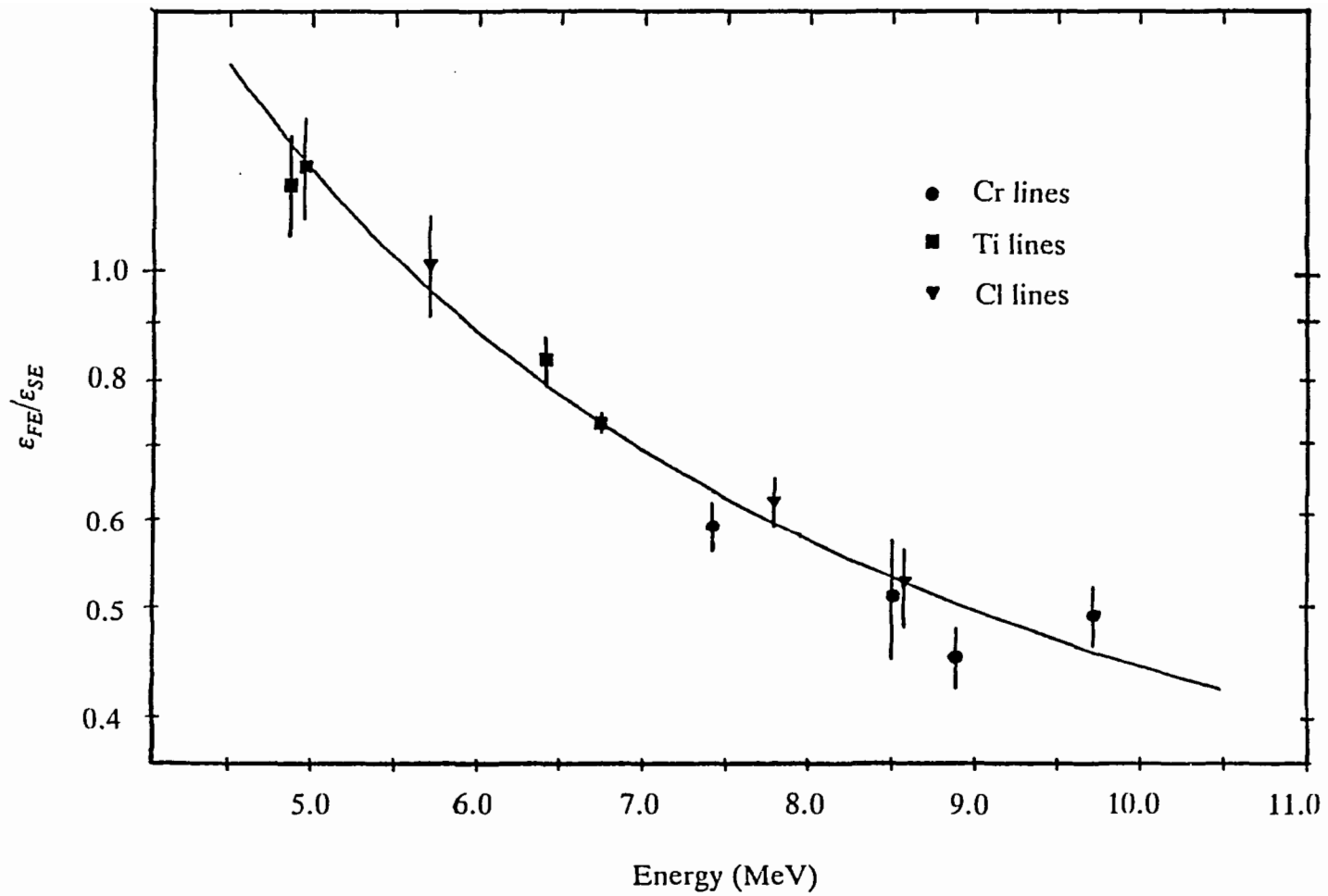


Fig. 5.2. The ratio of the full energy peak efficiency (ϵ_{FE}) to the single escape peak efficiency (ϵ_{SE}) for the EGG detector. The curve is a three parameter fit to the data.

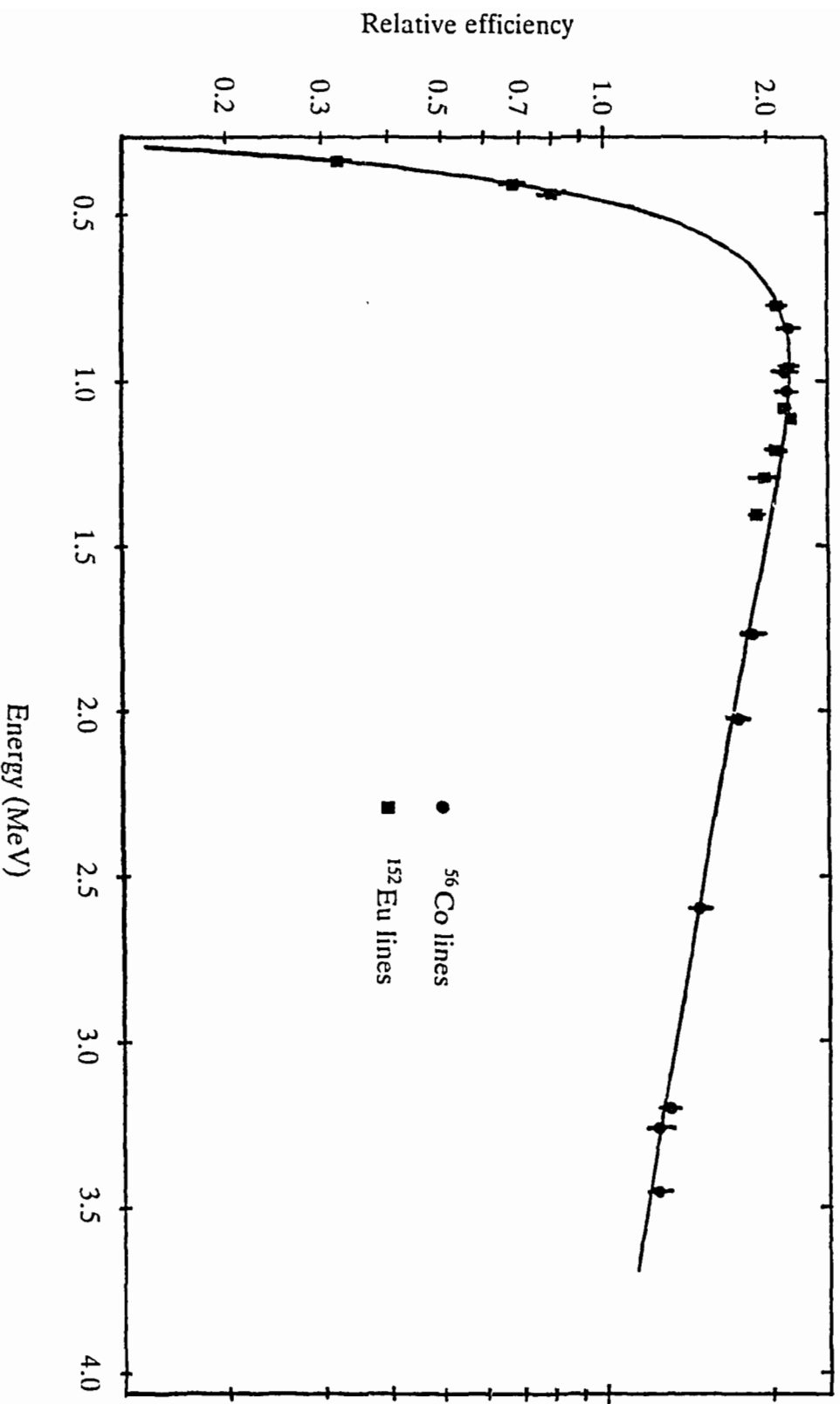


Fig. 5.3. The full energy peak efficiency for the EGG detector at low gamma-ray energies using data from ^{152}Eu and ^{56}Co sources. The curve is a six parameter fit to the data.

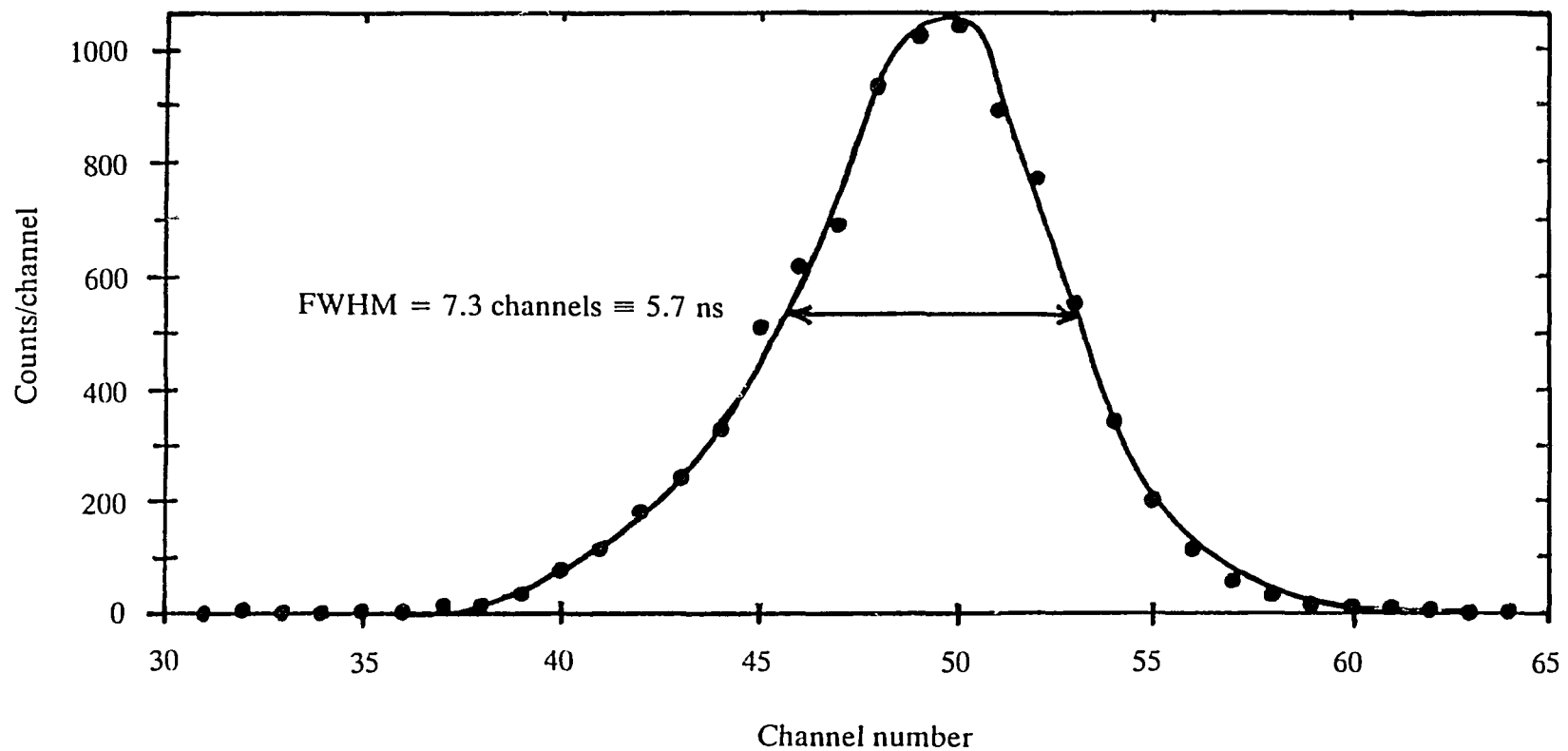


Fig. 5.4. A measurement of the PGT detector timing response function for gamma-rays in the energy range 810 – 920 keV. Start pulses were provided by a photomultiplier tube which detected gamma-rays in coincidence with the Ge detectors. The smooth curve through the points was drawn by eye.

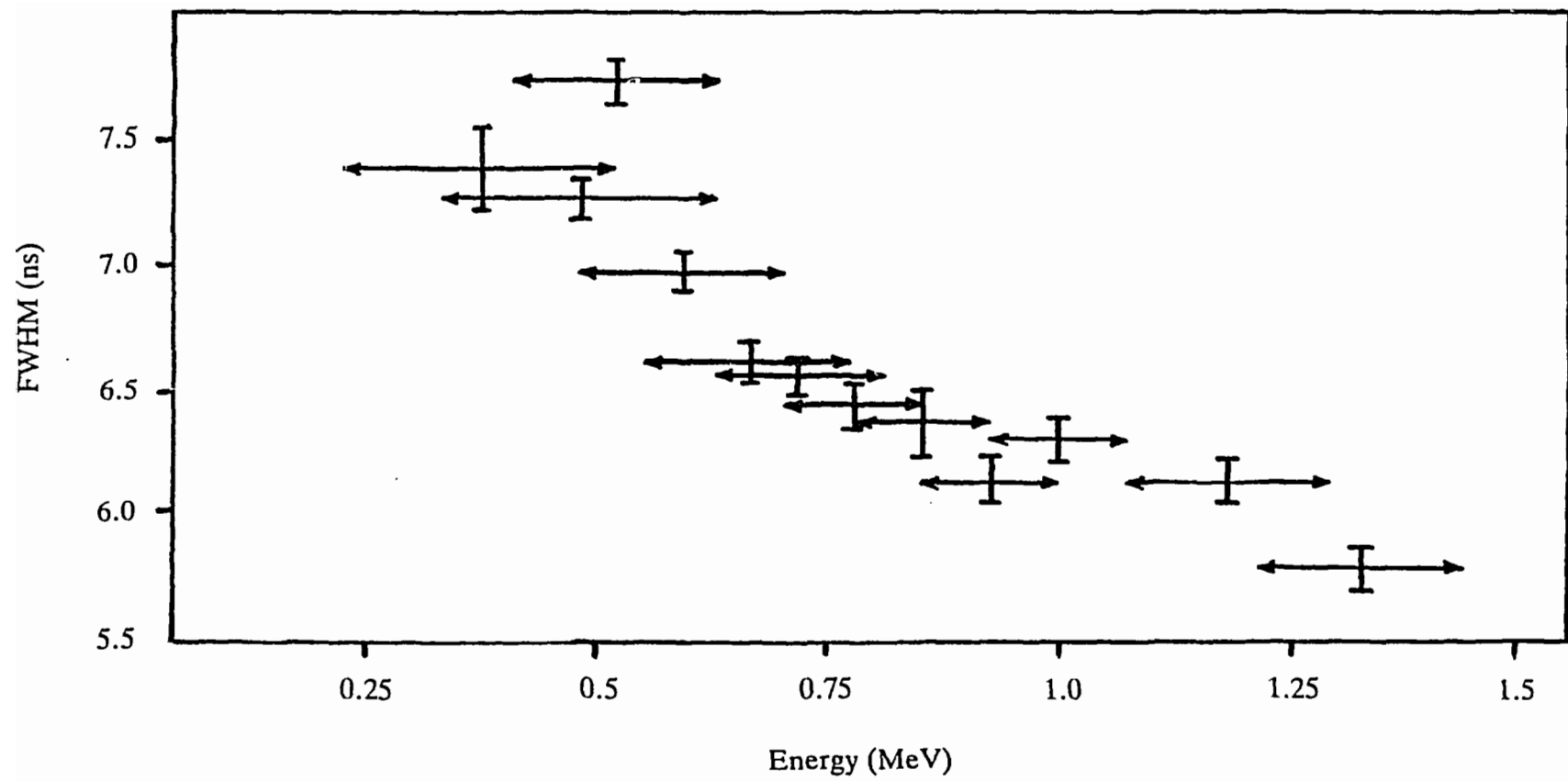


Fig. 5.5. The FWHM of the timing response of the EGG detector as a function of energy deposited in the detector. The horizontal bars on the data indicate the energy range over which the timing response was obtained.

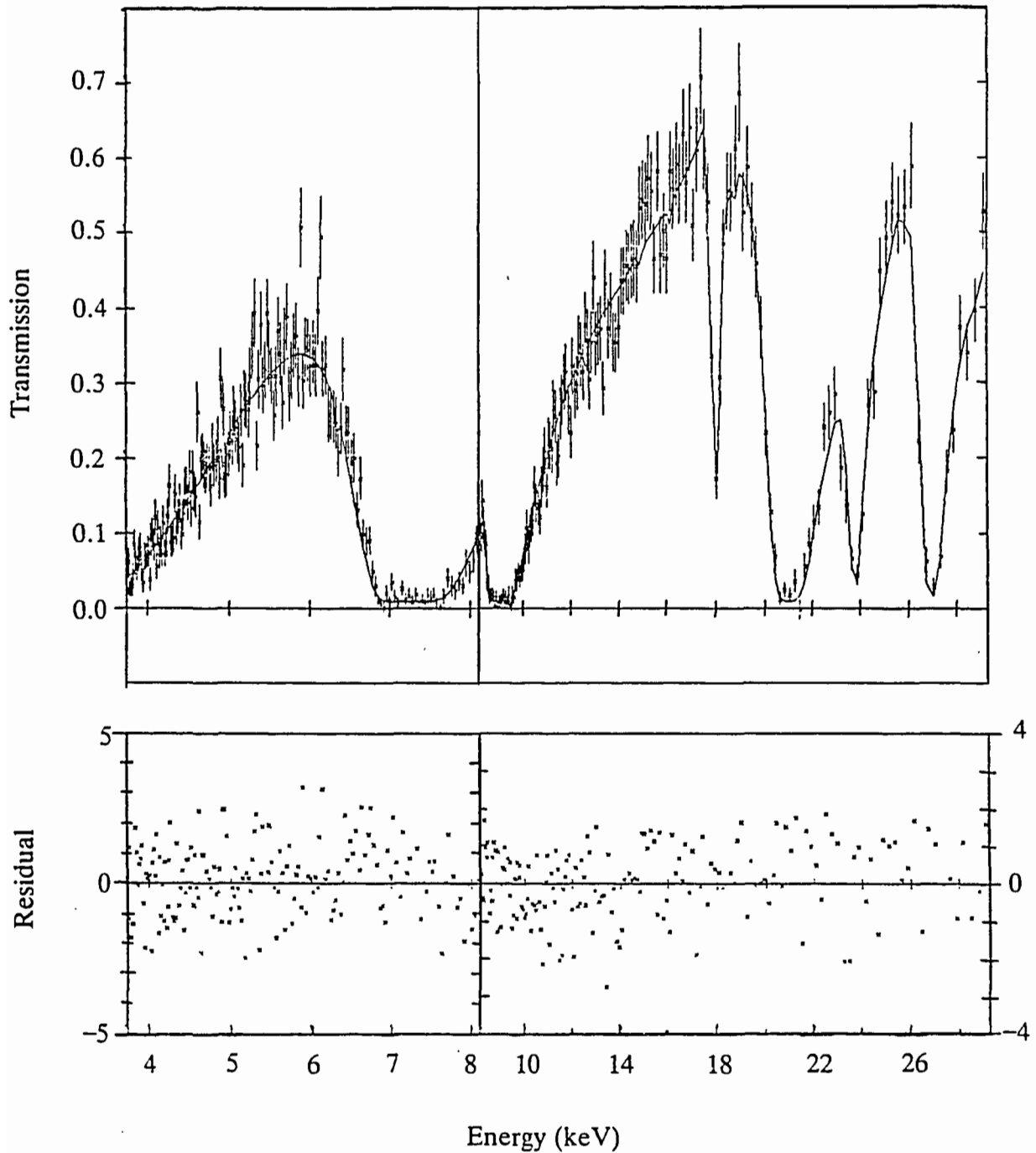


Fig. 5.6. The transmission observed through a $0.133 \text{ atoms b}^{-1}$ sample of Mn on the F2 flight path. The fit to the curve comes from calculations by the code REFIT, with a constant background of $(9 \pm 1) \times 10^{-3}$. Note the abscissa is a decreasing energy scale, and that at an energy of $\sim 8 \text{ keV}$ both the energy and the residual scales change.

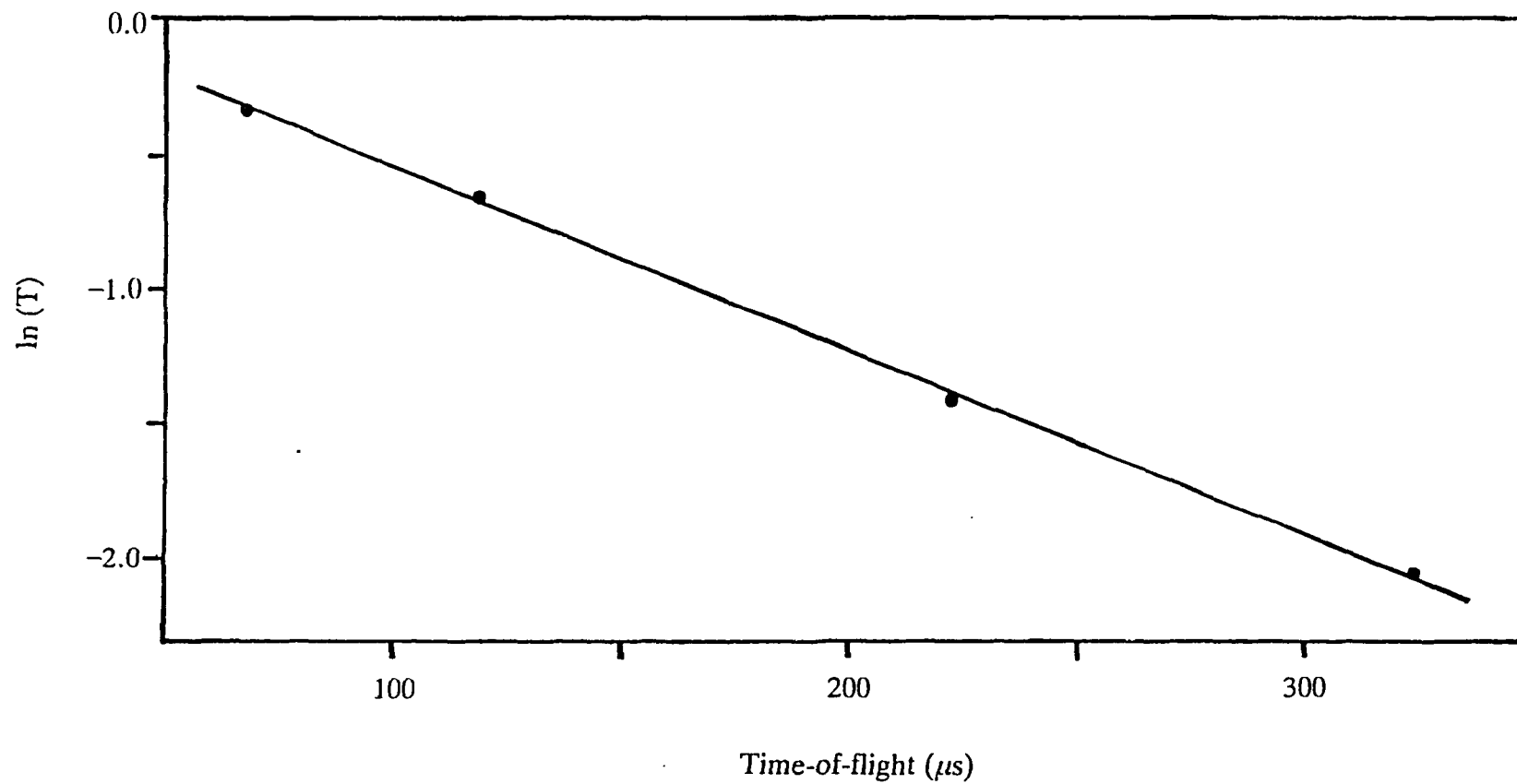


Fig. 5.7. Graph of the logarithm of the transmission through the ^{10}B sample, as a function of the time-of-flight. The straight line fit corresponds to a $1/v$ cross-section for the sample, and its slope determines that the value of n is 7.0 ± 0.1 atoms b^{-1} .

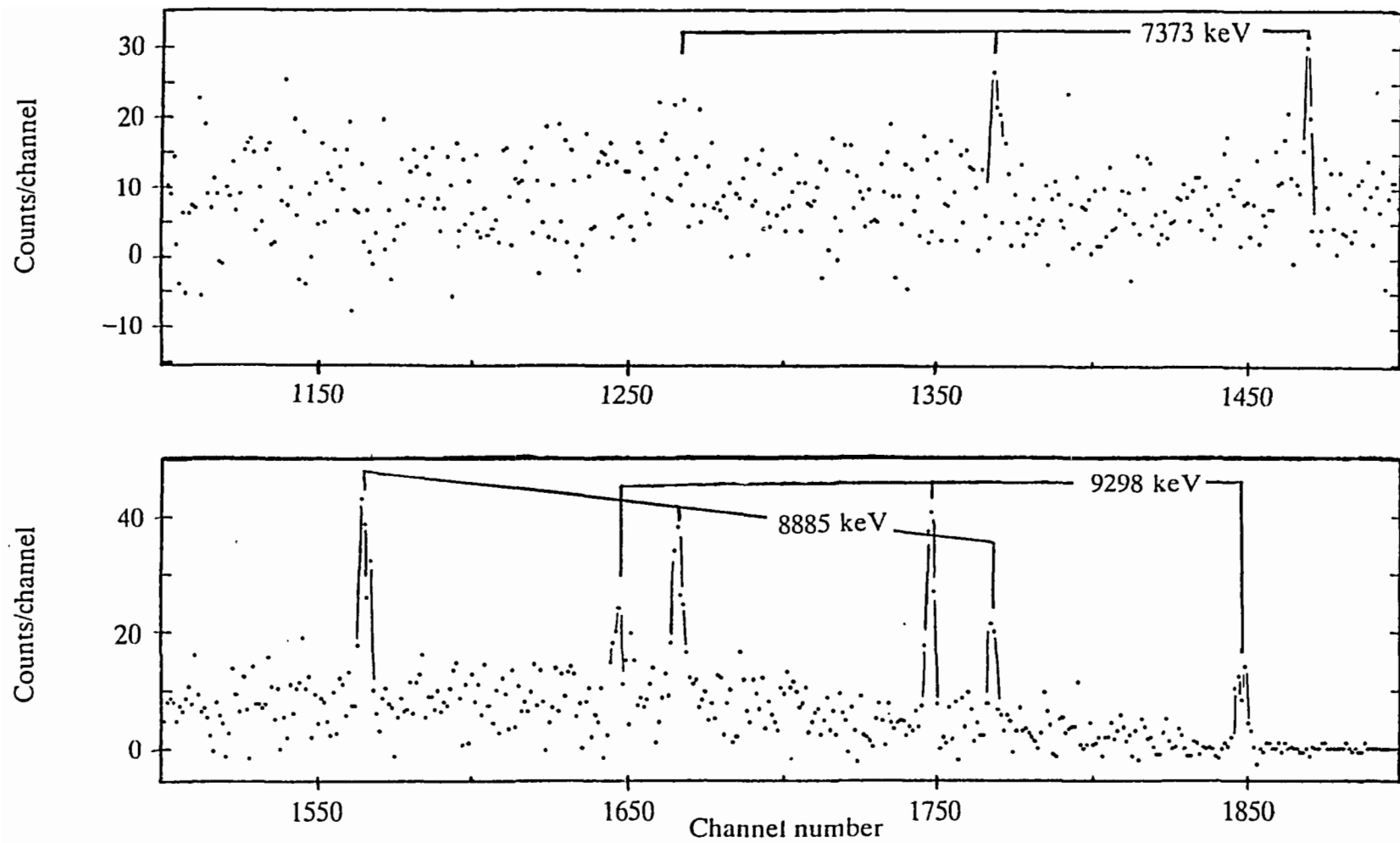


Fig. 6.1. The gamma-ray spectrum observed following capture in the 9.5 keV p -wave resonance of ^{54}Fe . The strong, high energy primary transitions are marked (with energies corresponding to thermal neutron capture).

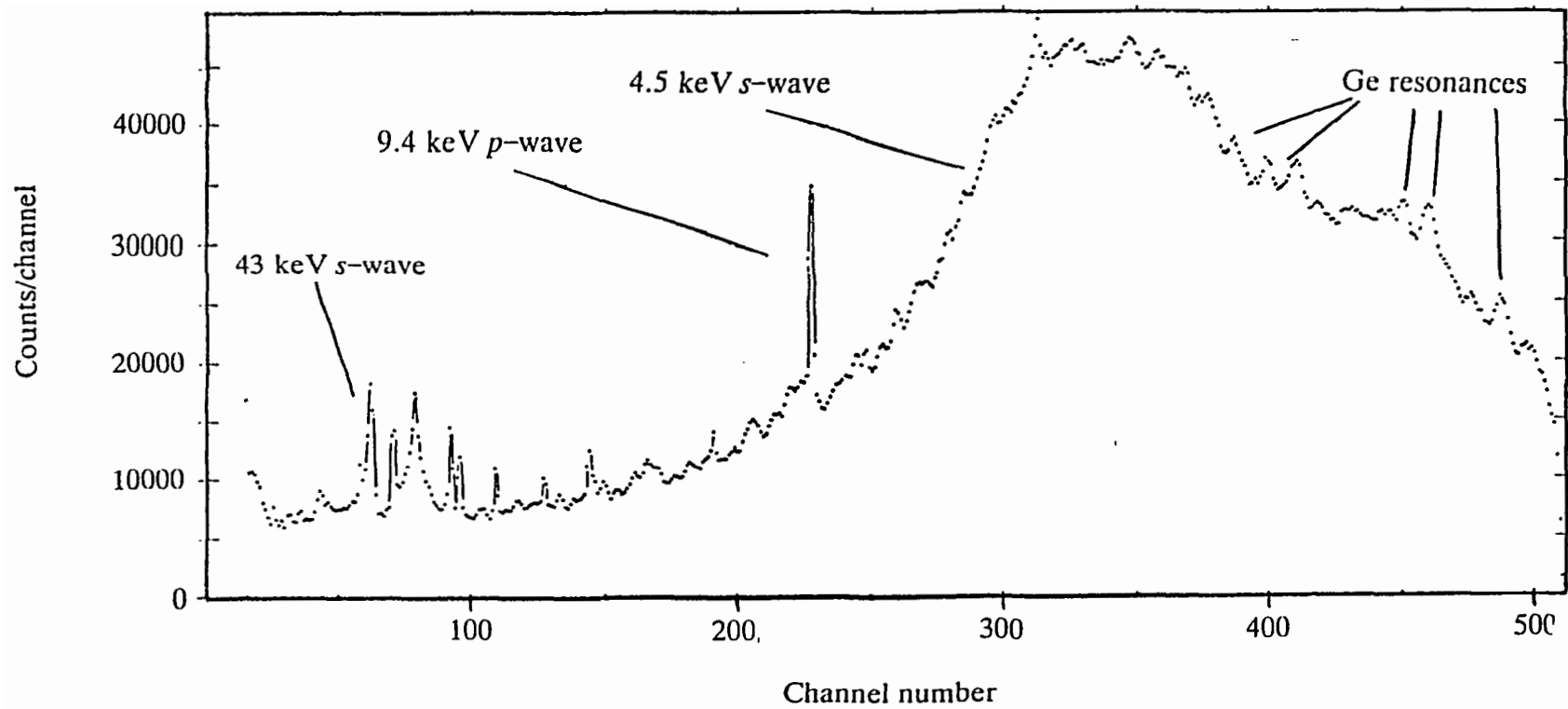


Fig. 6.2. The time-of-flight spectrum for all capture events in ^{62}Ni for which the gamma-ray energy was > 2.5 MeV. Individual resonances are marked, and examples of the effect of neutrons being captured in Ge resonances are indicated.

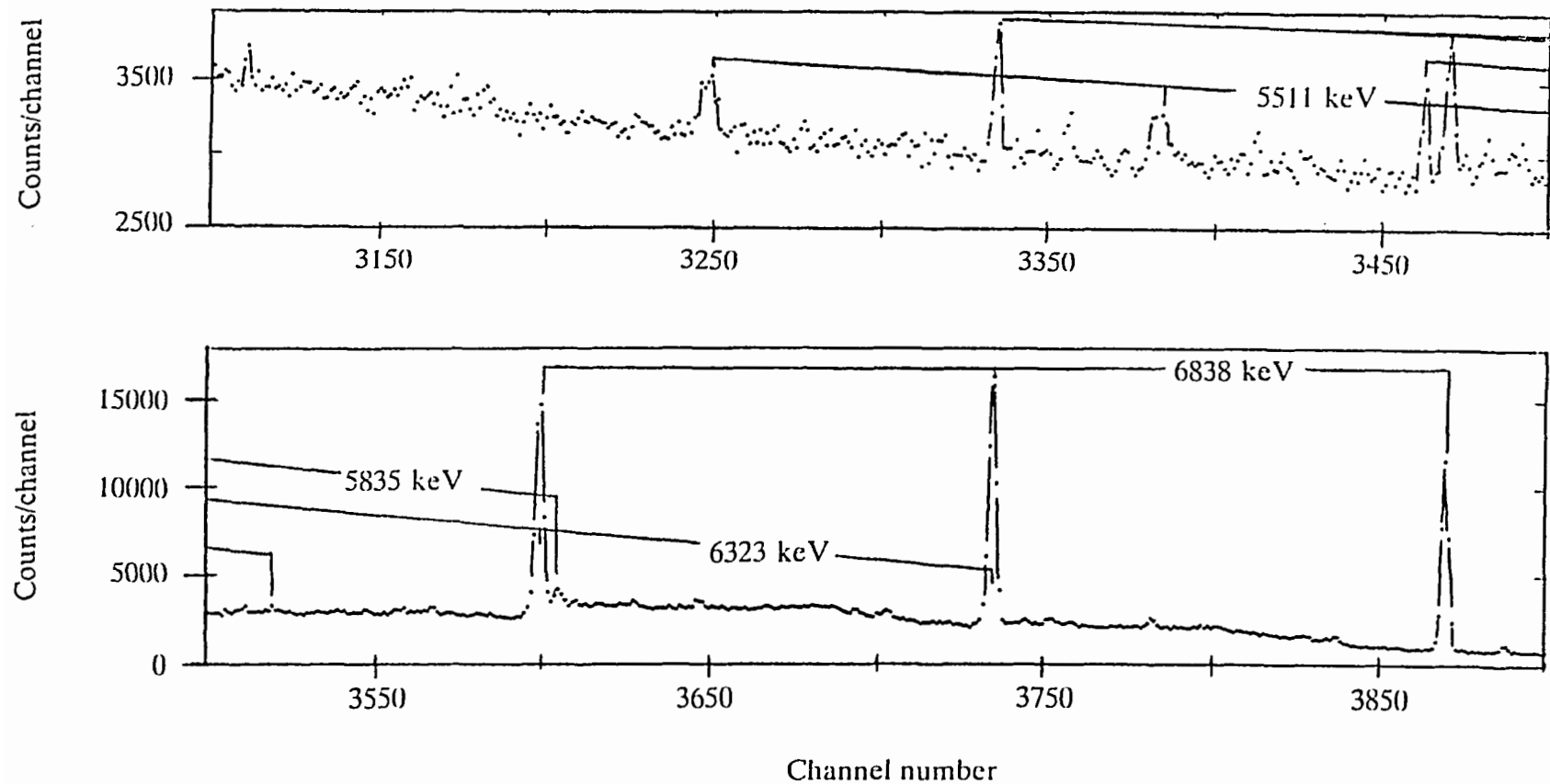


Fig. 6.3. The gamma-ray spectrum observed following capture in the 4.5 keV *s*-wave resonance of ^{62}Ni . Strong, high energy primary transitions are marked (with energies corresponding to thermal neutron capture), and the dominance of the 6.838 keV transition to the ground state of ^{63}Ni is evident.

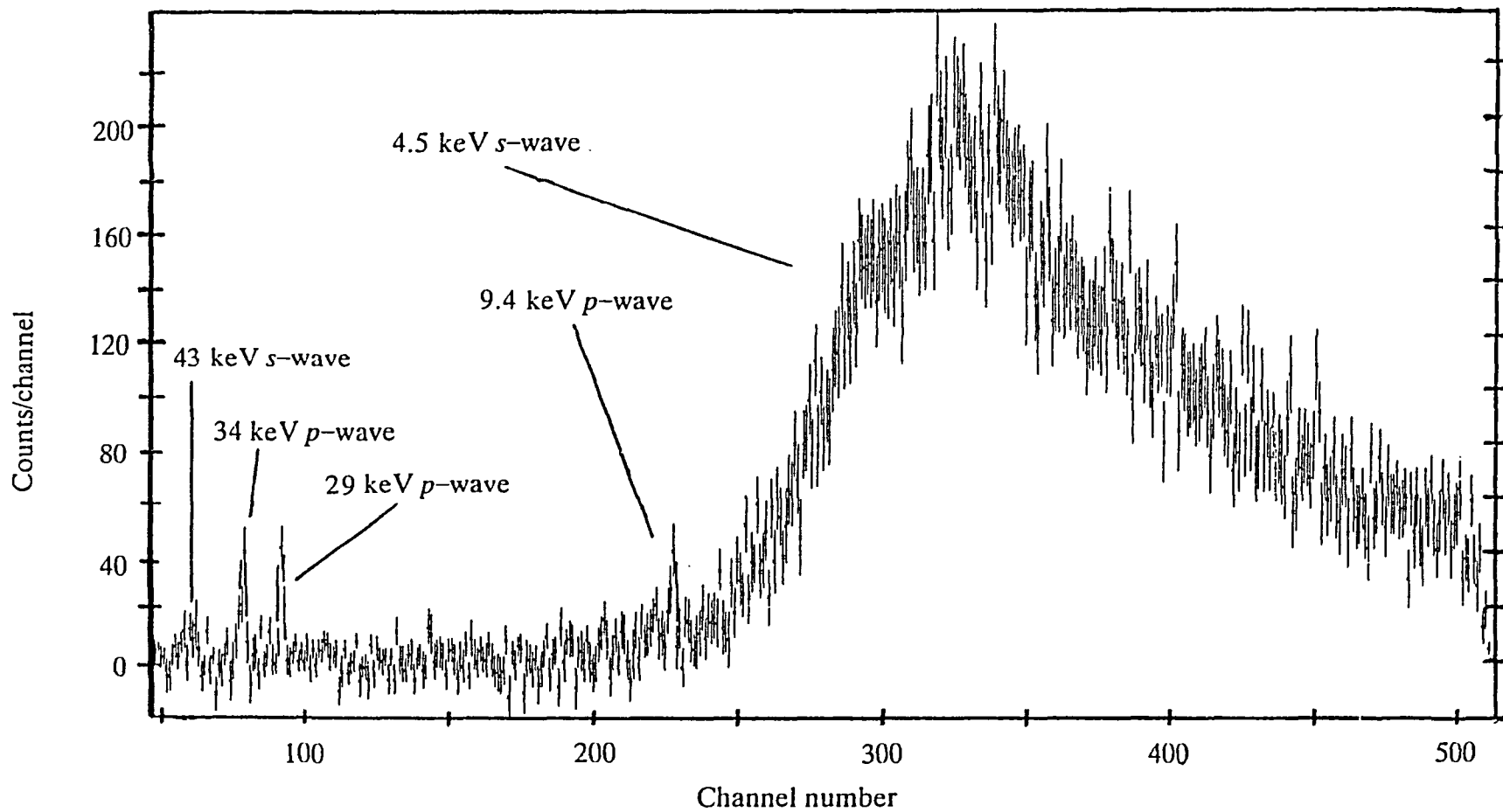


Fig. 6.4. The time-of-flight spectrum for the transition to the ground state following capture in ^{62}Ni . The most prominent resonances are marked, and the structure on the 4.5 keV resonance (see Figure 6.2) due to Ge resonances is no longer present.

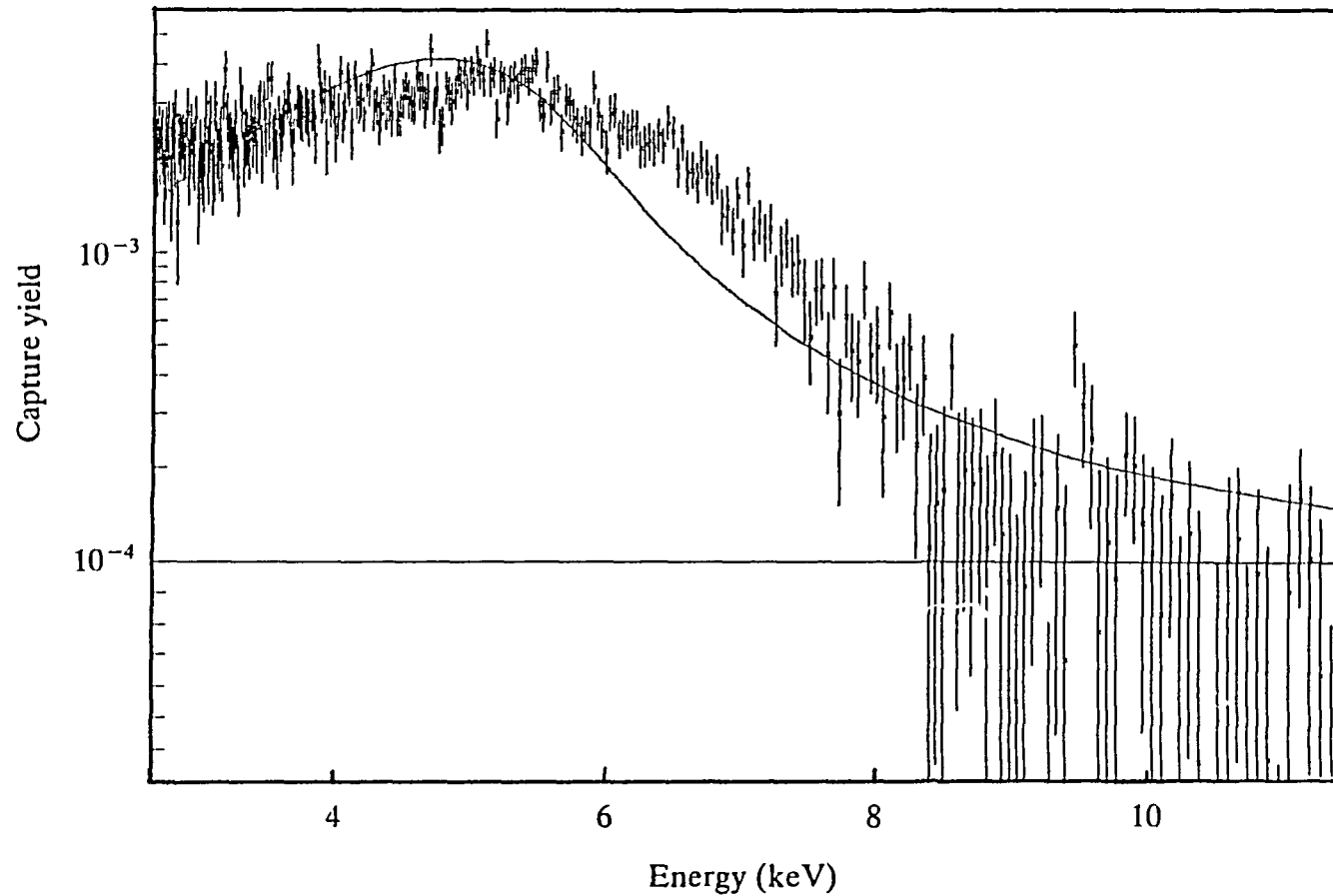


Fig. 6.5. Data obtained for the yield of the transition to the ground state following capture in ^{62}Ni . The curve is the best fit possible using reasonable values for the parameters of the 4.5 keV resonance. The inadequacy of this fit is believed to be due to the large amount of multiple scattering taking place. Note that the abscissa is an energy scale.

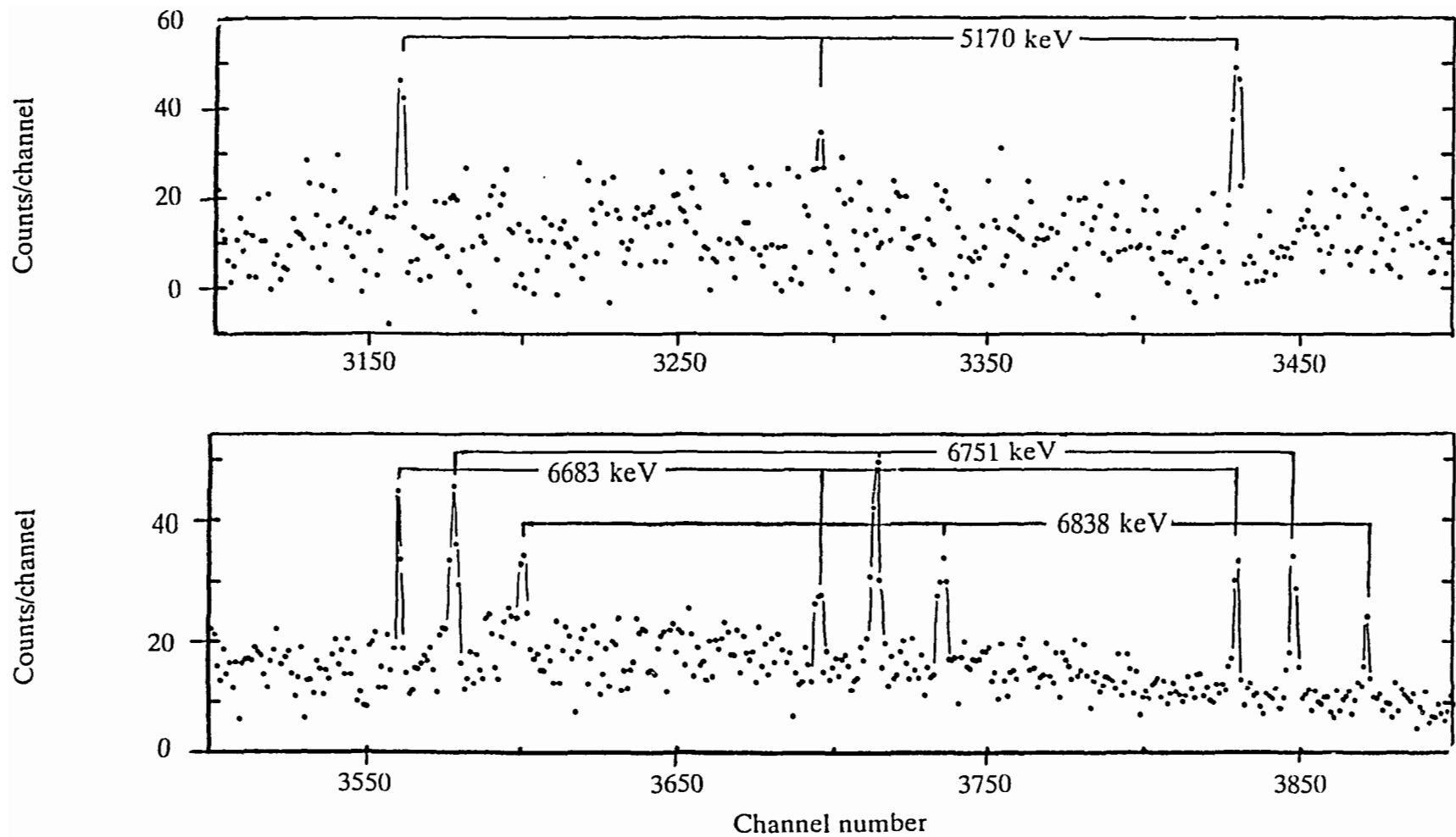


Fig. 6.6. The capture gamma-ray spectrum observed following capture in the 9.4 keV p -wave resonance of ^{62}Ni . Strong, high energy primary transitions are marked (with energies corresponding to thermal neutron capture). The strong gamma-ray line of energy 5170 keV, which is absent in the s -wave capture, is to a state at ~ 1.67 MeV in ^{63}Ni . A spin assignment of $5/2$ is suggested for the state.

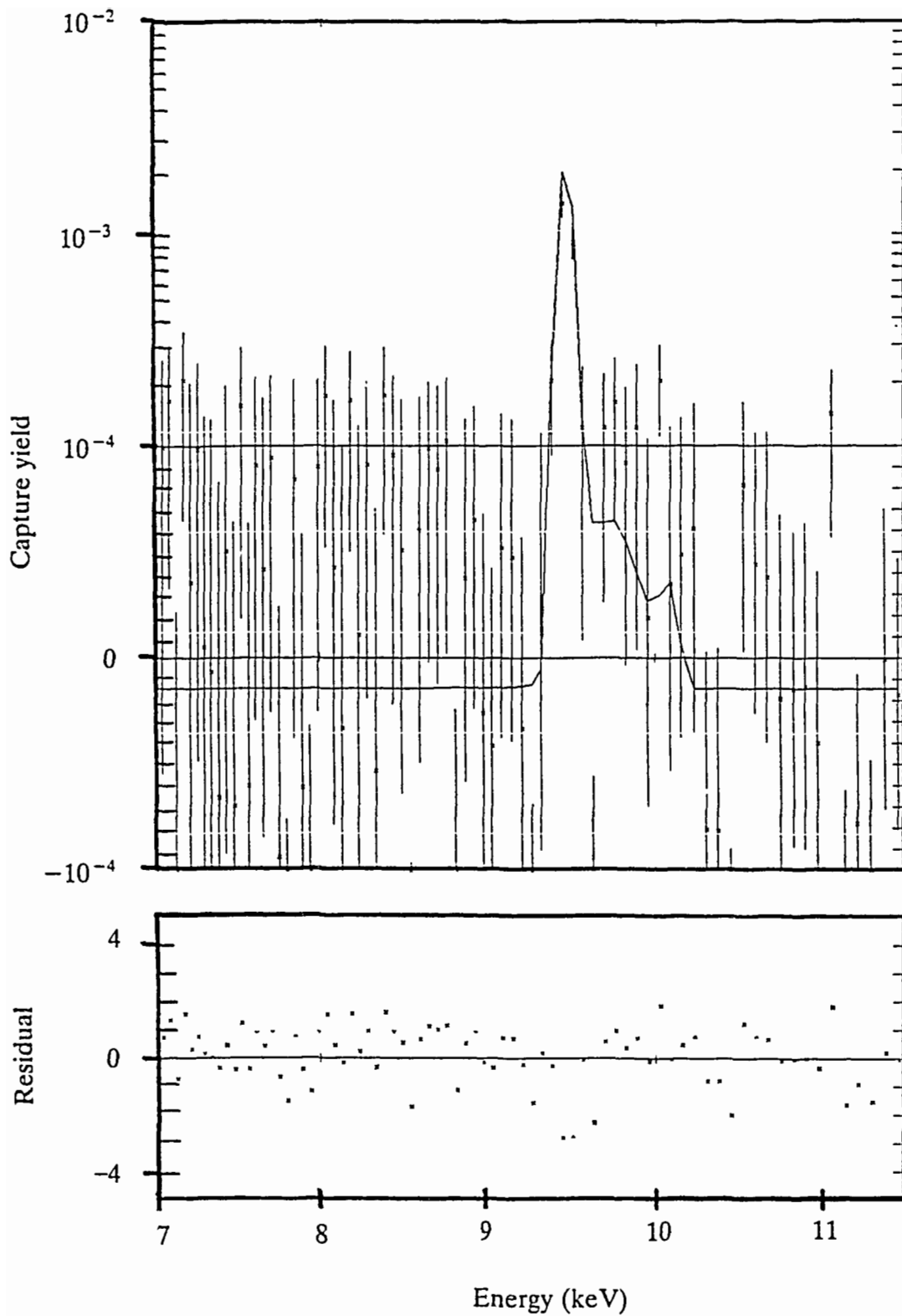


Fig. 6.7. The yield for the transition to the state at 1.67 MeV in ^{63}Ni following capture in ^{62}Ni . The curve is the best fit provided by the code REFIT and gives a value for the partial radiative width of this transition as 0.2 ± 0.05 eV. Note that the abscissa is an energy scale.

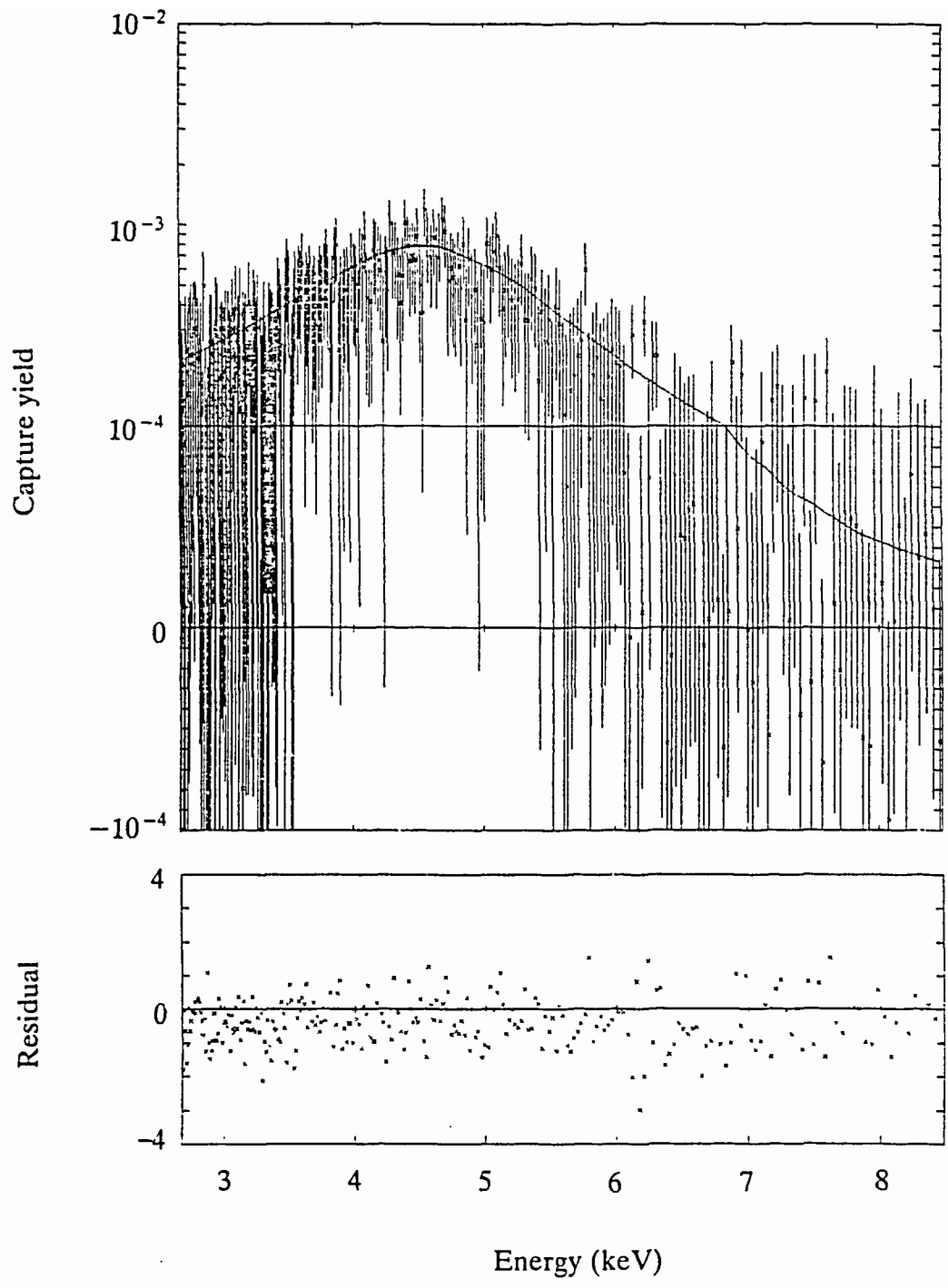


Fig. 6.8. The yield, obtained using a natural nickel sample, for the transition to the ground state of ^{63}Ni following capture in ^{62}Ni . The curve is the best fit provided by the code REFIT and gives a value for the partial radiative width of this transition as 3.0 ± 0.6 eV. Note that the abscissa is an energy scale.

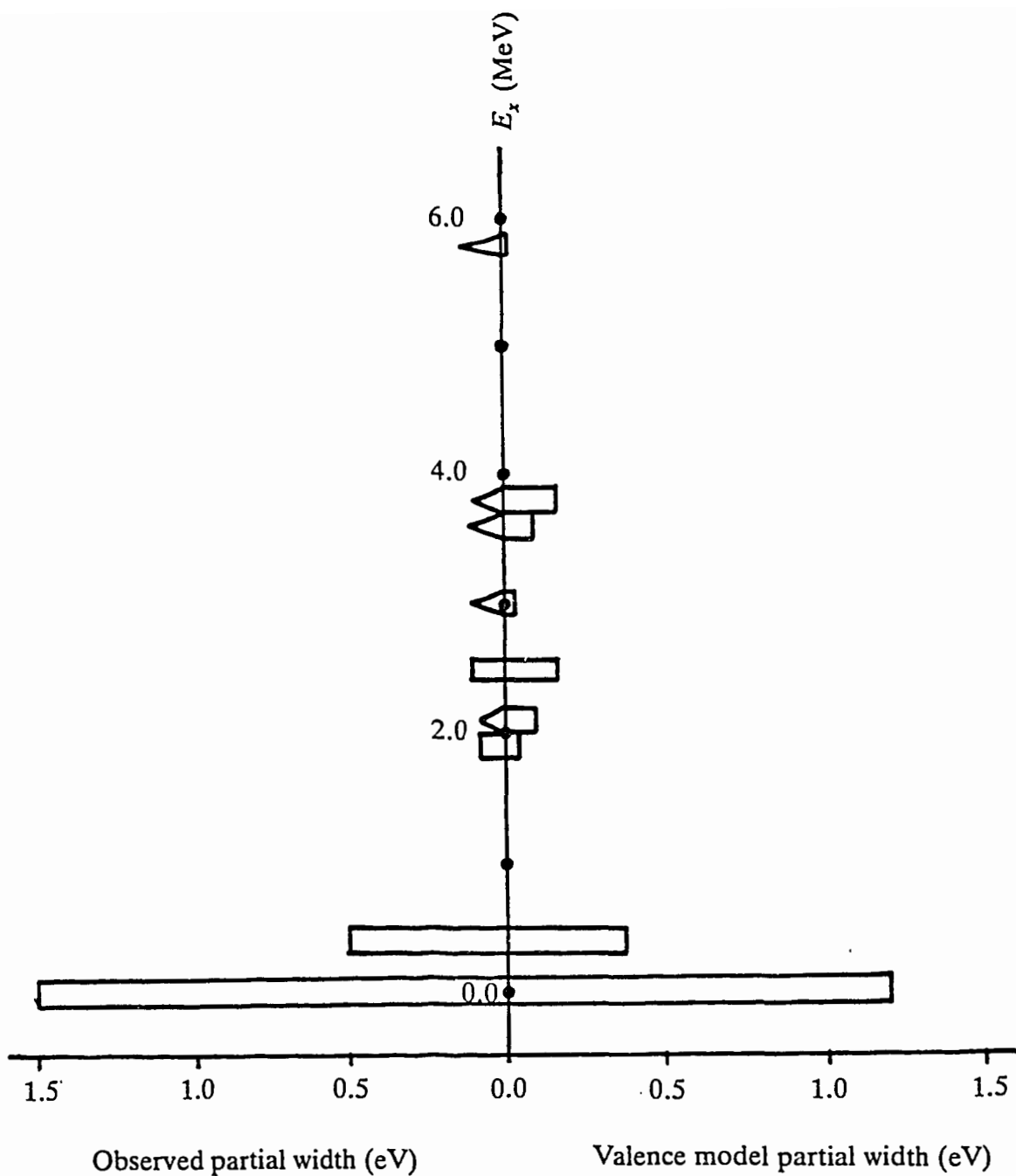


Fig. 7.1. The partial widths for transitions to states at energy E_x in ^{55}Fe , following capture in the 7.8 keV resonance of ^{54}Fe , compared with valence model predictions.

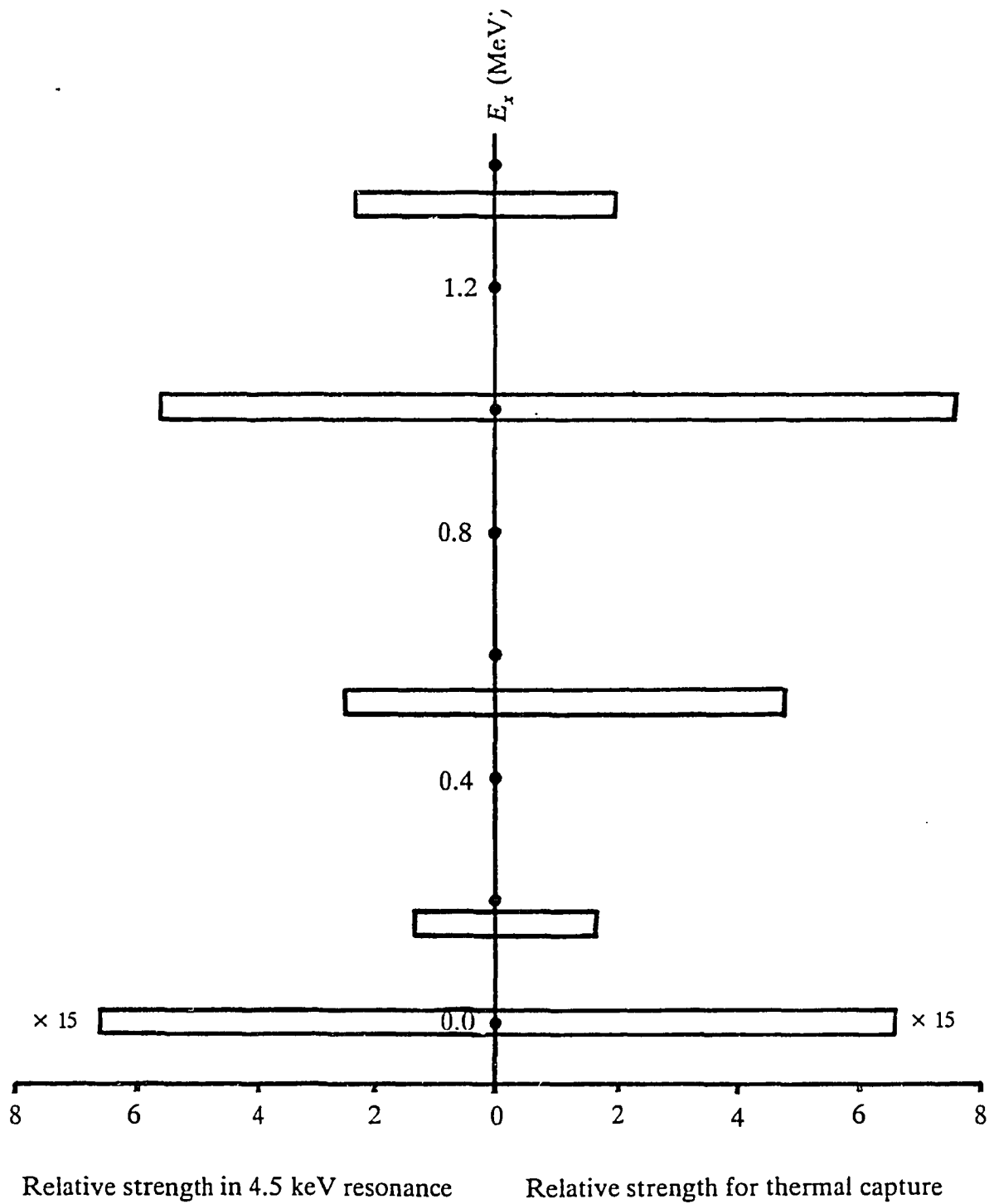


Fig. 7.2. Comparison of transitions strengths to states at energy E_x in ^{63}Ni , following thermal neutron capture, (Ish + 77), with capture in the 4.5 keV resonance of ^{62}Ni .